

THE ROLE OF DEEP-SEATED LANDSLIDES IN LANDSCAPE EVOLUTION:
QUANTITATIVE MODELING AND HIGH-RESOLUTION
TOPOGRAPHIC ANALYSIS

by

ADAM MICHAEL BOOTH

A DISSERTATION

Presented to the Department of Geological Sciences
and the Graduate School of the University of Oregon
in partial fulfillment of the requirements
for the degree of
Doctor of Philosophy

September 2012

DISSERTATION APPROVAL PAGE

Student: Adam Michael Booth

Title: The Role of Deep-Seated Landslides in Landscape Evolution: Quantitative Modeling and High-Resolution Topographic Analysis

This dissertation has been accepted and approved in partial fulfillment of the requirements for the Doctor of Philosophy degree in the Department of Geological Sciences by:

Josh Roering	Chairperson
Alan Rempel	Member
Gene Humphreys	Member
Mark Fonstad	Outside Member

and

Kimberly Andrews Espy	Vice President for Research & Innovation/Dean of the Graduate School
-----------------------	--

Original approval signatures are on file with the University of Oregon Graduate School.

Degree awarded September 2012

© 2012 Adam Michael Booth

DISSERTATION ABSTRACT

Adam Michael Booth

Doctor of Philosophy

Department of Geological Sciences

September 2012

Title: The Role of Deep-Seated Landslides in Landscape Evolution: Quantitative Modeling and High-Resolution Topographic Analysis

In many mountainous settings, landslides are the primary geomorphic agent that sets fundamental landscape characteristics, such as topographic relief and catchment-averaged erosion rate. The coupled system of landslides and other geomorphic processes responds to changes in climatic or tectonic forcing, but few studies have addressed these responses quantitatively, especially in terrain prone to deep-seated landslides (those thicker than the upper layer of soil). This study quantifies the topographic expressions and mechanics of deep-seated landslides using a combination of high-resolution topographic data and mathematical modeling. I first demonstrate that deep-seated landslides distinguish themselves from surrounding terrain by generating meter spatial scale surface roughness associated with gradients in strain rate of the deforming material. These methods are capable of mapping landslides with more than 80% accuracy in three study sites throughout the Pacific Northwest, United States. At longer, kilometer scale spatial wavelengths analysis of slope and drainage area data shows that landslides lengthen hillslopes and reduce ridge top elevations to leave their signature on the topography. I then develop and implement a mathematical landscape evolution model including a novel treatment of deep-seated landslide flux to simulate landslides at these

longer spatial scales. The model generates topographic profiles for two different bedrock types in agreement with those observed in a study area in the Eel River catchment, California, United States. The sediment fluxes required to produce these profiles are in agreement with independently estimated modern rates. Two-dimensional simulations constrain two essential geomorphic conditions at which landslides occur. First, there must be pre-existing pockets of deep weathering, which allow landslides to erode large volumes of material at rates that episodically exceed the long term average erosion rate. Second, the characteristic time scale for landslide processes must be shorter than the time scales associated with both soil creep and river incision. As the landslide time scale shortens, landslides systematically reduce hillslope relief and increase valley spacing to reduce the mean topographic gradient. This dissertation therefore improves the objectivity of analyzing landslide-prone terrain and provides a framework for rigorously interpreting landscape response to changing climatic and tectonic forcing.

This dissertation includes both previously published and co-authored material.

CURRICULUM VITAE

NAME OF AUTHOR: Adam Michael Booth

GRADUATE AND UNDERGRADUATE SCHOOLS ATTENDED:

University of Oregon, Eugene, Oregon
Grinnell College, Grinnell, Iowa

DEGREES AWARDED:

Doctor of Philosophy, Geology, 2012, University of Oregon
Bachelor of the Arts, Physics, 2004, Grinnell College

AREAS OF SPECIAL INTEREST:

Geomorphology and Landscape Evolution

PROFESSIONAL EXPERIENCE:

Research / Teaching Assistant, Department of Geological Sciences, University of Oregon, Eugene, 2007-2012

GRANTS, AWARDS, AND HONORS:

Graduate Teaching Fellowship, Department of Geological Sciences, University of Oregon, 2007-08 and 2011-12

Graduate Research Fellowship, National Science Foundation, 2008-2011

Nordic Research Opportunity Fellowship, National Science Foundation and The Research Council of Norway, 2010

Outstanding Student Paper Award, American Geophysical Union, 2009

Phi Beta Kappa, Grinnell College, 2004

Honors in Physics, Grinnell College, 2004

PUBLICATIONS:

- Booth, A., Roering, J. (2011). A 1-D mechanistic model for the evolution of earthflow-prone hillslopes. *Journal of Geophysical Research* 116, F04021, doi:10.1029/2011JF002024.
- Roering, J.J., Marshall, J., Booth, A., Mort, M., Jin, Q. (2010). Evidence for biotic controls on topography and soil production. *Earth and Planetary Science Letters* 298, 183-190.
- Booth, A., Roering, J., Perron, J.T. (2009). Automated landslide mapping using spectral analysis and high-resolution topographic data: Puget Sound lowlands, Washington, and Portland Hills, Oregon. *Geomorphology* 109, 132-147. doi:10.1016/j.geomorph.2009.02.027.
- Borovsky, B., Booth, A., Manlove, E. (2007). Observation of microslip dynamics at high-speed microcontacts. *Applied Physics Letters* 91, 114101. doi:10.1063/1.2784172.

ACKNOWLEDGMENTS

I thank my committee for their genuine interest in this work and for their wide ranging ideas which pushed me to new and exciting directions. I especially thank my advisor, Dr. Josh Roering, who both motivated me and allowed me the academic freedom to pursue my interests and develop as a scientist, and Dr. Alan Rempel, who shared both the intricate details and his broader philosophy of mathematical modeling in the earth sciences. Many discussions with my present and past lab mates Alex Handwerger, Ben Mackey, Jill Marshall, Corina Cerovski-Darriau, and Kristen Sweeny were also stimulating in generating this dissertation. My parents and siblings were extremely instrumental in making me believe that I could pursue a doctoral degree. My wife, Leslie Barnard Booth, supported me through the entire process, and I have grown immeasurably as a person, and perhaps as a scientist, because of her. Finally, our daughter, Iris Lynn Booth, has given me an entirely new and unanticipated outlook on the world. The work was supported by a National Science Foundation (NSF) Graduate Research Fellowship, NSF awards OCE-084111 and EAR-0447190 to Josh Roering, and NASA award NNX08AF95G also to Josh Roering.

TABLE OF CONTENTS

Chapter	Page
I. INTRODUCTION.....	1
II. AUTOMATED LANDSLIDE MAPPING USING SPECTRAL ANALYSIS AND HIGH-RESOLUTION TOPOGRAPHIC DATA: PUGET SOUND LOWLANDS, WASHINGTON, AND PORTLAND HILLS, OREGON	4
1. Introduction.....	4
2. Study Areas.....	6
2.1. Tualatin Mountains, Oregon	7
2.2. Puget Sound Lowlands, Washington	11
3. Methods.....	13
3.1. 2D DFT.....	14
3.2. 2D CWT	15
3.3. Fourier and Wavelet Spectra	17
3.4. Mapping Spectral Power	21
3.4.1. Windowed 2D DFT	21
3.4.2. 2D CWT.....	22
3.5. Optimizing Algorithm Outputs.....	23
4. Results.....	24
4.1. Landslide Maps.....	24
4.2. Dominant Wavelength Map.....	31

Chapter	Page
5. Discussion.....	34
6. Conclusions.....	36
III. A 1-D MECHANISTIC MODEL FOR THE EVOLUION OF EARTHFLOW- PRONE HILLSLOPES.....	39
1. Introduction.....	39
2. Study Areas: Eel River and Gabilan Mesa, California	44
3. Model Formulation	52
3.1. Soil Creep.....	53
3.2. Gully Incision.....	55
3.3. Earthflow Flux and Weathering.....	56
3.4. Governing Equation and Nondimensionalization	60
3.5. Steady State Solutions.....	64
4. Results	65
4.1. Matching Observed Profiles	66
4.2. Spatial Erosion Patterns	72
4.3. Long-Term Process Rates	76
4.4. Model-Predicted Steady-State Hillslope Relief.....	79
5. Discussion	82
6. Conclusions.....	88

Chapter	Page
IV. TOPOGRAPHIC SIGNATURES OF SLOW-MOVING, DEEP-SEATED	
LANDSLIDES AND A GENERAL LANDSCAPE EVOLUTION MODEL.....	90
1. Introduction.....	90
2. Topographic Signatures of Slow-Moving, Deep-Seated Landslides.....	94
2.1. Study Areas.....	95
2.2. Topographic Signatures.....	98
3. Landscape Evolution Model.....	102
3.1. Modeling Goals.....	102
3.2. Geomorphic Process Model.....	103
3.3. Numerical Model.....	110
4. Results.....	111
4.1. Estimating the Landslide Parameter, a.....	112
4.2. The Non-Dimensional Landslide Number.....	113
4.3. Controls on Stochastic Landslide Behavior.....	118
4.4. Landslide Regime Phase Space.....	119
4.5. Topographic Signatures.....	123
4.6. Uplift Rate and Catchment Relief.....	126
5. Discussion and Conclusions.....	128
APPENDIX: NUMERICAL SOLUTION OF EQUATIONS (12) AND (13).....	133
REFERENCES CITED.....	136

LIST OF FIGURES

Figure	Page
 Chapter II	
1. LiDAR-derived hillshade map of the Dixie Mountain quadrangle, Oregon (DMQ) study area	8
2. LiDAR-derived hillshade map of the marine Thurston County, Washington (MTC) study area.....	9
3. LiDAR-derived hillshade map of the Seattle, Washington (SEA) study area.....	9
4. (A) Two-dimensional Mexican hat wavelet ($s=1$), and (B) its Fourier transform	16
5. LiDAR-derived hillshade map of the NWD study area.....	18
6. LiDAR-derived hillshade map of the CBP study area.....	19
7. Power spectra indicating the frequency bands characteristic of deep-seated landslides.....	19
8. Spectral power sums from the (A) 2D DFT and (B) 2D CWT and their corresponding optimally classified landslide maps (C and D) for the NWD study area	25
9. Spectral power sums from the (A) 2D DFT and (B) 2D CWT and their corresponding optimally classified landslide maps (C and D) for the CBP study area.....	25
10. Spectral power sums from the (A) 2D DFT and (C) 2D CWT and their corresponding optimally classified landslide maps (B and D) for the SEA study area.....	27
11. Error index curves used to select optimal cutoff spectral power sums.....	29
12. Dominant wavelength map for deep-seated landslides in study area CBP.....	33
 Chapter III	
1. LiDAR-derived hillshade map of the Eel River study area	45

Figure	Page
2. Perspective view from Figure 1c, illustrating the typical geomorphology of earthflow-prone hillslopes	47
3. (left) Slope-area plots for the Eel River and Gabilan Mesa study sites, and (right) histogram of drainage area for the Eel River study site.....	50
4. (a) Normalized elevation and (b) topographic gradient versus distance from the drainage divide for representative steady state model-generated profiles	54
5. LiDAR-derived hillshade maps of sites used to compare steady state model solutions to representative topographic profiles	67
6. Representative and best fit hillslope profiles	68
7. Misfit versus the landscape evolution model's free parameters at each of the study sites.....	71
8. Contributions of each modeled geomorphic process to $\partial z^*/\partial t^*$ at each point along the best fit profiles.....	74
9. Model-predicted hillslope relief (normalized by hillslope length) as a function of uplift rate.....	80
 Chapter IV	
1. Example of a catchment dominated by slow-moving, deep-seated landslides near the Waipaoa River, North Island, New Zealand	92
2. LiDAR-derived hillshade map of the Waipaoa study area	97
3. LiDAR-derived hillshade map of the Eel River study area	99
4. LiDAR-derived slope-area plots for the Waipaoa and Eel River study areas	100
5. LiDAR-derived hillshade map (Figure 3, dashed white box), illustrating the spatial arrangement of the geomorphic process regimes	102
6. Dependence of (a) mean topographic gradient and (b) mean valley spacing of modeled catchments on V^* for thick steady state weathered zones	116

Figure	Page
7. Dependence of (a) mean topographic gradient and (b) mean valley spacing of modeled catchments on V^* for thin steady state weathered zones	120
8. Phase space illustrating the 3 model landscape regimes (no landsliding, steady landsliding, and stochastic landsliding) for combinations of V^* and ζ	121
9. Dependence of the standard deviation of weathered zone depths on V^* along transect A-A' in Figure 8	124
10. Relief v. uplift rate curves for modeled landscapes in each of the three landsliding regimes	127

LIST OF TABLES

Table	Page
Chapter II	
1. Comparing Algorithm-Generated and Independently Compiled Deep-Seated Landslide Maps in Each Study Area.....	28
Chapter III	
1. Parameter Values That Generate the Best Fit Between Modeled and Observed Hillslope Profiles	69
2. Long-Term Average Sediment Fluxes.....	78
Chapter IV	
1. Estimation of the Flow Law Constant, a	112
2. Parameters Used to Generate Figure 6.....	116
3. Parameters Used to Generate Figure 7.....	118

CHAPTER I

INTRODUCTION

Since the early 20th century, two of the most fundamental questions in geomorphology, inspired in no small part by the pioneering work of G. K. Gilbert, have been simply, "what does the surface of the earth look like?", and the natural follow up, "why?" The tools used to answer these questions have changed – for example from sketches, to topographic maps, to meter scale resolution digital elevation models – but the basic job of the geomorphologist remains essentially the same. This dissertation aims to answer these questions in a quantitative way, as they relate to a particular geomorphic process: deep-seated landslides.

Landslides are important from an applied science perspective because of potential hazards, and also from a basic science perspective because they often transport large volumes of sediment, thereby strongly influencing topographic form, sediment budgets, and long-term erosion rates. However, rates and sizes of landslides often vary by many orders of magnitude within a mountain range, making it difficult to relate landslide processes at the timescales over which they can be observed to their underlying drivers, such as tectonic uplift, land use, or climate. More specifically, even with modern field instrumentation and remote sensing data, the outwardly simple act of mapping landslides is subjective and time consuming, relationships between landslide area, depth, and volume are plagued by high uncertainties that carry over into estimates of erosion rates, and no widely accepted mechanistic model for sediment production and transport by landslides exists. The following chapters of this dissertation address these research gaps,

relying primarily on recently developed remote sensing data and mathematical modeling techniques.

The second chapter, coauthored with Dr. Josh Roering and Dr. J. Taylor Perron and published in the journal *Geomorphology* in 2009, improved the objectivity of landslide mapping by automating the process using traditional signal processing techniques with 1 meter resolution digital elevation models derived from Light Detection and Ranging (LiDAR). By systematically defining the spatial wavelengths of deep-seated landside features using two-dimensional Fourier and wavelet transforms, I was able to semi-automatically map landslides in study areas of similar sizes to standard USGS quadrangle maps with ~ 90% accuracy throughout the United States Pacific Northwest. The third chapter, coauthored with Dr. Josh Roering and published in the *Journal of Geophysical Research* in 2011, proposed a geomorphic transport law for these types of slow-moving, deep-seated landslides based on a mechanistic derivation of landslide sediment flux. This one-dimensional version of the transport law was able to accurately reproduce topographic profiles in a study area along the Eel River, northern California with different bedrock types, and predicted spatial patterns and overall erosion rates in agreement with independent observations. The final chapter, coauthored with Dr. Josh Roering and Dr. Alan Rempel and currently in review for the *Journal of Geophysical Research*, implemented this new transport law in a full two-dimensional numerical landscape evolution model and applied it to a study area in the Waipaoa catchment, North Island, New Zealand in addition to the Eel River site. Numerical experiments demonstrated how deep-seated landslides systematically reduce catchment

relief and lengthen hillslopes, as well as defined the weathering and landslide properties at which these effects were important.

This work addresses the two fundamental questions proposed above, but also pushes geomorphology in a new direction of using more quantitative techniques to improve observations of landforms and more rigorously infer the nature of the relevant geomorphic processes. This will propel the field to make more informed predictions about the socially relevant questions of landscape response to changes in climate, land use, and tectonic forcing over human to geologic time scales.

CHAPTER II

AUTOMATED LANDSLIDE MAPPING USING SPECTRAL ANALYSIS AND HIGH-RESOLUTION TOPOGRAPHIC DATA: PUGET SOUND LOWLANDS, WASHINGTON, AND PORTLAND HILLS, OREGON

Reproduced with permission from Booth, A., Roering, J., Perron, J.T. (2009). Automated landslide mapping using spectral analysis and high-resolution topographic data: Puget Sound lowlands, Washington, and Portland Hills, Oregon. *Geomorphology* 109, 132-147. doi:10.1016/j.geomorph.2009.02.027. Copyright 2009, Elsevier B.V.

1. Introduction

Creating detailed landslide inventory maps is a first step in assessing landslide hazards for policy-making purposes (Wieczorek, 1984), as well as in answering scientific questions involving spatial and temporal patterns of mass movement. Traditional landslide mapping methods include scanning topographic maps for opposing and irregular contours, interpreting aerial photographs using a stereoscope, and directly observing landslide morphology in the field (Nilsen and Brabb, 1977; Nilsen et al., 1979; Cruden and Varnes, 1996; Guzzetti et al., 1999; Wills and McCrink, 2002; Galli et al., 2008). However, each of these methods has limitations that may reduce the scope and accuracy of the resulting landslide map (Malamud et al., 2004a; Roering et al., 2005). Topographic maps often lack the resolution required to map small or topographically subtle landslides, while vegetation often obscures morphologic features indicative of landslides in aerial photographs. Detailed field mapping is time intensive and difficult to carry out in rugged, forested terrain (Van Den Eeckhaut et al., 2005). Furthermore, landslides located using any method must be translated to a paper or digital map, which introduces additional errors (Malamud et al., 2004a). For these reasons, landslide

inventories prepared by traditional means are often incomplete (Malamud et al., 2004b), and maps of a given area produced by different workers often differ dramatically (Guzzetti et al., 2000; Wills and McCrink, 2002; Galli et al., 2008). Use of incomplete or uncertain landslide inventories has clear implications for hazard assessment and may also skew the landslide distribution statistics used to estimate sediment production and transport (Hovius et al., 2000; Malamud et al., 2004a).

The increasing availability of high-resolution digital elevation models (DEMs) derived from airborne Light Detection and Ranging (LiDAR) measurements provides an additional tool for analyzing the geomorphic expression of deep-seated landslides over broad swaths of terrain. Airborne LiDAR can pierce vegetative cover and, with processing, reveal sub meter-scale features of the ground surface in many regions (Slatton et al., 2007). Many recent mapping efforts have taken advantage of LiDAR-derived DEMs to map landslides in forested terrain with improved results compared to traditional methods (Haugerud et al., 2003; Schulz, 2004, 2005, 2007; Van Den Eeckhaut et al., 2007a). Still, experts often disagree about which topographic features indicate landslides in a given LiDAR data set, and landslide mapping remains somewhat subjective (Guzzetti et al., 2000; Van Den Eeckhaut et al., 2005, 2007a).

An advantage of the high resolution of LiDAR-derived DEMs is that it allows more objective and quantitative analysis of fine-scale land surface features associated with a host of geomorphic processes, including landsliding. Several recent studies have illustrated how visual and statistical analyses of landslide topography can highlight patterns of surface deformation at specific sites (McKean and Roering, 2004; Chadwick et al., 2005; Glenn et al., 2006; Van Den Eeckhaut et al., 2007b). However, few studies

have utilized large, high resolution data sets to quantitatively investigate broad spatial patterns of landsliding (Hovius et al., 1997; Roering et al., 2005).

Here, we aim to develop new methodologies that utilize the Fourier and continuous wavelet transforms to automatically extract the topographic signatures of past deep-seated landslides from high-resolution topographic data. Specifically, variations in spectral power within spatial frequency bands characteristic of deep-seated landslides allow us to efficiently produce accurate kilometer-scale, deep-seated landslide maps. We also generate dominant wavelength maps and demonstrate their effectiveness in analyzing meter-scale topographic expressions of landslide mechanics, past landslide activity, and landslide-modifying geomorphic processes such as soil creep.

2. Study areas

We selected two main study areas — the Tualatin Mountains, Oregon, and the Puget Sound lowlands, Washington — based on the availability of high-resolution, LiDAR-derived DEMs and detailed, independently compiled landslide inventory maps. Figs. 1–3 show LiDAR-derived hillshade maps of the study areas, which we divide into five smaller sections for analysis: the Dixie Mountain quadrangle (DMQ) and northwest Dixie Mountain quadrangle (NWD), Oregon (Fig. 1), marine Thurston County (MTC) and the Carlyon Beach Peninsula (CBP), Washington (Fig. 2), and Seattle (SEA), Washington (Fig. 3). Although the independently compiled inventory maps represent workers' interpretations of landslide features and are therefore not completely objective, they are the most current maps of our study areas and provide an outside standard with which we compare our algorithm performance. Portions of the study areas contain debris

flow deposits and shallow landslides, but we focus specifically on the morphologic signatures of deep-seated landslide processes in this study.

2.1. Tualatin Mountains, Oregon

The Dixie Mountain quadrangle contains the NW–SE trending Tualatin Mountains, which drop 300 m or more in elevation to the Columbia River floodplain in the northeastern part of the quadrangle. Bedrock consists primarily of deeply weathered Columbia River flood basalts, which unconformably overlie weathered marine sandstone and siltstone of the Scappoose Formation (Trimble, 1963). An ~ 10–30 m blanket of loess accumulated during the late Pleistocene and is preserved on many of the high, low-angle ridges (Trimble, 1963; Madin and Niewendorp, 2008). This loess-mantled surface appears smooth in the LiDAR-derived hillshade map and is especially well-preserved along the spine of the Tualatin Mountains (along the SW edge of Fig. 1). Large landslide complexes occupy most of the northeastern slopes of the Tualatin Mountains where rivers have cut through the basalt and exposed the underlying Scappoose Formation (Trimble, 1963). Primary failure planes of the landslide complexes typically occur in weak layers of the Scappoose Formation at least tens of meters below the present surface (Madin and Niewendorp, 2008). In the LiDAR-derived hillshade map (Fig. 1), surfaces of these deep-seated landslides appear rough with many scarps, blocks undergoing tensile failure, and flow-like features clearly visible.

We acquired a LiDAR-derived DEM with 3-ft (0.9-m) point spacing of the Dixie Mountain quadrangle from the Oregon LiDAR Consortium (<http://www.oregongeology.com/sub/projects/olc/>). Madin and Niewendorp (2008) used

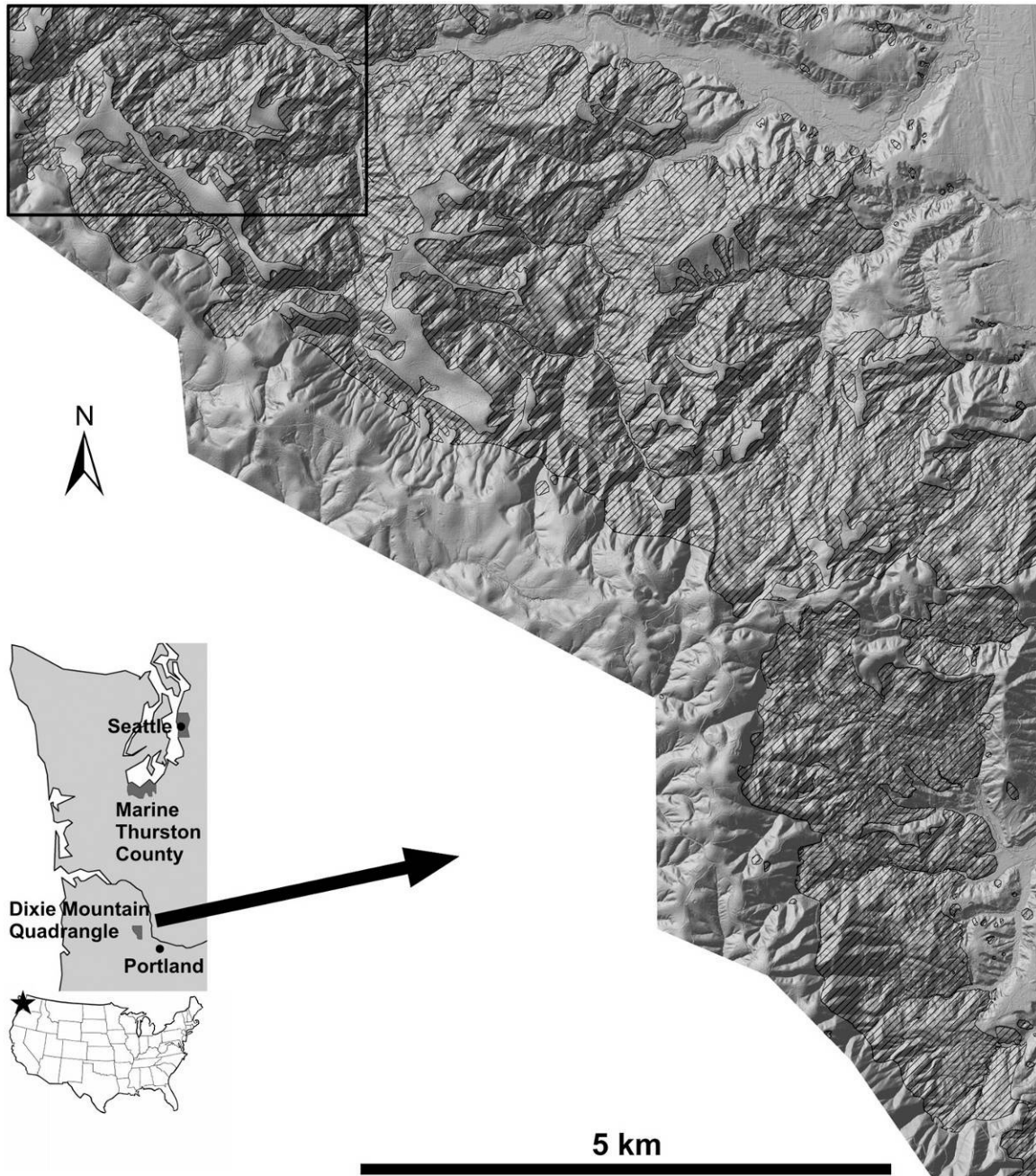


Fig. 1. LiDAR-derived hillshade map of the Dixie Mountain quadrangle, Oregon (DMQ) study area with deep-seated landslides independently mapped by Madin and Niewendorp (2008) shown in black, hatched pattern. The black rectangle in the NW corner outlines the Northwest Dixie Mountain quadrangle (NWD) study area, which we show in detail to illustrate our methods and results in Figs. 5 and 8.

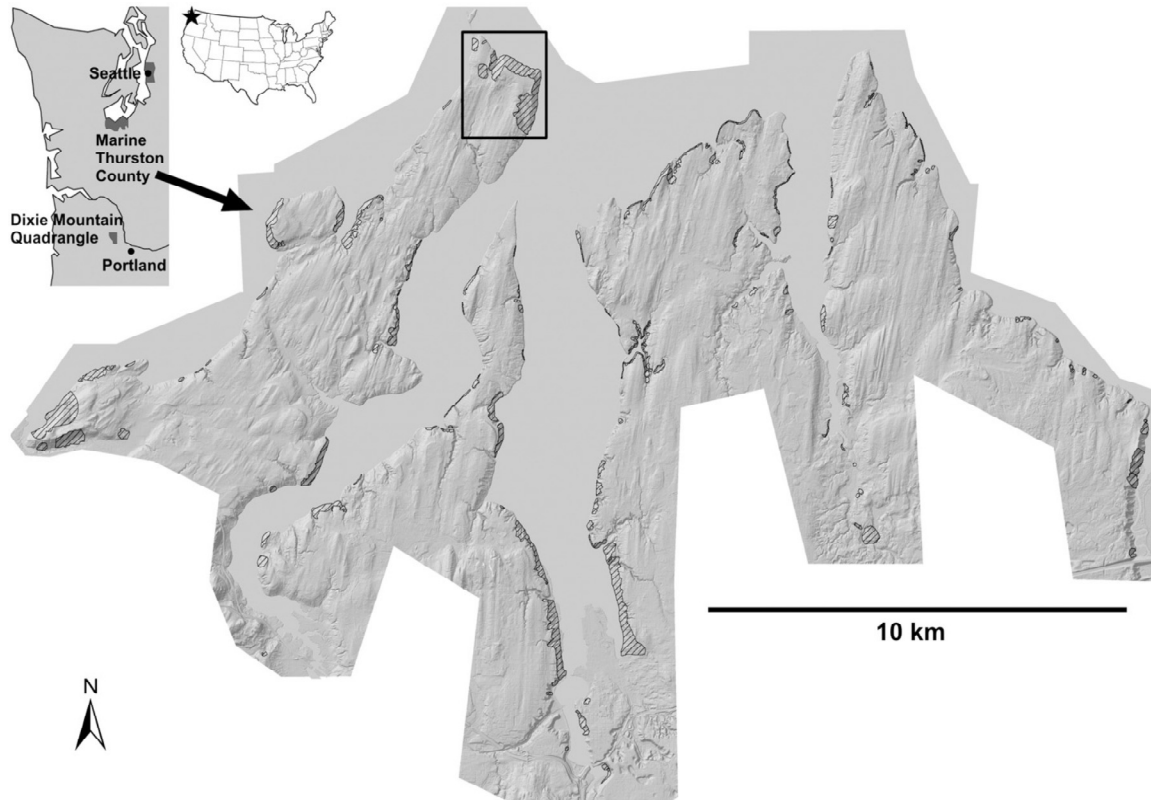
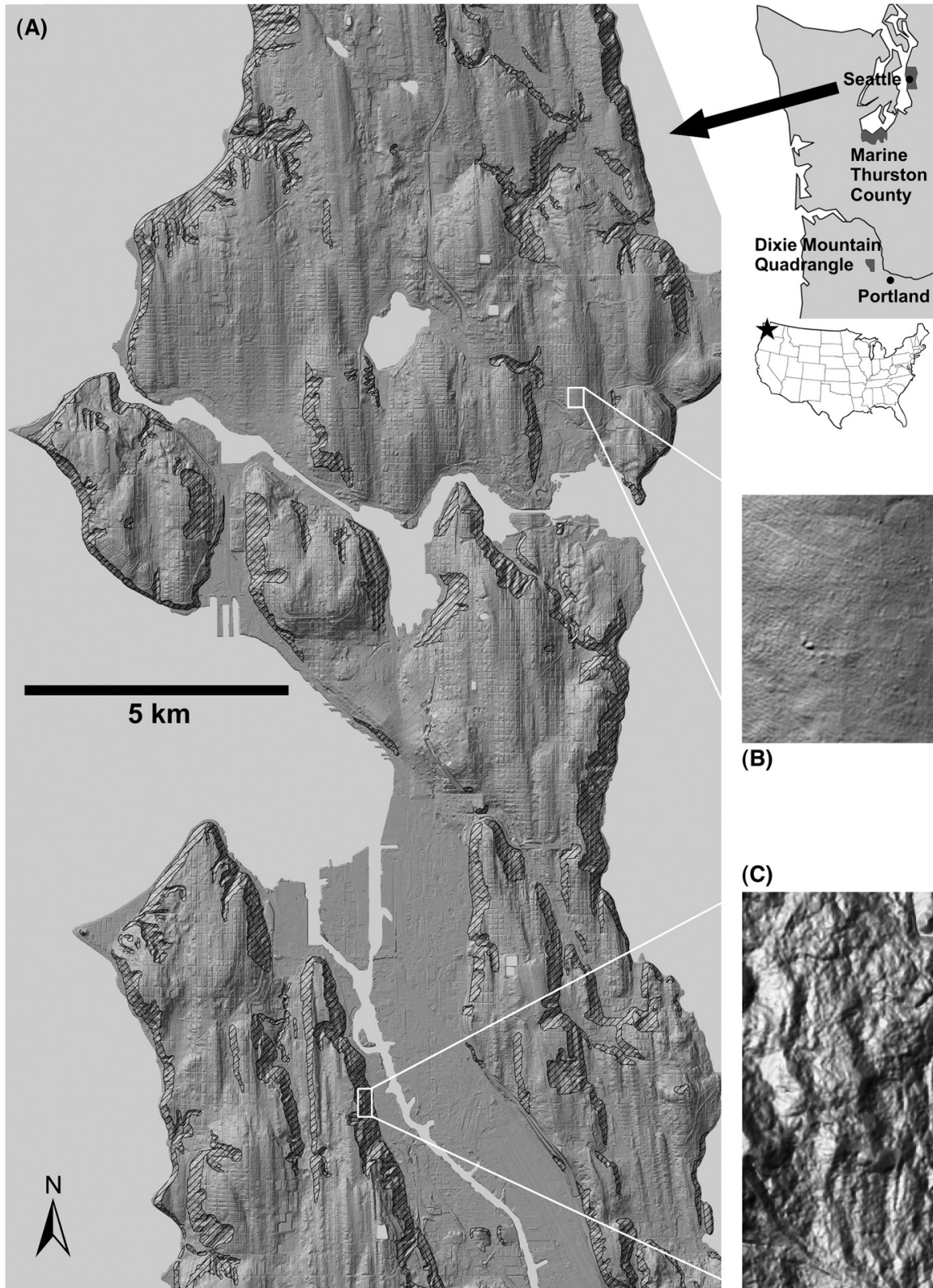


Fig. 2. LiDAR-derived hillshade map of the marine Thurston County, Washington (MTC) study area with deep-seated landslides independently mapped by M. Polenz (WA DNR, personal communication, 2008) shown in black, hatched pattern. The black rectangle in the north-central part of the figure outlines the Carlyon Beach Peninsula (CBP) study area, which we show in detail to illustrate our methods and results in Figs. 6, 9, and 12.

Fig. 3. (Next Page). (A) LiDAR-derived hillshade map of the Seattle, Washington (SEA) study area, with deep-seated landslides independently mapped by Schulz (2004, 2005, 2007) shown in black, hatched pattern. Boxes (B) and (C) indicate the patches of unfailed and failed terrain, respectively, used to compute the power spectra described in Section 3.3 and shown in Fig. 7 for the SEA study area.



field observations and interpretation of geomorphic features on a LiDAR-derived DEM to produce both a bedrock map and a surface deposit map of the quadrangle. LiDAR-derived DEMs were not available for previous mapping of the surrounding areas (Beeson et al., 1989, 1991), and previous maps included only bedrock units or a mix of bedrock units and surface deposits. In their surface map, Madin and Niewendorp (2008) classify landslide deposits based on style, age, and composition into five units: flow and fan deposits, surficial landslides, bedrock landslides, the Wildwood landslide complex, and the Dutch Canyon landslide complex. In our analysis of the DMQ and NWD study areas (Fig. 1), we use only deep-seated landslide units including bedrock landslides and the Wildwood and Dutch Canyon landslide complexes, which cover 53% of DMQ and 80% of NWD.

2.2. Puget Sound lowlands, Washington

The stratigraphy and surface morphology of most of the southern Puget Sound lowlands reflect the most recent interglacial–glacial cycle (Tubbs, 1974, 1975; Galster and Laprade, 1991; Haugerud et al., 2003). Nonglacial clay, silt, and sand deposited during the Olympia interglacial underlie glacial sediments of the Vashon stage of the Fraser glaciation (Armstrong et al., 1965; Booth, 1987). These loosely consolidated sediments are commonly exposed in 50-m or higher bluffs that truncate a glacially sculpted upland surface (Galster and Laprade, 1991; Schulz, 2004, 2007). In the LiDAR-derived hillshade maps (Figs. 2 and 3), this upland surface appears broadly undulating with many elongate, N–S trending drumlins. Following glaciation, isostatic rebound elevated the glacially sculpted surface while eustatic sea level and lake levels rose (Booth, 1987), undercutting adjacent slopes (Tubbs, 1974, 1975; Schulz, 2004, 2005,

2007). Coastal erosion, accomplished largely by deep-seated landsliding, resulted. Topographic features of these bluff-forming landslides, such as headscarps, slumped blocks, and hummocky topography, are visible both in the field and in the LiDAR-derived topographic data (Figs. 2 and 3) throughout much of the coastal Puget Sound lowlands.

High-resolution DEMs with 6-ft (1.8-m) point spacing for the Puget Sound lowlands are available from the Puget Sound LiDAR Consortium (<http://pugetsoundlidar.ess.washington.edu/>). As part of an ongoing landslide hazard project by the Geology and Earth Resources division of the Washington State Department of Natural Resources (WA DNR), M. Polenz (WA DNR, personal communication, 2008) recently compiled a landslide inventory for the marine shores of Thurston County using LiDAR-derived DEMs coupled with aerial photographs and field reconnaissance. The inventory includes both deep-seated and surficial landslides with brief descriptions of more than 800 landslide polygons. In our analysis of the MTC and CBP study areas (Fig. 2), we use only the large, deep-seated landslides, which cover 4% of MTC and 26% of CBP. Schulz (2004, 2005, 2007) created a detailed deep-seated landslide map for the city of Seattle by using LiDAR-derived DEMs and field observations to map headscarps, landslide bodies, and denuded slopes associated with ancient deep-seated landslides. In our analysis of the SEA study area (Fig. 3), we use all three of these features, which cover 15% of SEA.

3. Methods

We utilize two common signal processing techniques — the two dimensional discrete Fourier transform (2D DFT) and the two dimensional continuous wavelet transform (2D CWT) — to quantify the topographic expressions of deep-seated landslides and to objectively map their locations in our study areas. Fourier analysis has a rich history in the earth sciences and has been used to quantify various topographic patterns and landscape-scaling properties (Rayner, 1972; Hanley, 1977; Harrison and Lo, 1996; Perron et al., 2008). Wavelet analysis has recently gained popularity among those studying earth and planetary surface morphology and has successfully been implemented in studies that, for example, analyze polar topography (Malamud and Turcotte, 2001), quantify salmon nesting patterns (McKean et al., 2008), extract channel networks (Lashermes et al., 2007), and analyze morphotectonic lineaments (Jordan and Schott, 2005). The 2D DFT transforms discretely sampled data from the spatial domain to the frequency domain, providing information about how the amplitude of topographic features is distributed over a range of spatial frequencies. The 2D CWT transforms spatial data into position-frequency space, providing information about how amplitude is distributed over spatial frequency at each position in the data. We use both these transforms to determine characteristic wavelengths of landslide features and then to map where the signatures of these features are strongest. Throughout this paper we use spatial scale and wavelength interchangeably, and we refer to the inverse of a feature's wavelength as its spatial frequency. To assess the accuracy of our landslide mapping algorithms, we evaluate how well the algorithm outputs match the independently mapped deep-seated landslides in each study area. These independently compiled maps are

somewhat subjective as are all landslide inventory maps. However, they were created using previously unavailable high-resolution DEMs in addition to traditional methods and therefore are the most accurate deep-seated landslide maps available for our study areas.

We coded and executed all computations on a desktop computer using Matlab Version 7.4.0 (TheMathWorks, Inc.), so the methods should be accessible to all interested parties. Copies of our algorithms are available at <http://www.uoregon.edu/~jroering/specmaptools.html>.

3.1. 2D DFT

Two-dimensional Fourier analysis of topography provides quantitative information about the amplitude, orientation, and shape of periodic and quasiperiodic features over a range of spatial frequencies (Rayner, 1972; Hanley, 1977; Harrison and Lo, 1996; Perron et al., 2008). The 2D DFT of a data set $z(x,y)$ with $N_x \times N_y$ evenly spaced nodes is (Priestley, 1981; Perron et al., 2008)

$$Z(k_x, k_y) = \sum_{m=0}^{N_x-1} \sum_{n=0}^{N_y-1} z(m\Delta x, n\Delta y) e^{-2\pi i \left(\frac{k_x m}{N_x} + \frac{k_y n}{N_y} \right)}, \quad (1)$$

where k_x and k_y are wavenumbers in the x - and y -directions, Δx and Δy are grid spacings in the x - and y -directions, and m and n are indices in z . A common way of estimating the power spectrum of Z is the DFT periodogram,

$$V_{DFT} = \frac{1}{N_x^2 N_y^2} |Z(k_x, k_y)|^2, \quad (2)$$

which has units of amplitude squared, and when summed over all wavenumbers is equal to the variance of z by Parseval's theorem. The DFT periodogram produces a 2D array of values that describes the amplitudes of the frequency components of z . For the purposes

of automated landslide mapping, Eq. (2) therefore provides a measure of the amplitude of the topographic features in a DEM, such as hummocks and slumped blocks, at particular wavelengths and orientations.

3.2. 2D CWT

The generalized 2D CWT of $z(x,y)$ at wavelet scale parameter s and location (a,b) is (Kumar and Foufoula-Georgiou, 1994, 1997; Addison,2002)

$$C(s, a, b) = \frac{1}{s} \int_{-\infty}^{\infty} \int_{-\infty}^{\infty} z(x, y) \psi\left(\frac{x-a}{s}, \frac{y-b}{s}\right) dx dy, \quad (3)$$

where ψ represents a wavelet family. The 2D CWT is a convolution of z and ψ , and thus the wavelet coefficient $C(s,a,b)$ provides a measure of how well the wavelet ψ matches the data z at each node. When s is large, ψ is spread out and takes into account long wavelength features of z ; when s is small, ψ is more localized in space and sensitive to fine-scale features of z . We follow the convention of defining the wavelength or equivalent spatial scale of ψ as the inverse of its band-pass frequency (Kumar and Foufoula-Georgiou, 1997; Torrence and Compo, 1998), as illustrated in Fig. 4.

Because its shape resembles that of a landslide hummock, we use the 2D Mexican hat wavelet, described by the following equation and illustrated in Fig. 4, for our analyses:

$$\psi(x, y) = (2 - x^2 - y^2) e^{-\frac{1}{2}(x^2 + y^2)}. \quad (4)$$

The Mexican hat is proportional to the second derivative of a Gaussian envelope and has a wavelength of $2\pi s/(5/2)^{1/2}$ times the grid spacing (Torrence and Compo, 1998).

Convolving the 2D Mexican hat wavelet with a topographic data set therefore precisely

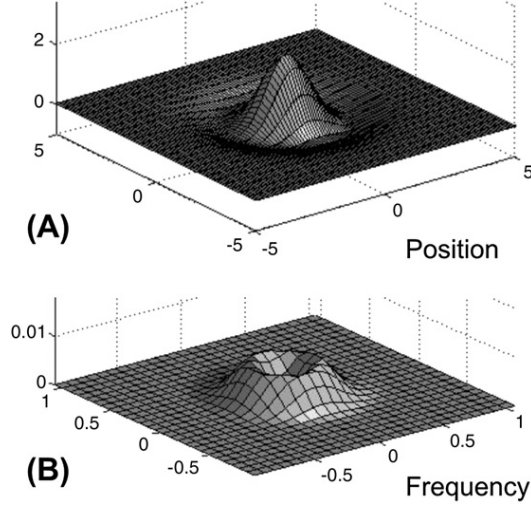


Fig. 4. (A) Two-dimensional Mexican hat wavelet ($s = 1$), and (B) its Fourier transform. In (B), radial frequency increases, and wavelength decreases, with distance from the center of the square array. The ring-shaped peak in (B) indicates the dominant frequency of the Mexican hat wavelet, which is the inverse of its wavelength or equivalent spatial scale. Note that in (B) the Mexican hat is spread out and contains additional frequencies on either side of its main frequency.

maps features of specific wavelengths and amplitudes, including characteristic landslide features.

The 2D CWT can also be condensed into a power spectrum by computing its variance over $N_a \times N_b$ nodes at each wavelet scale (Percival, 1995):

$$V_{CWT}(s) = \frac{1}{2N_a N_b} \sum_a \sum_b |C(s, a, b)|^2. \quad (5)$$

Similar to a Fourier power spectrum, Eq. (5) provides a general measure of how the amplitude of features changes with frequency over an entire data set. However, as shown for the 2D Mexican hat wavelet in Fig. 4, a wavelet of a given scale typically contains a range of frequencies on either side of its main band-pass frequency. Analyzing a single wavelet scale with the continuous wavelet transform is therefore sensitive to a range of frequencies, while the discrete Fourier transform analyzes individual frequencies

separately. This has the effect of smoothing the peaks in a wavelet power spectrum compared to its Fourier counterpart (Torrence and Compo, 1998).

3.3. *Fourier and wavelet spectra*

To determine the characteristic wavelengths of deep-seated landslide features in each study area, we first select representative patches of mapped deep-seated landslides and unfailed terrain. In Seattle, we use a portion of the Riverview landslide and the glacially sculpted upland surface of Calvary Cemetery as representative patches (Fig. 3B and C). For the Dixie Mountain quadrangle, we use a section of the Dutch Canyon landslide complex and a nearby smooth, loess mantled surface (Fig. 5). For marine Thurston county, we use the historically active Carlyon Beach landslide and the neighboring glacially sculpted upland surface (Fig. 6).

Next, we normalize each patch of terrain to have unit variance and generate Fourier and wavelet power spectra using Eqs. (2) and (5), respectively (Fig. 7A–C, G–I). For easier visualization, we condense the 2D array produced by Eq. (2) to a 1D power spectrum by plotting V_{DFT} against radial frequency $(f_x^2 + f_y^2)^{1/2}$. The spectra all show spectral power decreasing with spatial frequency, but the spectra tend to diverge over specific ranges of frequencies. In the DFT-generated spectra, unfailed terrain tends to have higher spectral power at high frequencies, and deep-seated landslides tend to have higher spectral power at intermediate frequencies. In the CWT-generated spectra, both types of terrain have similar spectral power at low and high frequencies, but deep-seated landslides tend to have higher spectral power at intermediate frequencies. These patterns indicate that deep-seated landsliding in our study areas tends to transfer spectral power from low and high frequencies to intermediate frequencies. Mechanisms that concentrate

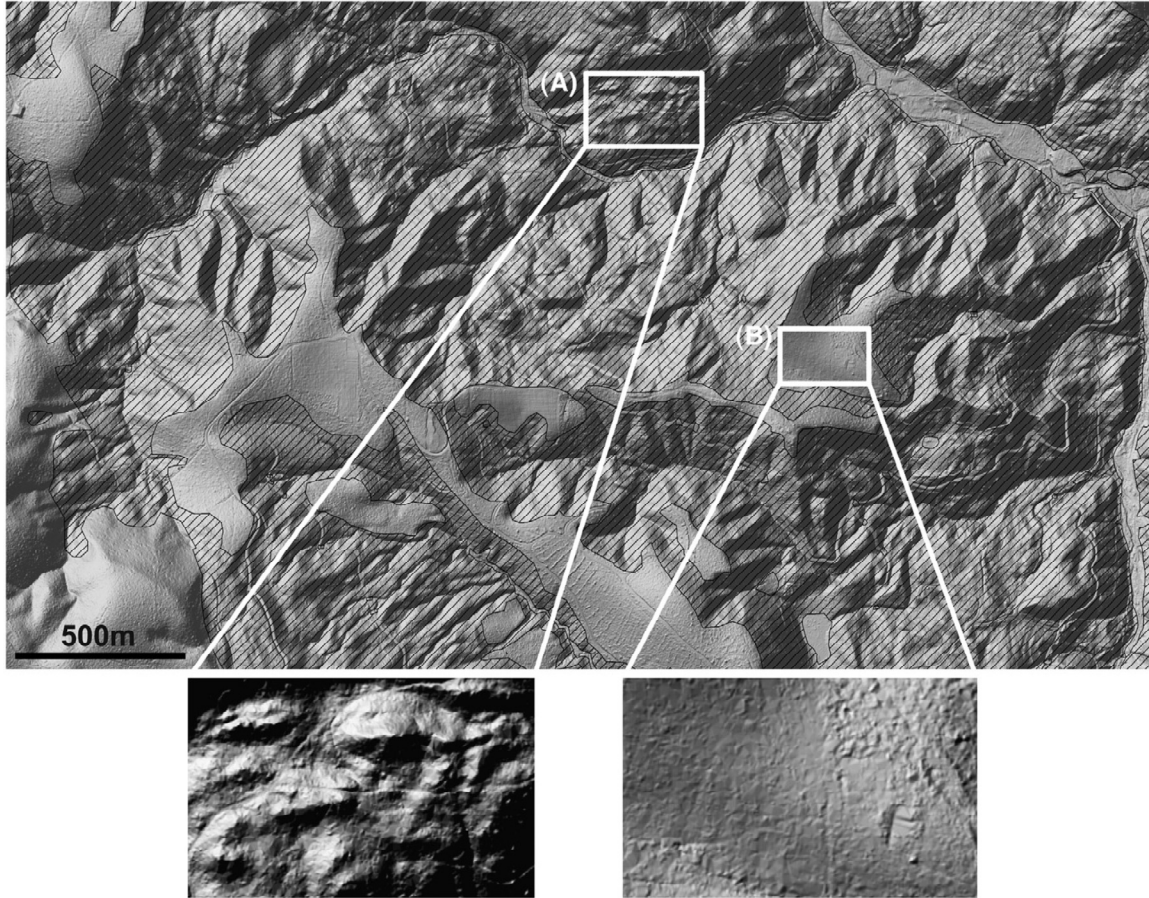


Fig. 5. LiDAR-derived hillshade map of the NWD study area with independently mapped, deep-seated landslides (Madin and Niewendorp, 2008) shown in black, hatched pattern. White boxes (A) and (B) indicate the patches of landslide and unfailed terrain, respectively, used to compute the normalized power spectra described in Section 3.3 and shown in Fig. 7 for the NWD and DMQ study areas.

spectral power include failure of coherent blocks of material separated by scarps in the upper portion of the landslides and folding from compressive stress in the lower portions.

To more clearly highlight the frequency bands over which deep-seated landslides tend to concentrate spectral power, we normalize the landslide-generated spectra by their corresponding unfailed surface-generated spectra (Fig. 7D–F, J–L). All six normalized spectra produce well-defined peaks that indicate the characteristic wavelengths of deep-seated landslide features in similar substrates in each study area. The peaks of the spectra indicate a characteristic wavelength of ~22 m for the Dixie Mountain quadrangle and

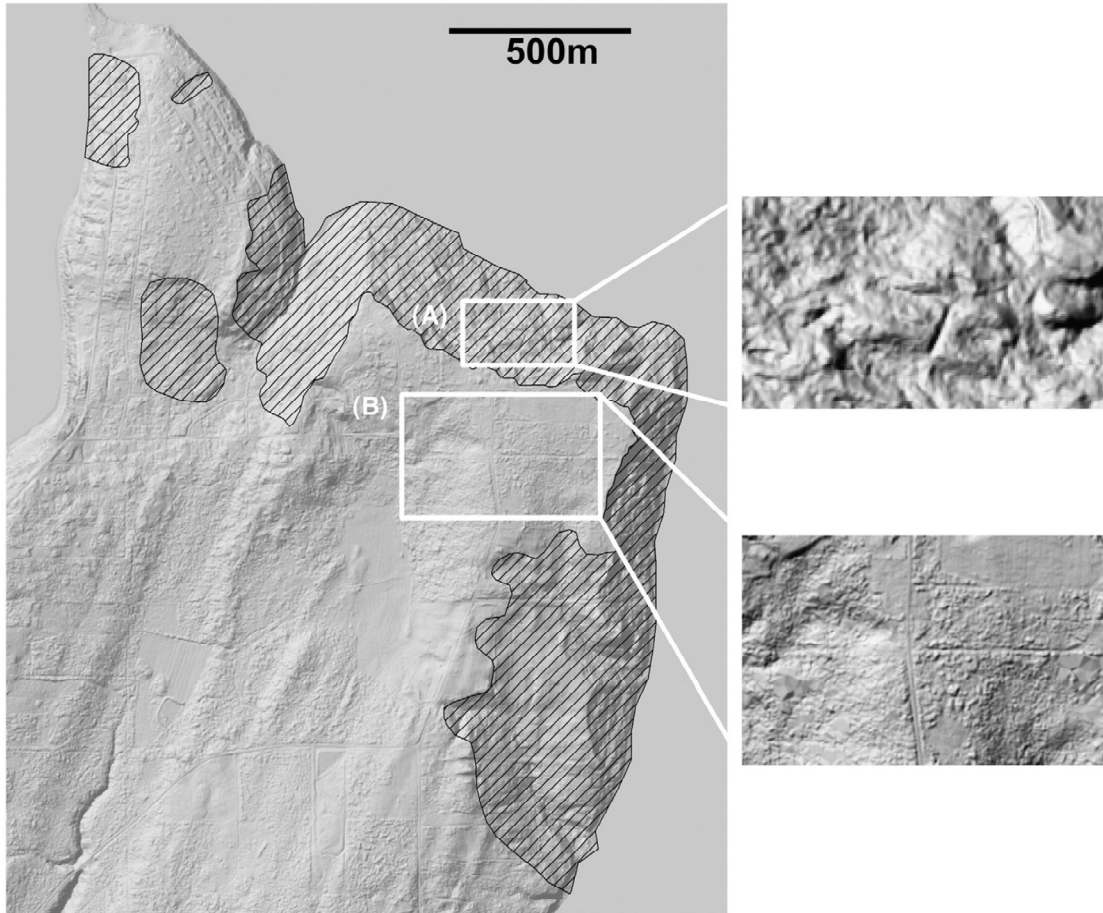
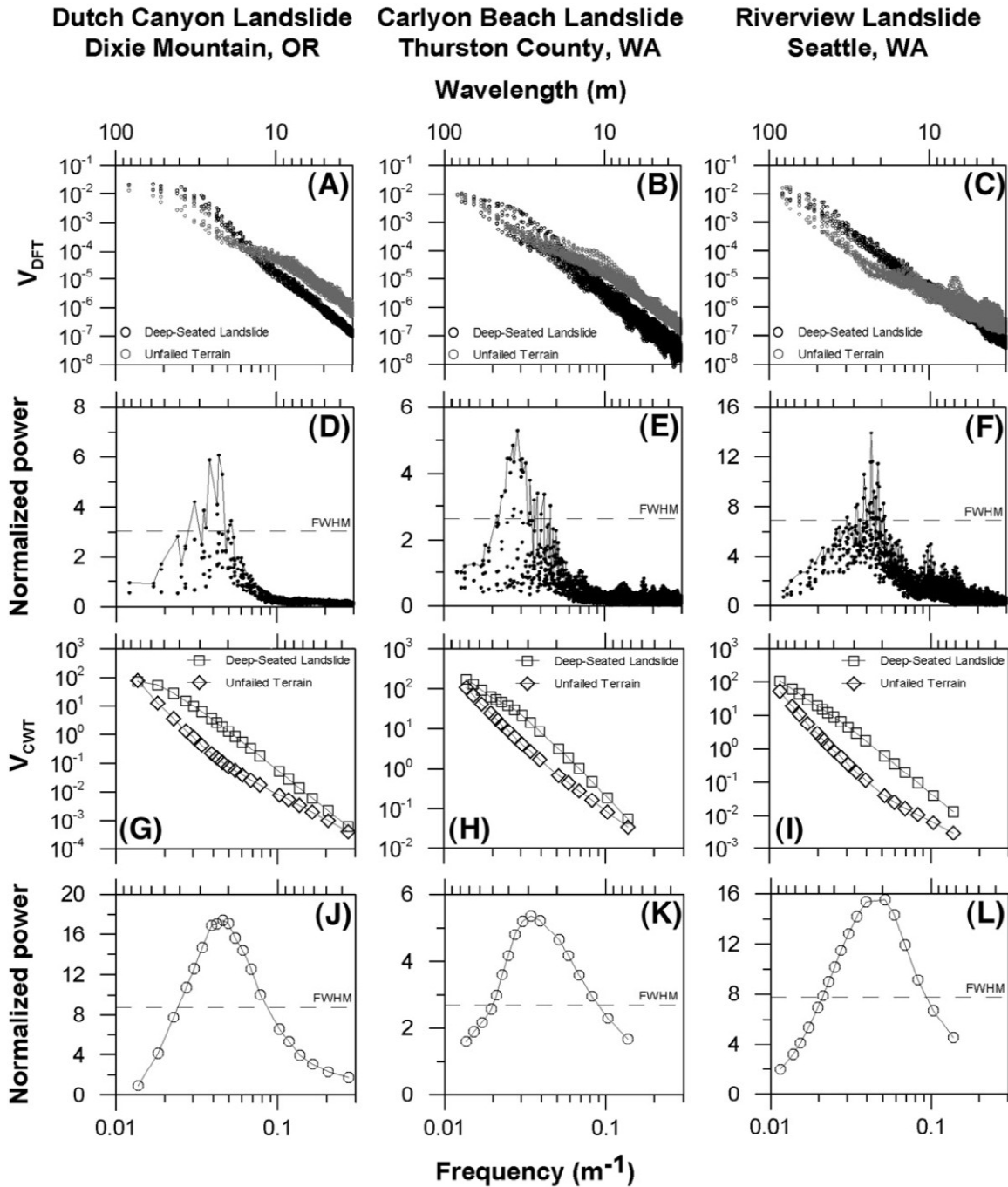


Fig. 6. LiDAR-derived hillshade map of the CBP study area with independently mapped, deep-seated landslides (M. Polenz, WA DNR, personal communication, 2008) shown in black, hatched pattern. White boxes (A) and (B) indicate the patches of landslide and unfailed terrain, respectively, used to compute the power spectra described in Section 3.3 and shown in Fig. 7 for the CBP and MTC study areas.

Fig. 7. (Next Page). Power spectra indicating the frequency bands characteristic of deep-seated landslides in the DMQ and NWD study areas (left-hand column), the MTC and CBP study areas (center column), and the SEA study area (right-hand column). Fourier power spectra (A–C) show that spectral power tends to decrease with increasing frequency in both unfailed and deep-seated landslide terrain. The peaks of the normalized Fourier spectra (D–F) highlight discrepancies in spectral power between deep-seated landslides and unfailed terrain, indicating the range of frequencies over which deep-seated landslides tend to concentrate spectral power. Solid lines highlight the upper envelopes of the normalized spectra, and dashed lines indicate the full width at half maximum (FWHM) for each spectrum. The wavelet power spectra (G–I) confirm that spectral power decreases with frequency, and the peaks of the normalized wavelet spectra (J–L) also highlight the bands of frequencies over which deep-seated landslides concentrate spectral power. All patches of terrain were normalized to have unit variance before computing spectral power.



Seattle, and ~32 m for marine Thurston County, with negligible differences in peak location between the Fourier and wavelet spectra.

Because landslide features occur over a range of wavelengths in both study areas, as indicated by both observation and Fig. 7, we take the full width at half maximum

(FWHM) of each peak as a straightforward measure of the spectrum's spread and use this characteristic band of spatial frequencies in our mapping algorithms. For the Dixie Mountain quadrangle, the Fourier and wavelet spectra indicate characteristic frequency bands of ~ 0.029 to 0.055 m^{-1} (wavelengths of ~ 18 to 34 m) and of ~ 0.022 to 0.09 m^{-1} (wavelengths of ~ 11 to 45 m), respectively. For marine Thurston County, the normalized Fourier spectrum indicates a characteristic frequency band of ~ 0.020 to 0.048 m^{-1} (wavelengths of ~ 21 to 50 m), while the normalized wavelet spectrum indicates a band of frequencies from ~ 0.020 to 0.09 m^{-1} (wavelengths of ~ 11 to 50 m). In Seattle, the normalized Fourier spectrum defines a characteristic frequency band of ~ 0.030 to 0.053 m^{-1} (wavelengths of ~ 19 to 33 m), and the normalized wavelet spectrum defines a band of frequencies from ~ 0.020 to 0.090 m^{-1} (wavelengths of ~ 11 to 50 m). At all three sites, the FWHM is broader in the wavelet spectrum because each wavelet scale consists of a range of frequencies. At small wavelet scales in particular, the Mexican hat wavelet becomes more spread out in the frequency domain, causing the right-hand sides of the wavelet spectra in Fig. 7 to differ considerably from their analogous Fourier spectra.

3.4. Mapping spectral power

In order to automatically map terrain with features indicative of past deep-seated landslides, we map spatial patterns of spectral power contained within the frequency bands determined from Fig. 7 using the transforms described in Sections 3.1 and 3.2.

3.4.1. Windowed 2D DFT

To map spatial patterns of spectral power with Fourier analysis, we implement the 2D DFT in a windowed mode. The algorithm systematically works its way through the

DEM computing the DFT periodogram using Eq. (2) within a square window centered on each node. The values of the periodogram calculated at each node are then summed over the characteristic frequency band, and this spectral power sum is displayed in mapview for analysis. A node with a high spectral power sum indicates a strong topographic signature of deep-seated landsliding within the window surrounding that node.

For both study areas we use a 63-by-63 node window, corresponding to a 115-by-115 m square of terrain in the Puget Sound lowlands (study areas MTC, CBP, and SEA) and a 58-by-58 m square of terrain in the Dixie Mountain quadrangle (study areas DMQ and NWD). In a window this size, the 2D DFT samples 64 evenly spaced frequencies ranging from zero to $(2\Delta)^{-1}$, the Nyquist frequency, in both the x - and y -directions, placing the frequencies of interest near the middle of the spectrum. This choice of window size also represents a balance between sampling enough frequencies to sufficiently describe the terrain and keeping computation times reasonable.

3.4.2. 2D CWT

Because wavelet analysis preserves information about both scale and position, we implement Eq. (3) directly to map spatial patterns of spectral power with the 2D CWT. We identify wavelet scales corresponding to the minimum and maximum frequencies in each study area's characteristic frequency band (Fig. 7J–L) and analyze only integer wavelet scales between and including these bounds. This choice of scales adequately encompasses the frequencies of interest in each landscape while keeping computation times short. The algorithm first computes a wavelet coefficient at each node in the DEM at each wavelet scale. It then squares and sums the computed wavelet coefficients at each node and displays the outcome in mapview. A node with a high value indicates

topography characteristic of a deep-seated landslide at that node. Because the 2D CWT is not windowed as is our 2D DFT algorithm, we smooth the output of our 2D CWT algorithm by averaging within a 63-node diameter window in order to produce comparable maps that illustrate broad patterns of past deep-seated slope instability.

3.5. *Optimizing algorithm outputs*

The most straightforward way to translate an array produced by the algorithms described in Sections 3.4.1 and 3.4.2 into a deep-seated landslide map is to classify each node in the array as a landslide if its spectral power sum is above a cutoff value or as an unfailed surface if its value is below the cutoff. This approach does not delineate boundaries of individual landslides that border or overlap each other, but instead indicates all nodes in the study area that have the topographic signature of deep-seated landsliding. The map resulting from a given cutoff value can then be compared to the independently mapped deep-seated landslides. Following Carrara et al. (1992), we select optimal cutoff values for each study area based on the overall error index

$$E = \frac{(A_1 \cup A_2) - (A_1 \cap A_2)}{(A_1 \cup A_2)}, \quad 0 \leq E \leq 1, \quad (6)$$

where A_1 and A_2 are the areas of landslides in the two maps being compared, and \cup and \cap represent the geometric union and intersection, respectively. The geometric union counts the total area of deep-seated landslides identified by the landslide inventory or by our algorithms, while the geometric intersection counts the total area identified as a deep-seated landslide by both the inventory and our algorithms. We compute E for each output array in each study area over a range of cutoff values, and select the best algorithm-produced landslide inventory map using the cutoff value that minimizes E . Nodes that

contain no data or are located within a body of water are not included in our optimization routines.

4. Results

4.1. Landslide maps

Arrays produced by applying our 2D DFT and 2D CWT algorithms to the study areas clearly highlight variations in spectral power contained in wavelengths characteristic of deep-seated landslides across broad areas of terrain (Figs. 8A and B, 9A and B, and 10A and C). Spectral power sums vary by orders of magnitude over each study area, reflecting considerable variation in the topography. Areas that are smooth over the range of spatial frequencies being analyzed (Fig. 7) have low spectral power, while areas that are rough over this frequency band have high spectral power. These areas of high spectral power tend to coincide with mapped deep-seated landslides, verifying that a cutoff spectral power sum can delineate landslide terrain.

In our five study areas, selecting an optimal cutoff spectral power sum by minimizing the error index correctly classifies an average of 82% of the land area as compared to the independently compiled landslide inventories (Table 1). The minima of the error index curves (Fig. 11) clearly indicate optimal cutoff spectral power sums for each study area. To the left of the minimum in each error index curve, large numbers of unfailed nodes are incorrectly classified as landslide nodes, keeping E high. To the right of the minimum, E is again high, but this time from landslide nodes being misclassified as unfailed nodes. In the vicinity of the optimal cutoff values, the error index curves are markedly lower in the Dixie Mountain quadrangle (DMQ and NWD) than in the Puget

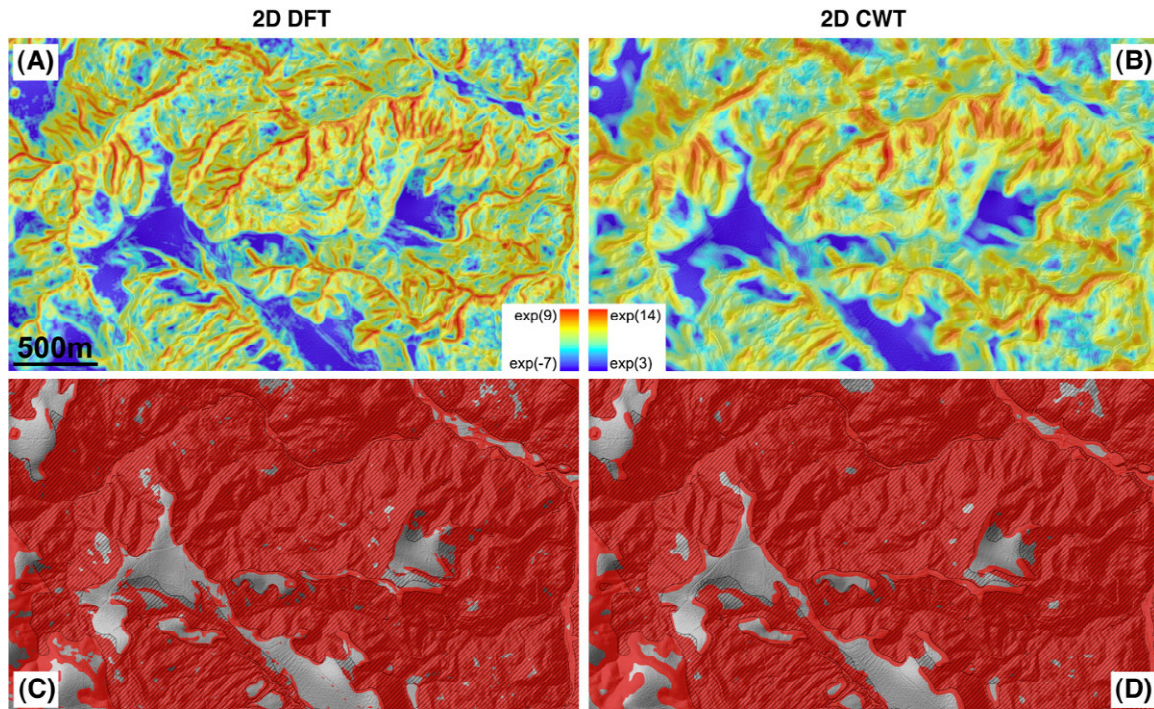
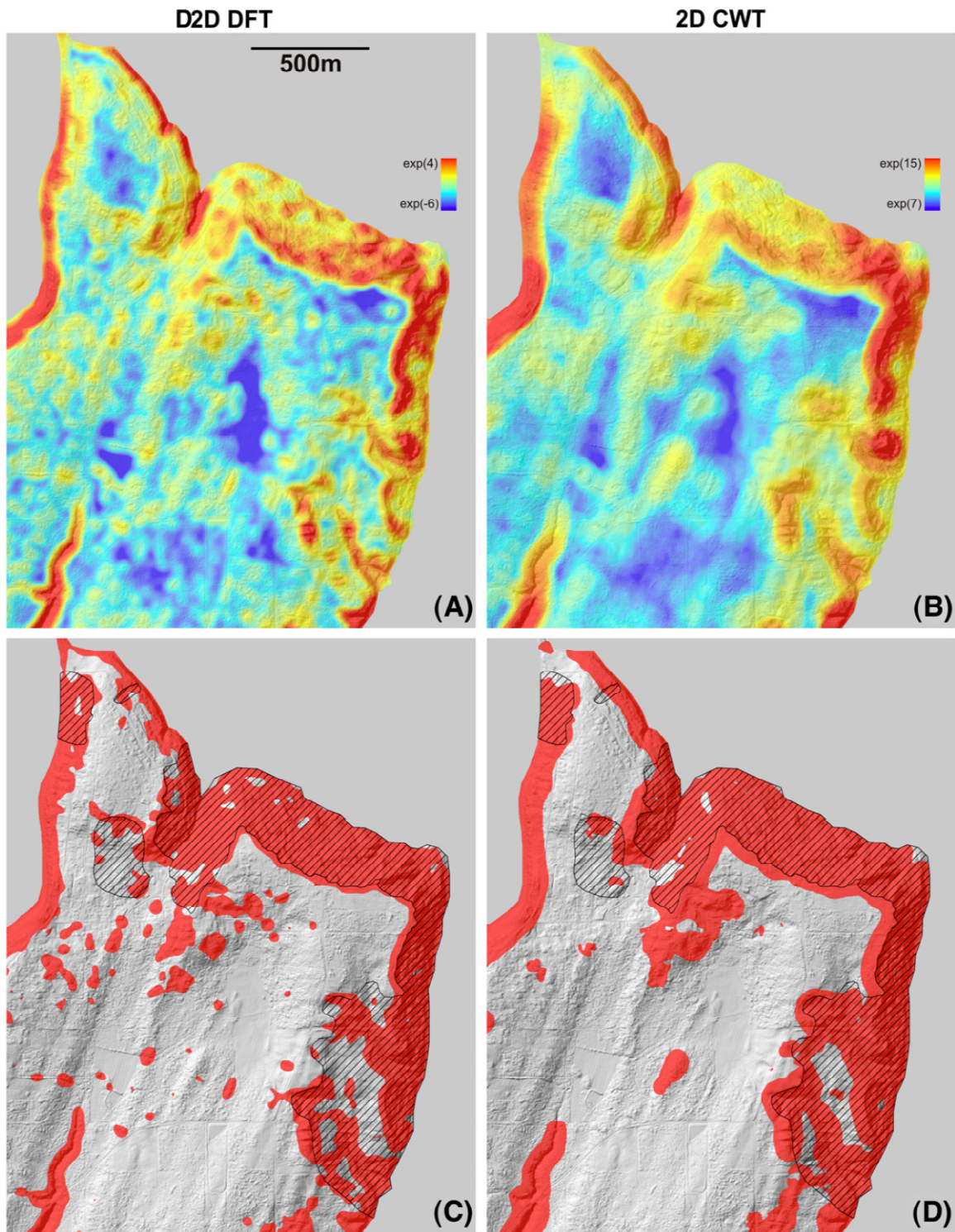


Fig. 8. Spectral power sums from the (A) 2D DFT and (B) 2D CWT and their corresponding optimally classified landslide maps (C and D) for the NWD study area. Warm colors (A and B) indicate strong topographic signals of deep-seated landslide terrain, while shaded red areas (C and D) delineate landslide terrain based on the optimal cutoff values (Table 1). Independently mapped deep-seated landslides (Madin and Niewendorp, 2008) are overlain in the black, hatched pattern.

Fig. 9. (Next Page) Spectral power sums from the (A) 2D DFT and (B) 2D CWT and their corresponding optimally classified landslide maps (C and D) for the CBP study area. Warm colors (A and B) indicate strong topographic signals of deep-seated landslide terrain, while shaded red areas (C and D) delineate landslide terrain based on the optimal cutoff values (Table 1). Independently mapped deep-seated landslides (M. Polenz, WA DNR, personal communication, 2008) are overlain in the black, hatched pattern.



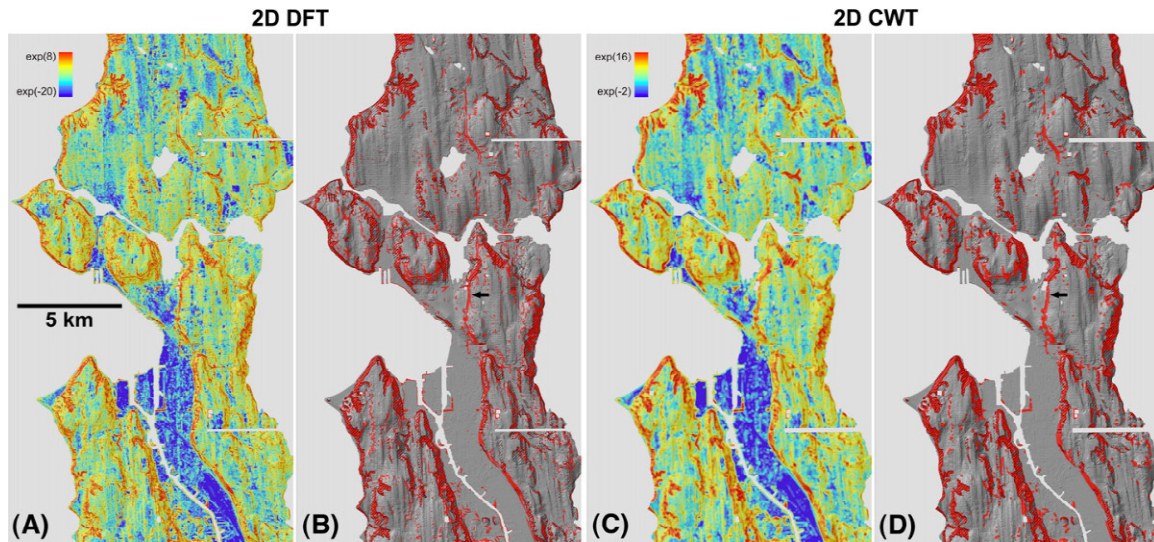


Fig. 10. Spectral power sums from the (A) 2D DFT and (C) 2D CWT and their corresponding optimally classified landslide maps (B and D) for the SEA study area. Warm colors (A and C) indicate strong topographic signals of deep-seated landslide terrain, while shaded red areas (B and D) delineate landslide terrain based on the optimal cutoff values (Table 1). Independently mapped deep-seated landslides (Schulz, 2004, 2005, 2007) are overlain in the black, hatched pattern. Small, black arrows (B and D) indicate the location of Interstate 5, which runs N–S through the study area and produces high spectral power sums because of its sharp edges. Grey, horizontal bars on the right-hand side of each image are areas of no data because of gaps in the LiDAR coverage.

Sound lowlands (MTC, CBP, and SEA) because landslides occupy a majority of the area in the Dixie Mountain quadrangle and only a small fraction of the area in the Puget Sound lowland study areas. Defining the best cutoff value as the spectral power sum that minimizes E produces visually appealing landslide maps (Figs. 8C and D, 9C and D, and 10B and D) and correctly classifies a high percentage of the land surface in our study areas (Table 1).

The error index curves shown in Fig. 11 and optimal cutoff values shown in Table 1 also highlight how the sizes of our data sets affect the optimal cutoff spectral power sums. Optimal cutoff values are similar for MTC, SEA, and CBP and for DMQ and NWD, but tend to be higher in the larger study areas. Our larger study areas tend to have

Table 1. Comparing algorithm-generated and independently compiled deep-seated landslide maps in each study area.

	Method	Study Area:				
		MTC	SEA	CBP	DMQ	NWD
Cutoff Value (m ²)	2D DFT:	2.86	1.88	0.65	0.33	0.22
	2D CWT:	2.6e+5	1.7e+5	5.9e+4	8.7e+3	5.3e+3
Error Index	2D DFT:	0.84	0.57	0.48	0.39	0.14
	2D CWT:	0.86	0.55	0.47	0.39	0.15
Percent Correct (%)	2D DFT:	88.8	87.1	81.3	68.3	87.0
	2D CWT:	86.1	87.8	80.5	67.8	86.0
Correctly Classified:						
Landslide Area (km ²), (True Positives)	2D DFT:	3.9	21.8	0.7	32.2	5.2
	2D CWT:	4.2	22.6	0.8	32.3	5.3
Unfailed Area (km ²), (True negatives)	2D DFT:	152.8	163.2	2.1	11.9	0.7
	2D CWT:	147.7	163.2	2.0	11.4	0.6
Incorrectly Classified:						
Landslide Area (km ²), (False Negatives)	2D DFT:	2.9	9.9	0.2	1.9	0.2
	2D CWT:	2.5	8.7	0.1	1.8	0.1
Unfailed Area (km ²), (False Positives)	2D DFT:	16.9	17.6	0.5	18.5	0.7
	2D CWT:	22.0	17.1	0.5	19.0	0.8
Total Area Analyzed (km ²)	2D DFT:	176.4	212.5	3.5	64.5	6.8
	2D CWT:	176.4	211.1	3.5	64.5	6.8

higher percentages of terrain mapped as unfailed, and this unfailed terrain inevitably has some topographic features that our algorithms interpret as deep-seated landslides, as discussed in the following paragraphs. Higher cutoff spectral power sums reduce the number of nodes in these large areas of unfailed terrain that are incorrectly classified as landslide nodes.

Although the optimized landslide maps produced by our algorithms succeed in mapping a large majority of the terrain in each study area correctly, some systematic misclassifications occur. The algorithms tend to falsely classify topographic features with sharp edges or spatial frequencies in the characteristic landslide band as landslide nodes. Conversely, the algorithms tend to overlook topographic features within the

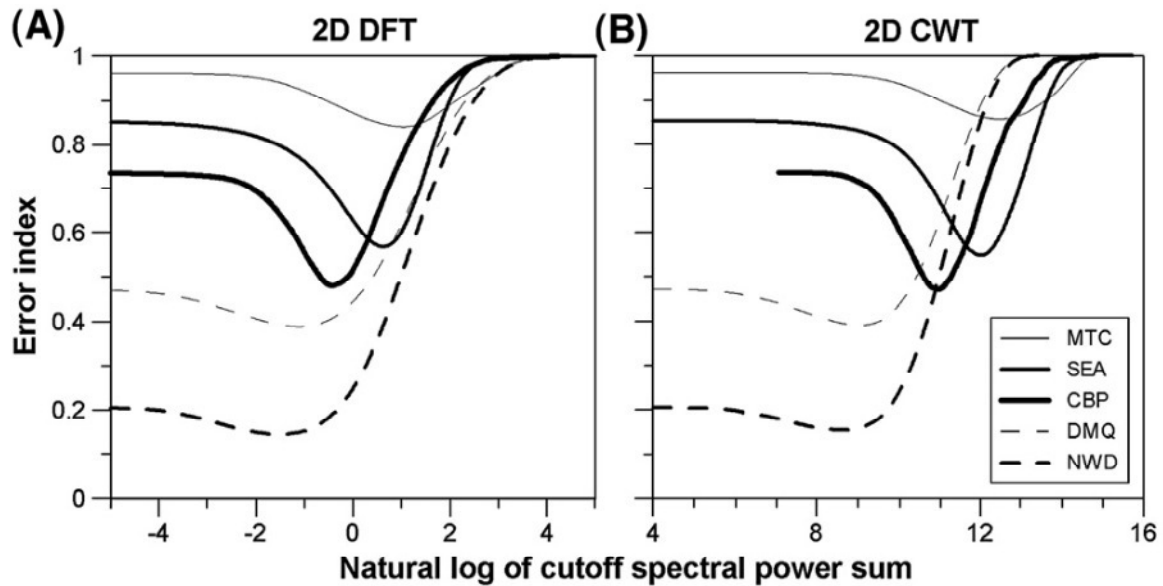


Fig. 11. Error index curves used to select optimal cutoff spectral power sums for classifying each algorithm-generated array with the (A) 2D DFT and the (B) 2D CWT. We computed E using 1500 logarithmically spaced cutoff values ranging from the minimum to maximum value in each array.

boundaries of known landslides that have subdued amplitudes due to non-landslide erosive processes or human modification of the landscape.

In our study areas, sharp-edged topographic features that tend to be misclassified as deep-seated landslides include narrow valley bottoms between landslide masses (north-central Fig. 8C and D), ravines (SW corner of Fig. 9C and D), edges of steep bluffs lacking deep-seated landslides (western Fig. 9C and D), and some roads (small arrow, Fig. 10B and D). These sharp edges produce high spectral power in Fourier analysis because large amplitude sine and cosine waves over a range of frequencies are required to capture abrupt changes in the data being analyzed. Any window in our analysis that contains an abrupt change in elevation therefore has an abnormally high spectral power sum. Wavelet analysis with the Mexican hat wavelet also tends to highlight sharp edges because of their high curvature. The Mexican hat wavelet is the

second derivative of a Gaussian envelope, so convolving a data set with the Mexican hat is akin to computing the data set's second derivative over a length scale proportional to the wavelet scale (Lashermes et al., 2007).

Topographic features in our study areas with wavelengths in the band characteristic of deep-seated landslides include some glacial features of the Puget Sound lowlands (center of Fig. 9C and D) and some fluentially dissected hillslopes in the Dixie Mountain quadrangle. Because these features have large amplitudes over the same wavelengths as deep-seated landslides, they produce high spectral power sums that lead to misclassification as landslide terrain.

In both study areas, landslides have a range of ages and activity levels, so the surfaces of different landslides have undergone different degrees of post-failure modification. Diffusive soil transport processes have likely subdued the topographic expression of many of the older landslides, shifting spectral power to longer wavelengths and making them difficult for our algorithms to detect. For example, our algorithms fail to capture part of the interior of the landslide mapped in the NE corner of Fig. 8C and D, and incorrectly classify the broad patch of smooth topography mapped as an ancient (M. Polenz, WA DNR, personal communication, 2008) deep-seated landslide in the SE corner of Fig. 9C and D. Anthropogenic modification of the landscape has also subdued many landslide morphologic features in our study areas, especially in the Puget Sound lowlands. Development within the mapped landslides on the slopes adjacent to the inlet on the northern shore of the Carlyon Beach peninsula (Fig. 9), for example, has likely removed many landslide features, preventing our algorithms from matching the mapped landslides in this area.

Despite these effects, our results show that automated landslide mapping methods can produce landslide maps with high degrees of precision in our study areas. The normalized spectra in Fig. 7 faithfully indicate the characteristic wavelengths of landslide morphologic features in similar substrates in each study area. The summed spectral power contained within these wavelengths quantifies the topographic signature of deep-seated landsliding at each node in a data set, allowing past deep-seated slope instability to be mapped.

4.2. Dominant wavelength map

In addition to analysis of broad spatial patterns, our methods allow node-by-node analysis of specific topographic features through the production of a dominant wavelength map. To produce the map, we compute wavelet coefficients using Eq. (3) for each study area over a range of wavelet scales and determine the mean wavelet coefficient over the entire area at each scale. The wavelet coefficients are then normalized by the mean at each scale, and the scale with the highest normalized wavelet coefficient is mapped as the dominant spatial scale at each node.

Fig. 12 shows the spatial distribution of dominant wavelength for mapped landslides in the CBP study area. Variations in dominant wavelength within the boundaries of these deep-seated landslides clearly highlight differences in landslide style and geomorphic processes. Most of the terrain within the historically active Carlyon Beach landslide (Fig. 12A) has dominant wavelengths within the characteristic band of ~ 11 to 50 m indicated by our normalized wavelet power spectrum (Fig. 7K). Very few nodes within the landslide are dominated by very short or very long wavelengths, illustrating the tendency of deep-seated landsliding to shift spectral power to intermediate

wavelengths. This may suggest that the initial deep-seated movement of the landslide occurred recently enough for its topographic signature to remain intact or that continued activity of the landslide has maintained its characteristic topographic expression. Nodes with similar dominant wavelength values within the landslide also tend to form continuous bands perpendicular to the local slope. These bands appear to reflect zones of tensile failure and block rotations that result from downslope movement of relatively coherent slide masses. These patterns in dominant wavelength differ from patterns in a nearby ancient (M. Polenz, WA DNR, personal communication, 2008) deep-seated landslide (Fig. 12B). At that site, longer wavelengths tend to dominate most nodes within the ancient landslide, marking a transition from deep-seated landsliding to subsidiary geomorphic processes. Specifically, diffusive soil transport processes appear to have reduced the amplitude of short wavelength features, leaving only longer wavelength expressions of past deep-seated landsliding, except where the landslide has been partly reactivated (small arrow, Fig. 12B). Also, fluvial processes acting in several channels have begun to dissect the ancient landslide mass at a larger spatial scale. Several of the long wavelength bands in the southern half of the ancient landslide trend NNW while the shoreline trends NNE. This likely reflects the dominant direction of fluvial transport and slope modification across the ancient landslide surface or indicates that large-scale blocks in the landslide failed in a direction not perpendicular to the modern shoreline, perhaps due to directed coastal erosion.

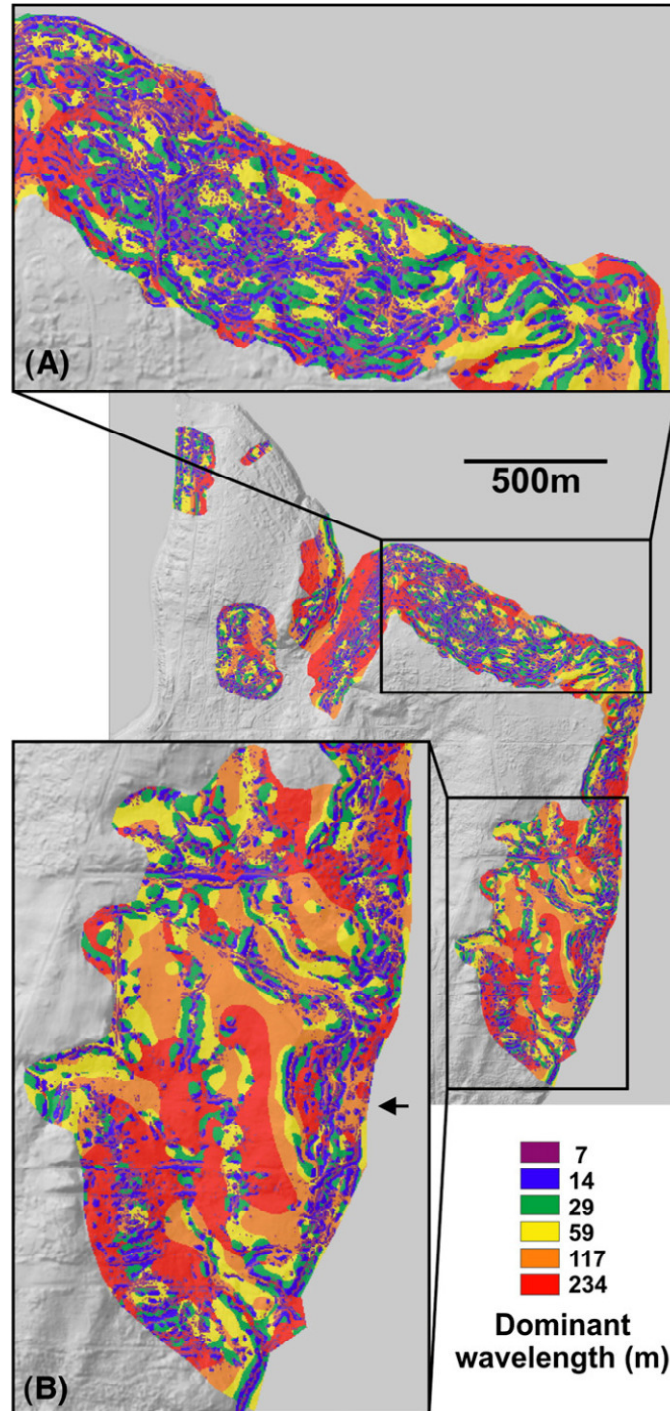


Fig. 12. Dominant wavelength map for deep-seated landslides in study area CBP. Warmer colors indicate longer dominant wavelengths. Recently active landslides (A) tend to have dominant wavelengths in agreement with the FWHM of the power spectra for the CBP study area (Fig. 7K). Ancient (M. Polenz, WA DNR, personal communication, 2008) landslides (B) have longer dominant wavelengths, marking a transition from deep-seated landslide processes to other geomorphic processes.

5. Discussion

A major strength of our automated deep-seated landslide mapping methods is that they work well in both rural and urban parts of our study areas. Although roads, grading, and other human modifications of the landscape do cause some misclassifications, many modifications do not completely erase the topographic signatures of deep-seated landslides. Anthropogenic topographic features often have higher spatial frequencies than deep-seated landslides in our study areas and therefore do not influence spectral power over our characteristic frequency bands. This filtering of unwanted wavelengths from the data works particularly well in Seattle, where nearly every node in the data has been modified by human activity, but our automated methods still classify 87% of the nodes correctly.

Error indices and percentages of correctly classified terrain both provide measures of how well our automatically generated maps match independently compiled, deep-seated landslide maps, but low error indices and high percentages of correctly mapped terrain do not always correlate. For example, we match the highest percentage of nodes, but also have the highest error index in MTC compared to our other study areas. In DMQ, we have the lowest error index, but also the lowest percentage of nodes classified correctly. These discrepancies result from differences in the abundances of deep-seated landslides in our study areas. To illustrate, we rewrite Eq. (6) as

$$E = 1 - \frac{C_{ls}}{A_{ls} + I_{ls}}, \quad (7)$$

where C_{ls} is the area of correctly identified landslide nodes (true positives), A_{ls} is the total area of mapped landslide nodes, and I_{ls} is the area of incorrectly classified landslide nodes (false negatives). In our data sets where A_{ls} is a high percentage of the total area

(DMQ and NWD), C_{I_s} can approach A_{I_s} while I_{I_s} remains low because very little land area exists to be classified as I_{I_s} . On the other hand, when A_{I_s} is only a small percentage of the total area (MTC, SEA, and CBP), I_{I_s} has the potential to become quite high as C_{I_s} approaches A_{I_s} simply because a large area of unfailed terrain exists. The former case tends to allow the ratio in Eq. (7) to approach 1, leading to a low E , while the latter case tends to keep the ratio small, leading to a high E . These discrepancies between error index and percentage of correctly classified nodes suggest that close visual inspection of maps may be required in addition to statistical measures to thoroughly evaluate the quality of the match between different landslide inventory maps of the same study area.

Our windowed 2D DFT and 2D CWT algorithms perform comparably to one another in each study area, but the 2D CWT shows more promise in future applications for several reasons. Most importantly, the 2D CWT applied to topographic data preserves information about position in addition to frequency, so it is more suited to visualization of spatial patterns of spectral power. Inspection of a study area's wavelet coefficients and dominant wavelength map allows both node-by-node analysis of specific morphologic features and investigation of broad spatial patterns. We chose the Mexican hat wavelet for our study because of its resemblance to a landslide hummock, but numerous other families of wavelets exist that may be better suited to different study areas or to extracting different topographic features. Lastly, the choice of wavelet scales is flexible in nonorthogonal wavelet analysis (Torrence and Compo, 1998), so as few or as many scales as needed can be analyzed, depending on the particular application. This differs from orthogonal wavelet analysis, which samples only discrete scale and location parameters (Torrence and Compo, 1998). For the automated mapping presented here,

after identifying characteristic wavelengths of deep-seated landslides, we needed only 5 to 7 wavelet scales to map topographic features associated with landslides. This required far less computation time than our windowed Fourier analysis.

Automated landslide mapping methods such as those described here may never completely replace traditional methods of topographic map inspection, aerial photograph interpretation, and fieldwork. In particular, because our automated methods rely entirely upon morphologic expressions as recorded by topographic data, they often do not capture the boundaries between neighboring and overlapping landslides and are insensitive to the details of subsurface geology. However, as high-resolution topographic data become increasingly available, our automated methods will provide effective, objective, and efficient tools that can supplement traditional methods. Our methods quantify and more objectively locate the same topographic features used to map landslides with visual inspection of photographs, maps, or high-resolution data, producing results that can serve as a starting point for a more detailed landslide inventory map in a fraction of the time required for a manual survey.

6. Conclusions

Landslide inventory maps provide valuable information to a variety of policy makers and scientists, but their creation remains a time consuming and subjective task. The increasing availability of high-resolution LiDAR-derived DEMs provides new opportunities for improving the efficiency and objectivity of mapping spatial and temporal patterns of slope instability. However, few studies to date have capitalized on

LiDAR-derived DEMs to investigate landsliding at meter-scale resolutions over kilometer-scale swaths of terrain.

We have described two signal processing techniques that can be used to quantify the morphologic expressions of deep-seated landslides using high-resolution topographic data and to map how these expressions vary spatially. Power spectra produced by two-dimensional Fourier and wavelet analyses define the characteristic wavelengths of landslide features in the Puget Sound lowlands, Washington, and the Tualatin Mountains, Oregon. Spectral power summed over a characteristic band of wavelengths provides a measure of the strength of the topographic signature of deep-seated landsliding at any point in a data set. Examining the spectral power sum at each node in mapview highlights patterns of past slope instability over study areas up to hundreds of square kilometers in extent.

To test how well these methods can delineate terrain that has undergone past deep-seated landsliding, we compared the outputs of our algorithms to independently created landslide inventory maps in each study area. We classified the algorithm-generated arrays so as to minimize the error index of the array compared to its corresponding landslide map. Assuming the landslide inventory maps recorded all landslides in each study area, our algorithms were able to match an average of 82% of the area in our five study areas. These results indicate that the 2D DFT and 2D CWT are capable of producing accurate deep-seated landslide maps in our study areas. Although we do not see automated methods replacing traditional landslide mapping methods, we propose that they can improve the objectivity of landslide mapping and decrease the time needed to compile landslide inventory maps.

Lastly, we created a dominant wavelength map to investigate the relationship between geomorphic processes and their topographic expressions. Spatial variations in dominant wavelength within deep-seated landslides highlight how deep-seated landsliding concentrates spectral power over intermediate wavelengths by dissecting the landscape into blocks and by forming hummocks of a particular spatial scale. Diffusive soil transport shifts spectral power to longer dominant wavelengths, while fluvial incision also dissects the surfaces of inactive deep-seated landslides at longer spatial scales. We suggest that dominant wavelength maps may be a useful tool for analyzing the topographic expressions of a suite of geomorphic processes over a wide range of scales.

CHAPTER III
A 1-D MECHANISTIC MODEL FOR THE EVOLUTION OF
EARTHFLOW-PRONE HILLSLOPES

Reproduced with permission from Booth, A. M., and J. J. Roering (2011), A 1-D mechanistic model for the evolution of earthflow-prone hillslopes, *J. Geophys. Res.*, 116, F04021, doi:10.1029/2011JF002024. Copyright 2011, the American Geophysical Union.

1. Introduction

In mountainous terrain, landslides often transport large volumes of material on hillslopes, exerting an important control on long-term erosion rate and therefore a landscape's topographic form. Especially where uplift rates are high, landslides may be the dominant mechanism of hillslope erosion [*Schmidt and Montgomery, 1995; Burbank et al., 1996; Korup et al., 2007*]. However, the high spatial and temporal variability of landslide motion and occurrence makes it challenging to infer long-term erosion rates due to landsliding using either short-term measurements or observations of landscape-scale topographic characteristics. Specifically, mapping active landslides and interpreting the morphology of inactive landslides can be a subjective and time consuming process [*Guzzetti et al., 2000; Wills and McCrink, 2002*], relationships between landslide frequency, area, and volume used to determine erosion rates often have high uncertainties [*Hovius et al., 1997; Stark and Hovius, 2001; Malamud et al., 2004; Brunetti et al., 2009; Guzzetti et al., 2009*], and few quantitative models exist for predicting landslide response to changes in climatic or tectonic forcing [*Densmore et al., 1998*]. Although several studies have utilized quantitative models of shallow landsliding to predict landscape response to changes in climate or uplift rate [*Tucker and Bras, 1998; van der Beek et al., 1999; Istanbuloglu and Bras, 2005*], comparable studies of deep-seated landslide

processes are lacking. In this study we characterize deep-seated landslides as those that incorporate some fresh or weathered bedrock and are more than several meters deep, in contrast to shallow landslides, which incorporate only soil and colluvium and are less than a few meters deep. Because of the above challenges, most studies addressing the role of deep-seated landslides in landscape evolution have focused on coarse topographic characteristics such as the distribution of hillslope angles at the mountain range scale [Schmidt and Montgomery, 1995; Burbank et al., 1996; Montgomery and Brandon, 2002; Gabet et al., 2004; Korup, 2008], despite the existence of many detailed, site-specific studies of individual landslides [e.g. Cruden and Krahn, 1973; Iverson and Major, 1987; Kilburn and Petley, 2003; Coe et al., 2003]. Few studies have addressed time and spatial scales intermediate to these two extremes in order to determine the role of deep-seated landslides in shaping hillslopes within a drainage basin [Miller, 1995; Roering et al., 2005].

Mathematical landscape evolution modeling is one method for exploring the interactions between deep-seated landslides and other surface processes at this intermediate scale. In a landscape evolution model (LEM), equations for sediment fluxes or incision rates due to different geomorphic processes govern the temporal evolution of the land surface elevation [Ahnert, 1976; Willgoose et al., 1991a, 1991b; Tucker and Bras, 1998]. Numerous studies have utilized geomorphic transport laws [Dietrich et al., 2003], which describe these fluxes in the context of landscape evolution, to infer geomorphic process rates based on landscape morphology or to simulate landscape response to changing process intensities [e.g. Kirkby, 1971; Tucker and Slingerland, 1994; Kooi and Beaumont, 1996; van der Beek et al., 1999; Roering et al., 2007; Perron

et al., 2009]. However, many of these models are limited to processes that can be easily approximated as varying slowly in both time and space. Few attempts have been made to generalize and include a geomorphic transport law for deep-seated landslide processes. *Ahnert* [1977, 1987] included a plastic flow term in numerical models to simulate slow mass movements if a threshold was exceeded, and *Kirkby* [1987] also developed a one-dimensional model for hillslope evolution including landsliding. Notably and more recently, *Densmore et al.* [1998] created a numerical landscape evolution model that produced realistic mountainous terrain and landslide frequency-magnitude statistics, while *Hergarten and Neugebauer* [1998, 1999] created a numerical model that exhibited self-organized criticality in landslide behavior. However, these studies' rule sets for deep-seated landslide initiation, movement, and deposition, although reasonable, are challenging to calibrate and not directly applicable to all types of deep-seated landslides, particularly the large, deep-seated earthflow failures that dominate many mountainous areas. For example, landslides in *Densmore et al.*'s [1998] model are rapid, with motion and deposition occurring in a single timestep, while in *Hergarten and Neugebauer*'s [1998, 1999] model, landslides controlled solely by the magnitude of a depth-slope product are the lone geomorphic agent acting at the surface. Here, we propose a rheology-based description of landslide initiation, movement, and deposition, and focus on the interactions among deep-seated landsliding, near-surface soil creep, and fluvial gully processes. We develop a landscape evolution model motivated by our observations of deep-seated earthflow behavior at a study site along the Eel River, northern California, but keep the model general to ensure it can be adapted to deep-seated landslides in diverse geologic settings.

Slope failures at the Eel River study site are slow, composite earth slide-earth flows [Cruden and Varnes, 1996], which we refer to simply as earthflows. At this site, earthflows transport weathered material, including blocks of weathered bedrock, downslope at rates of ~ 0.1 to 5 m yr^{-1} with shear strain, concentrated in bands ranging from narrow slip surfaces to meter-thick zones of distributed shear, responsible for most of the deformation. Movement is seasonal, with the onset of fast movement occurring once winter rainfall events elevate pore pressures sufficiently, as observed at a nearby earthflow [Iverson and Major, 1987]. In the study area, movements of active earthflows may temporarily become negligible during dry periods, while exceptionally wet periods may drive movement rates up to several meters per year [Mackey and Roering, 2011]. This style of slope failure commonly occurs in clay-rich, highly weathered lithologies such as the Franciscan mélangé of the California coast ranges [Kelsey, 1978; Keefer and Johnson, 1983; Iverson, 1986a; Mackey et al., 2009; and Mackey and Roering, 2011], which underlies the Eel River study site. Similar slope failures occur throughout the world in mechanically weak lithologies and have been extensively documented in the north island of New Zealand [Crozier, 1968; Gage and Black, 1979; McSaveny and Griffiths, 1987; Trotter, 1993], Japan [Matsukura and Mizuno, 1986], the Oregon Cascades [Swanson and Swanston, 1977; Pyles et al., 1987] and southern France [Malet et al., 2002; Maquaire et al., 2003].

In addition to earthflows, gullying and soil creep act to determine the morphology of hillslopes along the Eel River. Feedbacks between gullying and earthflow deformation may occur both on the lower sections of earthflows with deeply incised central or marginal gullies, and on higher sections containing extensive but often disconnected

networks of smaller gullies. For example, changes in the position and depth of the gully network affect the flow of groundwater within an earthflow, as discussed for earthflow microtopography by *Iverson and Major* [1987], which affects pore pressures within an earthflow. *Roering et al.* [2009] noted a correspondence between the fastest moving portion of an earthflow and a region with a high density of deep, connected gullies, and suggested that this network facilitated sediment removal from this part of the earthflow. Additionally, *Mackey and Roering* [2011] proposed that sediment transport in discontinuous gullies can redistribute mass near earthflow headscarps, which changes the state of stress in the underlying earthflow and alters movement. Surficial soil creep, driven by biologic or mechanical processes that dilate the soil, primarily smooths small-scale topographic roughness such as gully banks or hummocky topography associated with earthflow deformation.

These three processes - earthflows, soil creep, and gullying - act across an earthflow-prone landscape, driving changes in the land surface elevation over time. Our mechanistic mathematical model aims to capture the interactions among these processes over timescales that allow the full development of defining landscape characteristics such as hillslope length, profile form, and local relief. This necessitates averaging the behavior of each modeled process over many periods of activity and quiescence while retaining its essential components, as is common in many landscape evolution models [*Dietrich et al.*, 2003]. Because individual earthflows can remain active for hundreds to thousands of years [*Kelsey*, 1978; *Bovis and Jones*, 1992; *Mackey et al.*, 2009], we adopt a minimum timescale of 10^3 yrs as geomorphically significant for the purposes of this study.

We begin formulating a landscape evolution model for earthflow-prone terrain by combining expressions for sediment flux due to earthflows and soil creep with an expression for incision due to fluvial gully processes in a mass balance framework. In the model, earthflows behave as a non-Newtonian viscous fluid deforming under gravitational stress, soil creep is a slope-dependent diffusive process, and stream power determines the rate of fluvial incision via gullying. We then illustrate how changes in nondimensional parameters describing each process in the model control the form of a hillslope profile. To apply the model to our Eel River study site, as well as to a control site in the Gabilan Mesa, California, with no earthflow activity, we use Monte Carlo simulations to determine unique combinations of model parameters that best match representative profiles from the study areas. These model-generated profiles allow us to infer spatial patterns of erosion along a hillslope profile due to each modeled geomorphic process. Parameter values from the Monte Carlo simulations also yield estimates of the long-term average sediment flux due to each process, which we compare to observed process rates in the study areas. Lastly, using our most earthflow-prone study site as a reference state, we predict how changes in uplift rate and modeled earthflow parameters affect hillslope relief.

2. Study areas: Eel River and Gabilan Mesa, California

We develop our model for deep-seated earthflow-prone terrain based on observations of a study site along the Eel River, northern California (Figure 1). Bedrock there consists mainly of the central belt of the Franciscan Complex, part of a metamorphosed and tectonically-sheared Jurassic-Cretaceous accretionary prism [*Jayko*

+ (40° 9' N, 123° 37' W)

5km

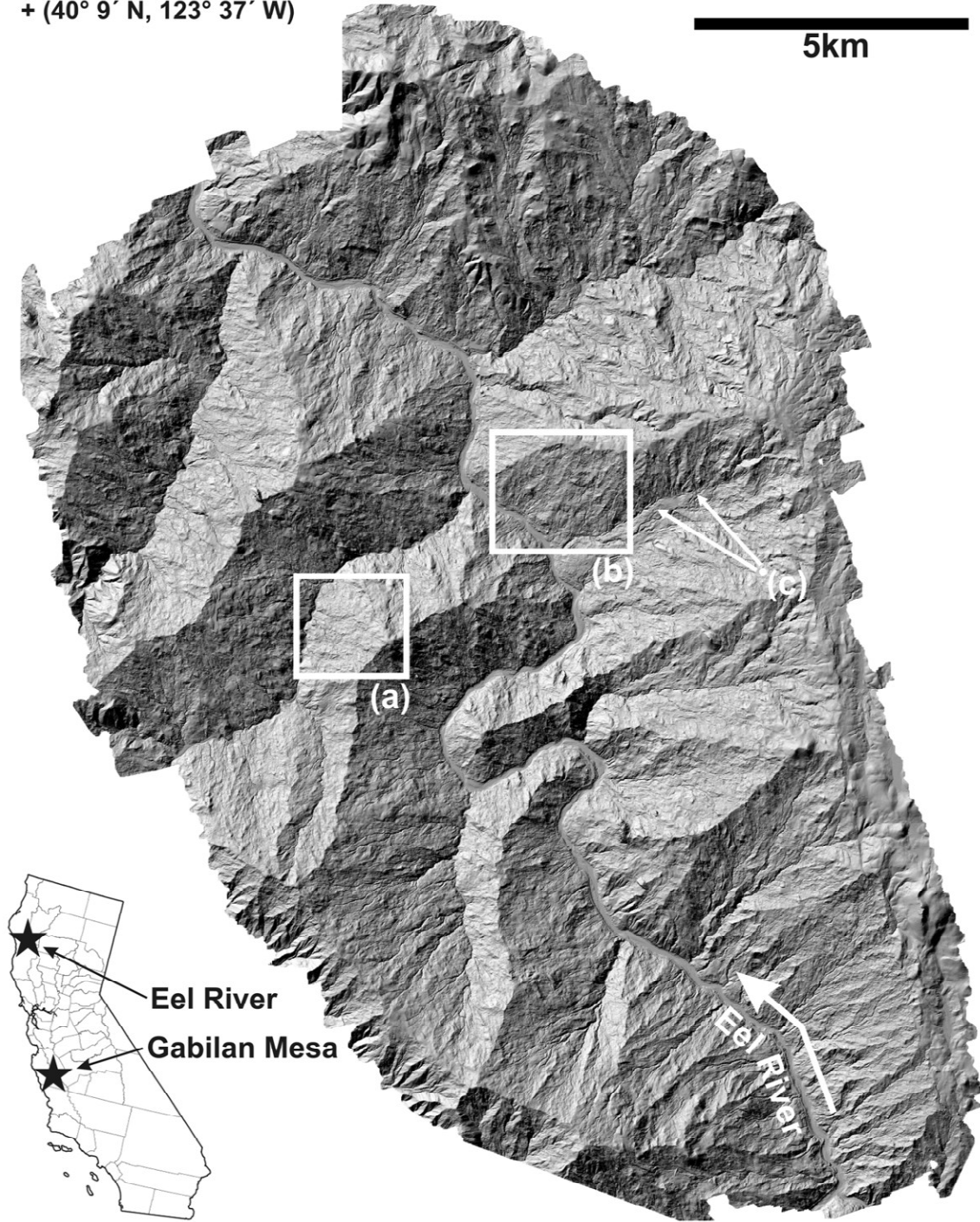


Figure 1. LiDAR-derived hillshade map of the Eel River study area. Hillslopes used to test our LEM, as described in section 4, (a) in a sandstone lithology and (b) in an argillaceous *mélange* lithology. (c) Approximate indication of the perspective view shown in Figures 2a and 2b.

et al., 1989; *McLaughlin et al.*, 2000]. A sheared *mélange* unit consisting mainly of meta-argillite underlies most of the terrain to the east of the Eel River in the study area and is especially prone to earthflows. Isolated blocks of chert, greenstone, and serpentinite occur within this unit, and these blocks commonly form local topographic highs less susceptible to earthflows than the surrounding hillslopes. To the west of the Eel River in the study area, the bedrock is mainly metasandstone and meta-argillite of the Broken Formation, which contains few highly sheared rocks. *McLaughlin et al.* [2000] note differences in the topographic expressions of these two units, with poorly incised and irregular topography in the *mélange*, and well-incised, regular drainages in the Broken Formation. Figure 2 illustrates the typical earthflow-prone topography of the *mélange* unit, where active and relict earthflow features such as headscarps, lateral levees, hummocks, and discontinuous gully networks cover nearly the entire hillslope. We select a representative hillslope from the Broken Formation (Figure 1, box (a)) to test our model in moderately earthflow-prone terrain, and from the *mélange* unit (Figure 1, box (b)) to test our model in pervasively earthflow-prone terrain. We carried out topographic analyses using a 1-m resolution LiDAR-derived digital elevation model (DEM) produced by the National Center for Airborne Laser Mapping (NCALM) in 2006.

The Eel River study area and surrounding mountains are currently experiencing rock uplift due to the northward migration of the Mendocino Triple Junction [*Furlong and Schwartz*, 2004]. Neither rock uplift nor erosion rate at the study site is known, but several studies have determined these rates in the vicinity. Rock uplift rates on the nearby coast range up to 4 mm yr⁻¹ as inferred from Holocene and late Pleistocene marine terraces [*Merritts and Vincent*, 1989]. *Fuller et al.* [2009] used ¹⁰Be concentrations in

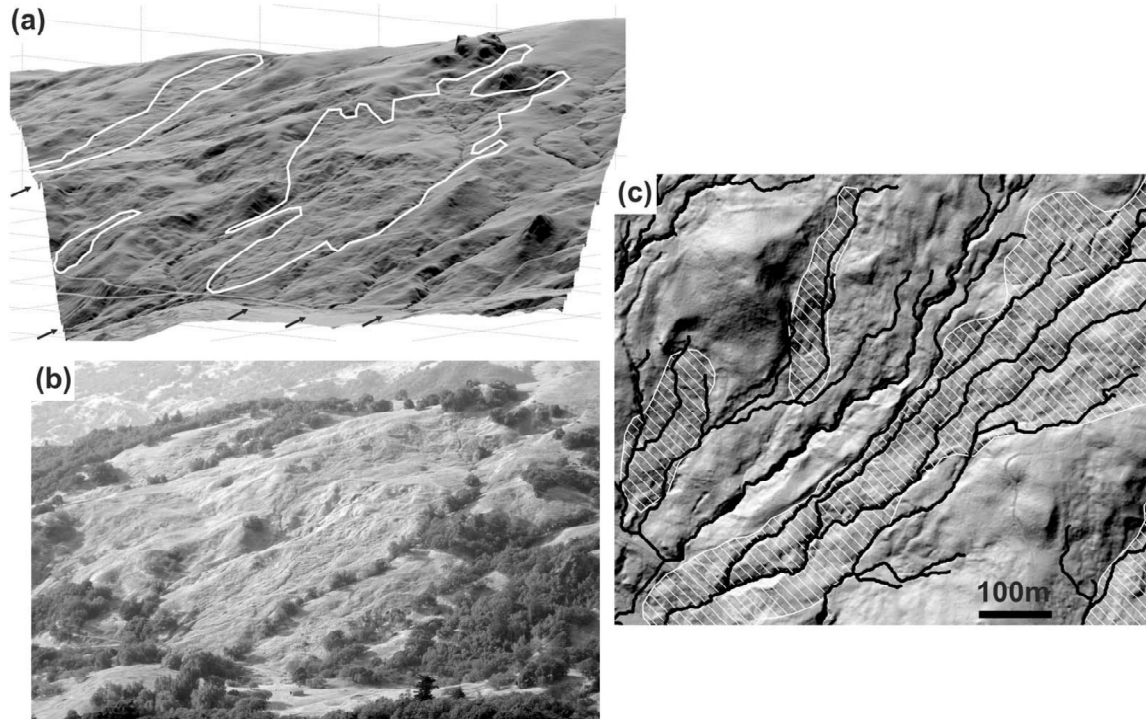


Figure 2. (a, b) Perspective view from Figure 1c, illustrating the typical geomorphology of earthflow-prone hillslopes in our Eel River study area. Figure 2a is a bare earth 1 m DEM draped with a hillshade map to approximate the same lighting and view angle as in Figure 2b, which is a photograph (barn in the central foreground for scale). In Figure 2a, the white outlines highlight three historically active earthflows [Mackey and Roering, 2011], and the black arrows indicate several of the more prominent and numerous small gullies incised on both active and relict earthflows. In addition to the active earthflows, relict headscarps, lateral levees, and hummocky topography cover most of the remaining hillslope, clearly indicating past generations of earthflow activity. Only a small portion of the hillslope, such as the smooth, rounded ridge at the upper right, lacks topographic signs of past earthflow failure. Figure 2c shows a more detailed view (center of Figure 5c) of a gully network incised into both active (white cross-hatched polygons) and relict earthflow features. Black lines show the steepest descent paths through this gully network.

strath terrace sediments and optically stimulated luminescence to estimate Pleistocene to Holocene erosion rates ranging from 0.07 to 0.35 mm yr⁻¹ in the nearby South Fork Eel River catchment. Finally, the modern, catchment-averaged erosion rate for the entire Eel River drainage basin, determined from 1950-2000 using suspended sediment data, is ~0.9 mm yr⁻¹ [Wheatcroft and Sommerfield, 2005]. Our site is probably not experiencing a

bedrock uplift rate as high as reported by *Merritts and Vincent* [1989] because their highest rates are confined to the tectonically distinct King Range [*Dumitru*, 1991], but it may be uplifting more rapidly than the South Fork [*Fuller et al.*, 2009] due to its present location just south and east of the Mendocino triple junction. *Furlong and Govers* [1999] predicted a peak in uplift to the south of the northward-migrating Mendocino Triple Junction using a geodynamic model, while *Lock et al.* [2006] estimated an uplift rate for this peak of 0.5 to 1 mm yr⁻¹ currently located near the northern end of the Eel River study site. We therefore adopt an uplift rate on the order of 1 mm yr⁻¹ in this study, which also agrees with the modern erosion rate averaged over the entire catchment. This choice of uplift rate does not affect our model formulation or application to the study sites, but does influence the magnitude of the sediment fluxes calculated in section 4.3.

To highlight differences between earthflow-prone terrain and other landscapes not influenced by landslides, we contrast the topographic characteristics of our Eel River study area with a site in the Gabilan Mesa, California (Figures 1 and 5a). This site shows no signs of earthflow or other landslide activity, and typifies gentle, convex ridge-valley topography common for first-order basins in soil-mantled terrain [*Montgomery and Dietrich*, 1992] resulting from a competition between near-surface soil creep and channelized fluvial processes [*Perron et al.*, 2008]. The Gabilan Mesa consists mainly of massively-bedded, continental gravel and sand of the Paso Robles Formation, which conformably overlie Pliocene shallow marine sediment [*Christensen*, 1965; *Galehouse*, 1967]. *Christensen* [1965] determined that the base of the Paso Robles formation in the vicinity of the study site has uplifted ~1000 ft over the last 2 or 3 million years, which gives an average rock uplift rate of 0.1 to 0.15 mm yr⁻¹ since the Pleistocene. Using

exposure and burial ages from cosmogenic radionuclides, *Perron et al.* [2005] determined a surface age of 86 to 464 kyr for unincised remnants of the original Gabilan Mesa surface ~80 m above the modern valley bottoms, which gives an incision rate of 0.14 to 0.74 mm yr⁻¹ over this time period [*Roering et al.*, 2007]. The strikingly uniform valley spacing [*Perron et al.*, 2008, 2009] and uniform ridgetop curvature [*Roering et al.*, 2007] suggest that the Gabilan Mesa is likely in a topographic steady-state such that erosion rate approximately balances rock uplift rate. We adopt an uplift rate of 0.3 mm yr⁻¹, near the center of the range reported above, and emphasize that this choice affects only the magnitude of the calculated sediment fluxes in section 4.3. We utilize a 1-m DEM of the Gabilan Mesa (Figure 5a), also produced by NCALM, for our analyses.

To systematically capture the morphologic characteristics of the Eel River landscape, we generate a slope-area plot using all LiDAR grid points in the study area except those in the main stem of the Eel River (Figure 3). At each grid point, the magnitude of the topographic gradient, calculated using its four nearest neighbors, determines the slope, and a steepest descent algorithm determines the drainage area. To determine the drainage area in streams whose headwaters are outside the study area, we supplement the 1-m DEM with a 1/3-arc second resolution DEM available from the United States Geologic Survey National Map Seamless Server (<http://seamless.usgs.gov/>). Figure 2 also shows a slope-area plot for the Gabilan Mesa, digitized from *Dietrich and Perron* [2006], who utilized a 2-m DEM, to highlight differences between the two sites.

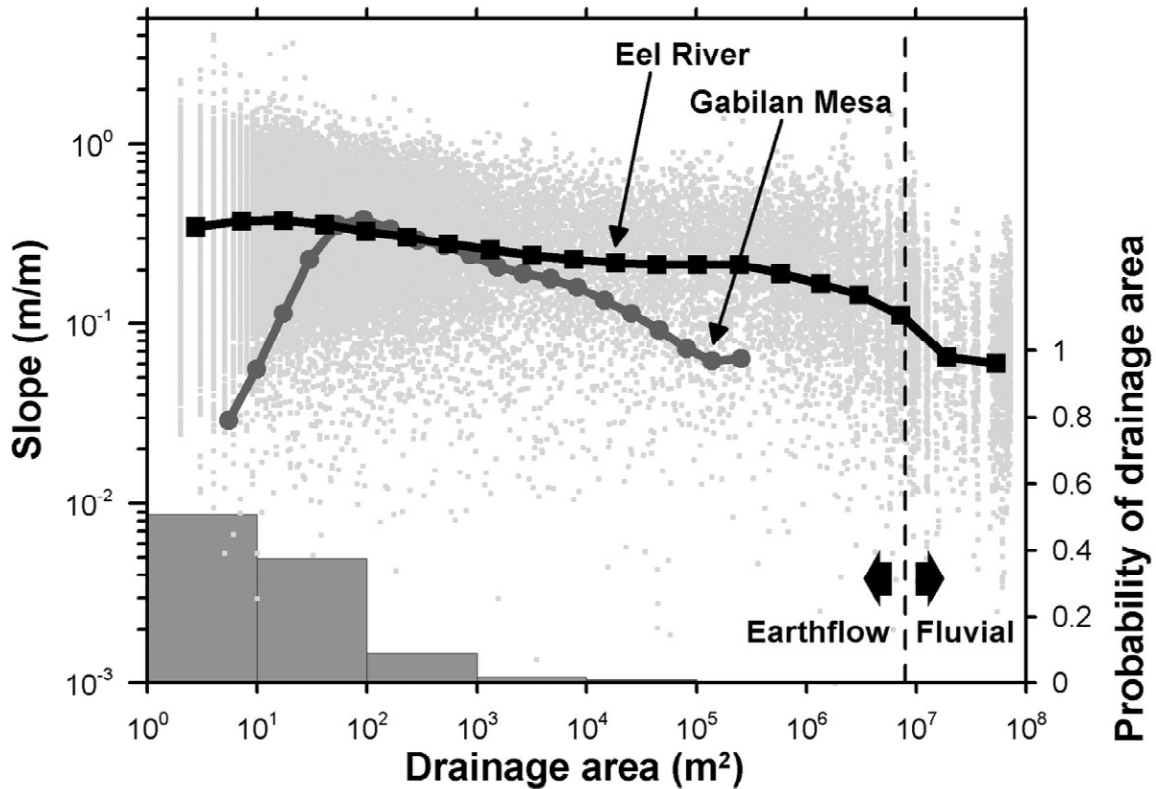


Figure 3. (left) Slope-area plots for the Eel River and Gabilan Mesa study sites, and (right) histogram of drainage area for the Eel River study site. On the left axis, the small grey points show the local topographic gradient and upslope drainage area at each grid point in the Eel River study area, the large black squares connected with a thick black line show the logarithmically binned mean, and the vertical dashed line approximately indicates the transition to a sediment transport regime dominated by fluvial processes. For comparison, the large grey circles connected with a thick line show a slope-area plot from the Gabilan Mesa, California, a site with no landslide activity, digitized from Dietrich and Perron [2006]. Standard errors are smaller than the symbols for both study sites. All $\sim 1.5 \times 10^8$ grid points with their complete drainage area contained within the DEM (Figure 1) were used to calculate the binned mean and standard error for the Eel River site, but for clarity, only a random subsample of points is shown. On the right axis, the grey bars indicate the proportion of all grid points in the DEM with drainage areas falling within each order of magnitude bin.

In the Eel River study area, topographic gradient tends to slowly decrease from ~ 0.35 to ~ 0.20 as drainage area increases up to $\sim 10^6 \text{ m}^2$. These locations occupy the >1 km long, low-angle hillslopes that make up over 99% of the terrain in the study area (Figure 3, right axis), nearly all of which show signs of previous or current earthflow and

gully activity (Figure 2). On this typical Eel River hillslope (Figure 2a,b), a patchwork of several historically active earthflows [Mackey and Roering, 2011] and hummocky topography, lateral levees, and headscarps from previous earthflow activity cover most of the slope. Several prominent gullies and networks of smaller, discontinuous gullies are incised over much of the hillslope. Figure 2c shows a more detailed view of a gully network incised into active and relict earthflow features. At areas greater than $\sim 10^6 \text{ m}^2$, the topographic gradient decreases slightly more rapidly up to a drainage area of $\sim 10^7 \text{ m}^2$, where it abruptly decreases to <0.1 (Figure 3). This transitional drainage area is typical of the main tributaries to the Eel River (Figure 1) and coincident with a transition to a sediment transport regime dominated by fluvial processes in the major rivers bounding the long, low-angle hillslopes.

The slope-area characteristics of the Eel River study site contrast sharply with those of the Gabilan Mesa. There, at small drainage areas less than 10^2 m^2 , topographic gradient increases rapidly with drainage area, tracking the transition from broad, gentle ridgetops to steeper hillslopes over a horizontal distance of tens of meters. Mean topographic gradients at the Eel River site, however, are much greater over this same range of drainage areas, and exhibit only a subtle increase followed by a subtle decrease in magnitude, due to the lack of well-developed ridge-valley topography at this short length scale. At drainage areas of $\sim 10^2 \text{ m}^2$, both sites have similar average topographic gradients, but topographic gradient decreases much more rapidly with increasing drainage area at the Gabilan Mesa site, to <0.1 at a drainage area of $\sim 10^5 \text{ m}^2$. Topographic gradients at the Eel River site do not attain a similar value for another two orders of magnitude in drainage area, or until $\sim 10^7 \text{ m}^2$. This difference reflects the two

sites' vastly different hillslope length scales: in the Gabilan Mesa, locations with drainage areas much larger than $\sim 10^2 \text{ m}^2$ are found only in the well-developed fluvial network, while locations with similar drainage areas in the Eel River study area are found within gullies that incise active or relict earthflows on this site's $>1 \text{ km}$ long hillslopes. Although differences in denudation rate and relief between the two sites could cause a significant difference in drainage density and therefore hillslope length scale [Kirkby, 1987; Howard, 1997; Oguchi, 1997; Tucker and Bras, 1998], we suggest that the greater than order of magnitude difference in hillslope length scales likely results from earthflows inhibiting the formation of small scale ridge-valley topography and effectively lengthening hillslopes.

3. Model formulation

The morphology of hillslopes in the Eel River study site (Figure 2), suggests that earthflows, gullies, and soil creep interact across the landscape to create the topographic signature revealed by the slope-area analysis described above. Our model therefore aims to capture the dynamics of interactions between these processes and to estimate their contributions to landscape form. To capture the first-order effects of earthflows on topographic form over geomorphically significant timescales, we combine a mechanistic mathematical expression for sediment flux due to earthflows with similar mechanistic expressions for soil creep flux and gully incision in a simple one-dimensional (1-D) landscape evolution model based on steady-state mass flux. The model simulates the evolution of the land surface elevation as a competition between these three processes, with each process affecting the entire modeled hillslope through time and driving the

hillslope profile toward a different end member steady-state solution. By allowing each of these processes to continuously shape the modeled hillslope, we emphasize process interactions, especially between earthflows and gullies, and determine the role each plays in shaping topography over $>10^3$ -year timescales. Our model is based on the Eel River study site, but we intentionally keep the model general so that it may be adaptable to other landscapes where landslide processes can be described as a flux of material with a characteristic velocity and depth. Below, we first develop each component of the model independently, then combine the components into a mass balance and derive a non-dimensional governing equation for generating steady-state solutions.

3.1. Soil creep

In soil-mantled landscapes, dilational disturbances of the near surface caused by biological and mechanical processes including vegetation growth, animal burrowing, and frost heave result in a net downslope flux of sediment [Selby, 1993]. Gilbert [1877, 1909] and Davis [1892] first proposed that this creep-driven flux should increase with topographic gradient, resulting in convex hillslopes. Culling [1960] later formalized this observation into a mathematical model by assuming that sediment flux is directly proportional to the topographic gradient, and studies have since provided field evidence for a model of this form using cosmogenic radionuclides [McKean *et al.*, 1993; Small *et al.*, 1999]. Following this body of work we describe the sediment flux per unit contour width due to soil creep, q_s (with units of $L^2 T^{-1}$), in one dimension as

$$q_s = -D \frac{\partial z}{\partial x}, \quad (1)$$

where D is a diffusive proportionality constant ($L^2 T^{-1}$), z is the land surface elevation (L) and x is horizontal distance from the drainage divide (L). For a hillslope in dynamic

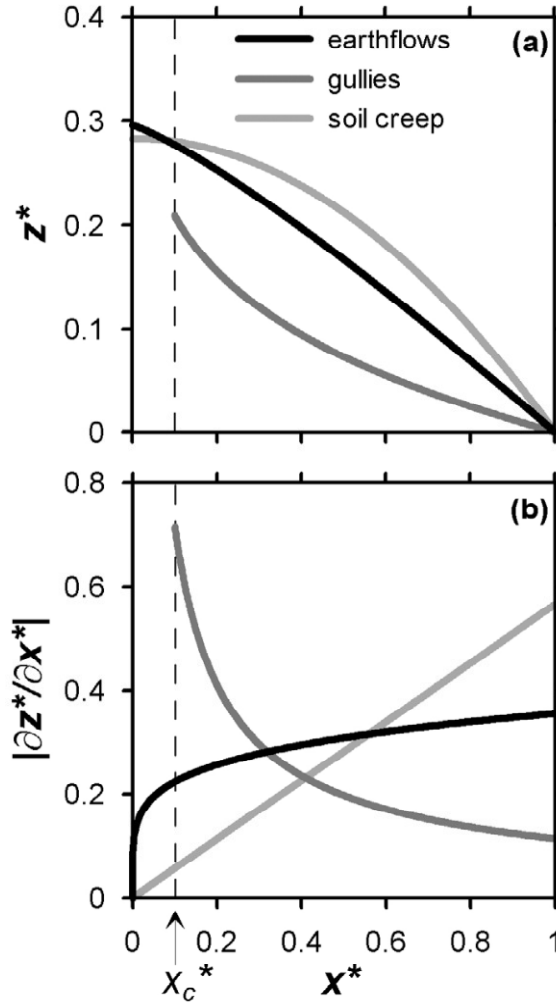


Figure 4. (a) Normalized elevation and (b) topographic gradient versus distance from the drainage divide for representative steady state model-generated profiles with only soil creep (lightest grey), gully incision (medium grey), or earthflow deformation (black) active. All distances are normalized to the hillslope length, and the exponents used to generate these curves are $hm = 0.8$, $n = 1$, and $p = 5$.

equilibrium with a uniform erosion rate, equation (1) predicts that the magnitude of the topographic gradient increases linearly with distance from the drainage divide, resulting in a convex parabolic hillslope form (Figure 4, light grey line) [Culling, 1960]. However, as hillslopes steepen, this linear approximation gives way to a nonlinear dependence of sediment flux on topographic gradient [Howard, 1994; Roering *et al.*, 1999], limiting the

applicability of equation (1) to gently sloping, soil-mantled terrain. Topographic gradients are 0.39 ± 0.22 and 0.36 ± 0.18 (mean \pm 1 standard deviation) in the Eel River and Gabilan Mesa study areas, respectively, for which there is little difference between the linear and non-linear models [Roering *et al.*, 1999].

3.2. Gully incision

Flow of water in a channel exerts a shear stress on its bed, resulting in the detachment and subsequent transport of sediment. The erosion rate of the bed therefore increases with shear stress, as expressed in the common stream power model for detachment-limited channels [Howard and Kerby, 1983]:

$$\dot{\epsilon}_g = KA^m S^n. \quad (2)$$

In equation (2), $\dot{\epsilon}_g$ is the incision rate ($L T^{-1}$), K is the coefficient of erosion ($L^{1-2m} T^{-1}$), A is drainage area (L^2), S is channel slope, and m and n are dimensionless constants. We favor this detachment-limited model over a transport-limited model because we frequently observe bedrock exposed in gullies in the study area, indicating that flows can remove most temporarily stored sediment from the channel, and that in the long term a gully's ability to be incised depends on the ability of flowing water to dislodge large boulders or detach fresh bedrock [Whipple and Tucker, 2002]. We do not observe debris flow deposits in these gullies, and therefore do not include a formulation of incision or deposition due to debris flows in our model. The drainage area, A , in equation (2) serves as a proxy for an effective water discharge, and the exponent m therefore reflects the hydraulic geometry of the channel, the drainage basin hydrology, and the dependence of incision on shear stress. The exponent n reflects only the dependence of incision on shear stress, and therefore may contain information about the physical mechanisms of erosion

responsible for lowering the bed [Whipple and Tucker, 1999]. To apply the stream power model to our 1-D model, we assume that drainage area increases with distance from the drainage divide according to Hack's law [Hack, 1957], such that

$$A = k_a x^h, \quad (3)$$

where k_a (L^{2-h}) and h are constants. Substituting equation (3) into equation (2) gives

$$\dot{\varepsilon}_g = K k_a^m x^{hm} \left| \frac{\partial z}{\partial x} \right|^n, \quad (4)$$

where the parallel bracket indicates absolute value, which describes the incision rate at each point along the modeled profile. For a channel experiencing steady state erosion, equation (4) predicts a concave profile with channel gradient decreasing smoothly in the downstream direction (Figure 4, medium grey line). To simulate a threshold drainage area for channel incision, we apply equation (4) only where $x > x_c$, where x_c is a critical distance from the ridgetop, determined by matching the model to observed profiles in section 4.1.

3.3. Earthflow flux and weathering

Earthflows transport sediment downslope through a combination of internal deformation and frictional slip on a shear surface [Brunsden, 1980; Keefer and Johnson, 1983; Zhang *et al.*, 1991; Swanson *et al.*, 1995]. In the former case, strain can be distributed throughout the earthflow mass, but is usually concentrated in a centimeter- to meter-thick zone near the base with plug-like flow near the surface [Keefer and Johnson, 1983; Iverson, 1986a; Pyles *et al.*, 1987] such that deformation of material within this shear zone controls the downslope flux. In the latter case, shear strain is localized on a single failure surface, so frictional properties of the failure surface control the flux of the

material above it. In particular, feedbacks between pore pressure and dilation across a failure surface may strongly control shear localization and earthflow motion over seasonal [Iverson and Major, 1987; Hilley *et al.*, 2004; Iverson, 2005] and even daily [Schulz *et al.*, 2009] timescales. However, it remains unclear how the displacement on and the location of a given failure surface evolve over longer than seasonal timescales. Borehole measurements and other observations of earthflow shear zones often reveal multiple failure surfaces at different depths [Brunsdon, 1984; Trotter, 1993], as well as distributed deformation across centimeter- to meter-thick zones at a given time [Keefer and Johnson, 1983; Iverson, 1986a; Pyles *et al.*, 1987]. Furthermore, models of earthflow movement based on Coulomb failure, including dilation and pore pressure interactions, focus on small displacements over short periods of time on a single slip surface [Iverson, 2005].

To extend these field observations and detailed models to longer timescales, we note that the deepest shear zones or failure surfaces are typically just above the interface between unweathered bedrock and weathered earthflow material [Swanson and Swanston, 1977; Trotter, 1993], indicating that in the long-term the position of this weathering front sets the depth of earthflow activity [Crozier, 1968; Gage and Black, 1979]. These observations suggest that in order for earthflows to persist in a landscape, the location of shear, either distributed or localized, tends to migrate downward in approximate concordance with the weathering front over geomorphically significant timescales. For the shear zone to migrate downward faster than the weathering front, it would have to deform stronger, unweathered bedrock, which is not consistent with our field observations. Conversely, if the weathering front migrated downward more rapidly

than the shear zone, the shear stress at the weathering front would increase, making deformation of this weathered material at depth more likely. Over time, these two opposing effects – higher material strength below the weathered zone and low driving stresses near the surface – would tend to focus the shear zone where driving stress is high and the material is weak, at the interface between fresh and weathered bedrock.

Here, we seek the first-order effects of earthflow motion on landscape evolution over these long timescales ($>10^3$ yrs) and so choose to approximate sediment flux by earthflow processes as a continuous non-Newtonian flow of all weathered material above the bedrock interface. In doing so, we assume that there is a characteristic earthflow thickness, set by the average depth of weathering, as described above, and that a steadily deforming, non-Newtonian flow effectively averages across periods of faster and slower earthflow motion. This treatment does not explicitly include the behavior of individual, short-lived failure surfaces or episodes of earthflow activity and quiescence, but instead parameterizes the long-term behavior of earthflows through the constants of the flow law.

The general relationship between stress and strain rate in a non-Newtonian fluid, assuming that variations in viscosity with strain rate are much greater than variations in normal stress differences [Barnes *et al.*, 1989], is

$$\dot{\epsilon}_{ij} = a |\sigma_{II}|^{p-1} \sigma_{ij}, \quad (5)$$

where $\dot{\epsilon}_{ij}$ is a component of the strain rate tensor (T^{-1}), a is a constant ($L^p M^{-p} T^{2p-1}$), σ_{II} is the second invariant of the stress tensor ($M L^{-1} T^{-2}$), p is a dimensionless flow law exponent, and σ_{ij} is the corresponding component of the stress tensor ($M L^{-1} T^{-2}$). For an earthflow modeled as a 1-D, uniform, gravity driven non-Newtonian flow, shear in the

downslope direction is the only significant component of the stress tensor, so the shear strain rate is

$$\frac{\partial u'}{\partial z'} = a(\rho_e g (H' - z') \sin \theta)^p, \quad (6)$$

where the prime notation refers to a coordinate system aligned with the slope such that u' is the slope-parallel velocity ($L T^{-1}$), z' is the slope-normal coordinate (L) with $z' = 0$ at the base of the earthflow, ρ_e is the density of weathered earthflow material ($M L^{-3}$), g is acceleration due to gravity [$L T^{-2}$], H' is slope-normal earthflow thickness (L), and θ is the slope angle. For $p \geq 1$, this rheology can represent a range of behaviors from a Newtonian viscous fluid ($p = 1$) to a completely plastic material ($p \rightarrow \infty$). The value of p therefore controls the thickness of the shear zone relative to the depth of the flow, with moderate values of ~ 5 – 10 giving a narrow shear zone in general agreement with the observations described above. *Iverson* [1986a, 1986b, 1986c] used a similar rheology-based approach to investigate the response of an earthflow to perturbations to its stress field, while *Vulliet and Hutter* [1988a, 1988b, 1988c] and *Vulliet* [2000] have accurately predicted the deformation of slow-moving landslides using a similar rheology in a finite element model. We extend this rheology-based modeling approach to investigate landscape evolution by generalizing equation (6) to a form that can be easily combined with equations (1) and (4) in a mass balance framework.

Integrating equation (6) twice with respect to z' and making use of the small angle approximation [*Turcotte and Schubert*, 2002, p. 311] gives an expression for the depth-averaged flux per unit contour width due to earthflow movement, q_e ($L^2 T^{-1}$), as

$$q_e = \frac{a(\rho_e g |\partial z / \partial x|)^p H^{p+2}}{p + 2}, \quad (7)$$

where H is the vertical earthflow thickness [L]. We use the magnitude of the surface slope so that for any $p \geq 1$, equation (7) always gives a real value for the flux in the positive direction when $x \geq 0$. Assuming uniform, steady-state uplift at a rate U ($L T^{-1}$) and erosion of material with density ρ_e along the entire length of a profile, equation (7) predicts that the topographic gradient varies as

$$\left| \frac{\partial z}{\partial x} \right| = \frac{|x|^{1/p}}{\rho_e g H^{1+2/p}} \left(\frac{U(p+2)}{a} \right)^{1/p}, \quad (8)$$

which gives a topographic profile that transitions from convex to near planar with distance from the drainage divide when $p > 1$ (Figure 4, black line). By applying this expression for earthflow flux to geomorphically significant timescales in our 1-D model, we assume that there is a characteristic earthflow thickness, H , and material parameters, a and p , that adequately describe the long-term behavior of earthflows in the study area. Equation (7) has the form of a geomorphic transport law [Dietrich *et al.*, 2003] where the flux of material depends on some material parameters and the local topography, and so easily incorporates into a landscape evolution model.

3.4. Governing equation and nondimensionalization

Conservation of mass in one dimension requires that along a hillslope profile affected by the three geomorphic processes described above, the land surface elevation changes with time as

$$\frac{\partial z}{\partial t} = \frac{\rho_r}{\rho_e} U - \frac{\partial}{\partial x} (q_s + q_e) - \dot{\epsilon}_g, \quad (9)$$

where t is time (T), ρ_r is the bulk density of intact bedrock ($M L^{-3}$), and U is uplift rate relative to a baselevel ($L T^{-1}$). In further developing our landscape evolution model we note that soil creep and earthflow processes are active over the entire length of hillslopes

in the Eel River study area, while gullies do not form until after accumulating a small threshold drainage area. We therefore allow q_s and q_e to be non-zero everywhere along the modeled hillslope profile, but allow \square_g to be non-zero only beyond a critical distance, x_c (L), from the ridgetop to simulate a threshold for channel incision. Changes in the land surface elevation at a point on the profile result from competition between all three modeled processes for $x \geq x_c$, and a competition between just soil creep and earthflows for $0 \leq x < x_c$. *Smith and Bretherton [1972]*, *Howard [1994]*, *Tucker and Bras [1998]*, and *Perron et al. [2008]*, for example, previously used similar process competition-based models where both hillslope and channel processes act at every point in the landscape. We do not include a threshold for earthflow deformation because nearly all points in the Eel River study area show signs of past earthflow activity, and earthflows therefore appear to be continuously active enough over the long term, relative to soil creep and gully processes, to maintain their expression in the topography. Substituting equations (1), (4), and (7) into (9) and simplifying gives

$$\frac{\partial z}{\partial t} = \frac{\rho_r}{\rho_e} U + D \frac{\partial^2 z}{\partial x^2} - \frac{a(\rho_e g)^p H^{p+2}}{p+2} \frac{\partial}{\partial x} \left(\left| \frac{\partial z}{\partial x} \right|^p \right) - K k_a^m x^{hm} \left| \frac{\partial z}{\partial x} \right|^n, \quad (10)$$

which describes the rate of change of the land surface elevation at each point along a one-dimensional hillslope profile for $x \geq x_c$. For $0 \leq x < x_c$, we simply set the last term on the right-hand side of equation (10) equal to 0. Each term on the right-hand side represents a contribution to the change in the land surface elevation due to a specific modeled geomorphic process. The first term describes vertical motion of bedrock and its change in density due to weathering, which supplies mobile, weathered material that can be transported by geomorphic processes. The second term describes surficial soil creep as a

diffusive process, where elevation is the quantity being diffused, which primarily smooths the topography in areas of high profile curvature. The third term represents earthflow deformation, which transports weathered material of thickness H downslope according to the non-Newtonian flow rheology described in section 3.3. The last term describes detachment-limited incision due to flow of water in gullies.

To better understand how the terms in equation (10) control the form of a modeled hillslope profile, we recast it in terms of dimensionless variables. This facilitates comparison of the relative importance of each of the terms, and simplifies analysis of the modeled hillslope response to changes in forcing parameters. We first use hillslope profile length, ℓ , as a characteristic length scale, and the ratio of hillslope length to uplift rate, ℓ/U , or the time it takes to uplift one hillslope length in the vertical direction, as a characteristic timescale to substitute the following into equation (10):

$$z^* = z/\ell, \quad x^* = x/\ell, \quad H^* = H/\ell, \quad \text{and} \quad t^* = tU/\ell. \quad (11)$$

Four nondimensional groups result,

$$\rho^* = \frac{\rho_r}{\rho_e}, \quad (12a)$$

$$D^* = \frac{D}{U\ell}, \quad (12b)$$

$$V^* = \frac{a(\rho_w g)^p H^{p+2}}{U\ell(p+2)}, \quad (12c)$$

$$\text{and } K^* = \frac{Kk_a^m \ell^{hm}}{U}, \quad (12d)$$

which characterize the relative magnitude of each modeled geomorphic process. The first is the density ratio of fresh bedrock to weathered earthflow material. The second is the ratio of the characteristic uplift timescale, ℓ/U , to the characteristic timescale for

diffusion of a feature of size ℓ . The third is the ratio of the uplift timescale to a characteristic timescale for a non-Newtonian flow, which is the time required for a flow with thickness H and a surface slope of 1 to transport ℓ^2 of sediment past a reference point. The last is the ratio of the uplift timescale to the timescale for a kinematic wave, such as a knickpoint, to propagate a distance ℓ in the upstream direction. The magnitudes of D^* , V^* , or K^* quantify the intensity of the three main processes transporting sediment in the study area – soil creep, earthflows, and gullies, respectively – with higher values indicating more vigorous geomorphic activity with respect to uplift. The relative magnitudes of D^* , V^* , and K^* reflect the relative intensities among each of the modeled geomorphic processes.

The nondimensional version of the governing equation for our LEM is then

$$\frac{\partial z^*}{\partial t^*} = \rho^* + D^* \frac{\partial^2 z^*}{\partial x^{*2}} - V^* \frac{\partial^*}{\partial x^*} \left(\left| \frac{\partial z^*}{\partial x^*} \right|^p \right) - K^* x^{*hm} \left| \frac{\partial z^*}{\partial x^*} \right|^n, \quad (13)$$

where each nondimensional parameter given in equations (12a-d) controls the relative contribution of each term on the right-hand side to changes in the land surface elevation. In taking this approach, we capture the general, first-order behavior of the modeled processes in a way that is consistent with basic dimensional analysis and can be easily applied to the study area. Specifically, we assume that a change in any of the dimensionless parameters D^* , V^* , and K^* , adequately encompasses a change in any of the dimensional parameters in a way that captures the dynamic behavior of the modeled system. For example, a change in any of the parameters on the right-hand side of equation (12c), such as earthflow thickness or density, affects V^* , but the magnitude of V^* alone should capture the essential characteristics of the modeled topographic profile.

3.5. Steady-state solutions

For steady-state denudation, each geomorphic process included in our model (equation (13)) drives the modeled hillslope profile toward a distinct topographic form. As a result, different topographic forms reflect the relative importance of the various geomorphic processes within the context of the model. Figure 4 gives examples of modeled steady-state topographic profiles with soil creep, earthflows, or gully incision acting independently. If only soil creep transports sediment ($V^*, K^* = 0$), the magnitude of the topographic gradient increases linearly with distance from the drainage divide, and elevation decreases as x^{*2} . If earthflows are the only mechanism for transporting sediment ($D^*, K^* = 0$), topographic gradient first increases rapidly with distance from the divide, then increases gradually, leading to an elevation profile that transitions from convex to quasi-planar. If gully incision is the only geomorphic process acting along the profile ($D^*, V^* = 0$), both topographic gradient and elevation decrease from a maximum value at the channel head (where $x^* = x_c^*$) rapidly at first, then more gradually, generating a broad concave morphology.

If all three of these geomorphic processes act in competition along the modeled hillslope, profiles reflect a blend of the three end members described above, which the values of D^* , V^* , and K^* describe quantitatively. Equation (13) can thus be a tool for predicting steady-state topographic form given estimates of these controlling parameters. Conversely, a given steady-state profile resulting from a unique combination of model parameters, as we will show in section 4.1, can provide a means for estimating values of these parameters at a particular site. Below, we exploit this quantitative relationship

between topographic form and geomorphic process to infer values for D^* , V^* , and K^* and estimate sediment fluxes due to different geomorphic processes at the study sites.

4. Results

To demonstrate the utility of our model for making quantitative predictions about the behavior of earthflow-prone terrain, we apply it to our Gabilan Mesa and Eel River study sites. The Gabilan Mesa site (Figure 5a), which shows no signs of earthflow activity, serves as a control to demonstrate that, given a topographic profile, the model does not falsely predict any sediment flux due to earthflow activity where there is none. The first Eel River site (Figure 5b) is underlain by the Broken Formation metasandstones and shows some minor historic earthflow activity, while the second (Figure 5c) is underlain by the weaker *mélange* lithology and shows major historic earthflow activity [Mackey and Roering, 2011]. We first demonstrate that the model can generate steady-state topographic profiles in good agreement with representative profiles observed in each of these distinctive sites using reasonable values for the free parameters. Next, we highlight along-profile patterns of steady-state erosion due to each of the modeled geomorphic processes and discuss implications for the study areas. We then calculate long-term average sediment fluxes due to each of the modeled geomorphic processes along the representative profiles, which are in agreement with modern rates observed in the study areas. Last, we illustrate how changes in modeled earthflow behavior affect predicted hillslope relief under varying rates of tectonic forcing.

4.1. Matching observed profiles

As a first test of our LEM, we utilize Monte Carlo simulations to determine combinations of the parameters D^* , V^* , K^* , x_c^* , and hm/n that generate steady-state solutions to equation (13) that best match representative topographic profiles at the three sites with varying levels of historic earthflow activity. We determine representative profiles at these sites by extracting 9–37 profiles from the 1 m resolution LiDAR DEMs, normalizing the profiles by their length, and then averaging the elevations at 100 evenly spaced, interpolated points along each profile. Figure 5 shows the locations of the profiles, and Figure 6 shows the resulting representative profiles from each site. At the Gabilan Mesa site our profiles capture the first-order hillslope-valley transition so that both soil creep acting on the convex ridges and fluvial incision acting in the channels shape the representative profile. At the Eel River sites, we select straight profiles that extend nearly the full length of the long, quasi-planar hillslopes in order to include the competing effects of earthflows, gullies, and soil creep. This method of selecting profiles captures the general topographic form of the hillslope, which records the integrated effects of geomorphic processes acting over time, rather than that of a specific earthflow or gully, and aligns with the goals of our steady-state, process competition model.

In our Monte Carlo simulations, we numerically solve equation (13) for steady-state topographic gradient as a function of normalized distance from the drainage divide for random combinations of the parameters D^* , V^* , K^* , x_c^* , and hm/n over the ranges given in Table 1. To solve equation (13) at steady-state, we set $\partial z^*/\partial t^* = 0$ and solve for $\partial S^*/\partial x^*$, where $S^* = |\partial z^*/\partial x^*|$, then integrate this differential equation from the drainage divide, where $S^* = 0$, to the foot of the hillslope at $x^* = 1$ using a stiff ordinary

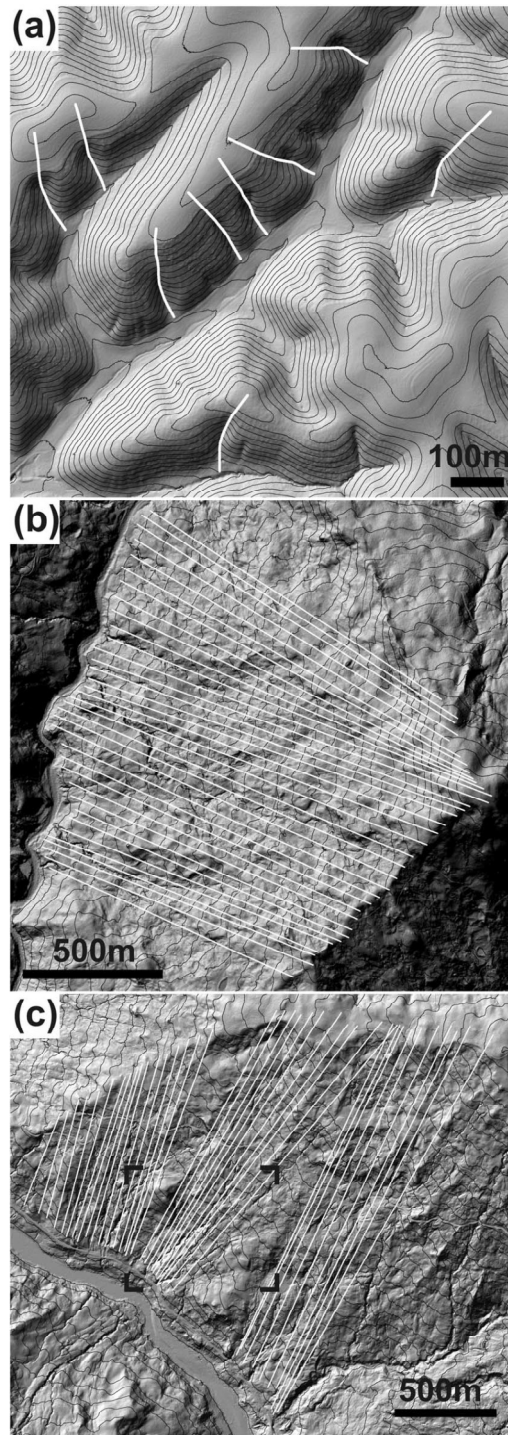


Figure 5. LiDAR-derived hillshade maps of sites used to compare steady state model solutions to representative topographic profiles from (a) the Gabilan Mesa site, (b) the Eel River sandstone site, and (c) the Eel River mélangé site. The white lines indicate locations of individual profiles averaged to determine the representative profile at each site. The contour interval is 5 m in Figure 5a, and 20 m in Figures 5b and 5c. A detailed view of the area in rectangular brackets in Figure 5c is shown in Figure 2c.

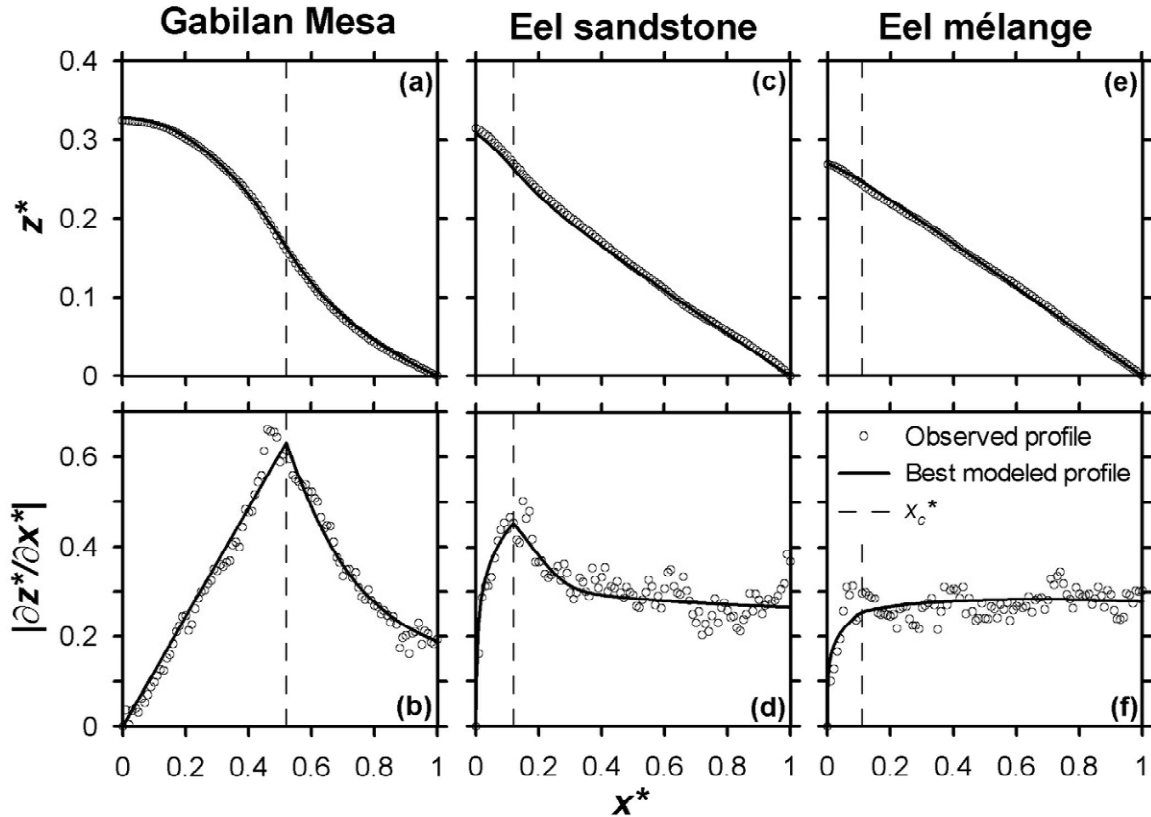


Figure 6. Representative and best fit hillslope profiles from (a, b) the Gabilan Mesa, (c, d) the Eel River sandstone, and (e, f) the Eel River mélange sites. Minimum misfits given in Table 1 are determined from the normalized topographic gradients at each site (Figures 5b, 5d, and 5f).

differential equation solver in Matlab (The Mathworks, Inc.) [Shampine and Reichelt, 1997]. This allows all uplifted material to be transported across the hillslope boundary at $x^*=1$ at steady-state, simulating the efficient removal of sediment by the actively incising rivers that bound our representative hillslopes. For each combination, we calculate the misfit (RMS error) between the modeled and normalized observed profiles, and determine the combination of model parameters that minimizes the misfit. Based on initial simulations over a wider range of parameters, we selected the parameter ranges reported in Table 1 so that they include the combination that minimizes this misfit and illustrate the dependence of misfit on each parameter in the vicinity of the best fit value.

Initial simulations also indicated that the minimum misfit is not sensitive to ρ^* or p , as long as $p > 3$, at any of the three sites, so we set these parameters to reasonable values of $\rho^* = 1.6$ and $p = 5$. This estimate for ρ^* is based on typical rock to soil density ratios [Selby, 1993], while the estimate for p gives a reasonable plug-flow rheology and is in agreement with the range of values reported in Vulliet and Hutter [1988a, 1988b] and Vulliet [2000]. No modeled profiles match the observed profiles well when $p < 3$. The misfit at the Gabilan Mesa site is not very sensitive to hm/n , so we set this ratio to 0.63 ($h = 1.8$, $m = 0.35$ and $n = 1$), as in Perron et al. [2009] and making use of Hack's Law (equation (3)) [Hack, 1957], at that site only. The remaining parameters D^* , V^* , K^* , and x_c^* are chosen at random from the ranges given in Table 1 in each simulation at each site, and their values exert a strong control on the quality of the fit.

Table 1. Parameter values that generate the best fit between modeled and observed hillslope profiles for the Gabilan Mesa and Eel River study sites, and the ranges of parameters sampled.^a

Free Parameter	Best-fit values			Range		
	Gab.	San.	Mel.	Gab.	San.	Mel.
D^*	1.3	4.2×10^{-2}	7.7×10^{-3}	$1 \times 10^{-1} - 1 \times 10^1$	$1 \times 10^{-3} - 1 \times 10^0$	$1 \times 10^{-3} - 1 \times 10^1$
V^*	4.3×10^{-2}	9.0	1.7×10^2	$1 \times 10^{-6} - 1 \times 10^2$	$1 \times 10^{-1} - 1 \times 10^3$	$1 \times 10^1 - 1 \times 10^4$
K^*	10.3	26.9	5.7	$1 \times 10^0 - 1 \times 10^2$	$1 \times 10^{-1} - 1 \times 10^2$	$1 \times 10^{-1} - 1 \times 10^3$
x_c	0.52	0.12	0.11	0.4–0.6	0.01–0.3	0.01–0.3
hm/n	0.63 ^b	0.10	0.21	0.63 ^b	0.1–2.0	0.1–2.0
RMS Error	2.7×10^{-3}	3.5×10^{-3}	3.0×10^{-3}			

^aGab. = Gabilan Mesa (Figure 5a), San. = Eel River sandstone lithology (Figure 5b), and Mel. = Eel River mélange lithology (Figure 5c).

^bDenotes values that were held constant in determining the best-fit profile at that site.

As a control, we first apply the landscape evolution model to the representative profile from the Gabilan Mesa site. In this landscape, soil creep and fluvial incision are the most important geomorphic processes, and there is no evidence of landslide activity. The representative profile (Figure 6a,b) reflects this since slope increases linearly with distance from the divide over the upper half of the profile as predicted for soil creep, and then decreases smoothly over the lower half of the profile as predicted by the stream power model. Our best-fit modeled profile matches the observed profile well and is especially sensitive to D^* and K^* , as shown by the sharp minima in Figure 7a,c. As expected for a site with no earthflow activity, results are not sensitive to V^* , as long as it is less than ~ 0.1 , as shown by the broad, flat minimum in Figure 7b.

We next apply our model to the Eel River site underlain by the sandstone lithology where there are only a few small ($< 0.025 \text{ km}^2$), isolated patches of historic earthflow activity [Mackey and Roering, 2010]. The fluvial network at this site is much less organized than at the Gabilan Mesa site, but the gullies are more established than at the m \acute{e} lange site, as evidenced by the subtly concave profile over the lower $\sim 90\%$ of the hillslope (Figure 6c,d). Our best-fit modeled profile matches this observed profile, and is most sensitive to V^* and K^* (Figure 7f,g). The misfit is relatively insensitive to D^* (Figure 7e) as long as it is less than ~ 0.1 , indicating that soil creep is not important in setting the long-term profile form at this location compared to earthflow and gully processes. Small values of hm/n also tend to result in a better fit (Figure 7i), indicating that gully incision at this site does not depend strongly on drainage area, but instead depends strongly on local topographic gradient (equation (2)).

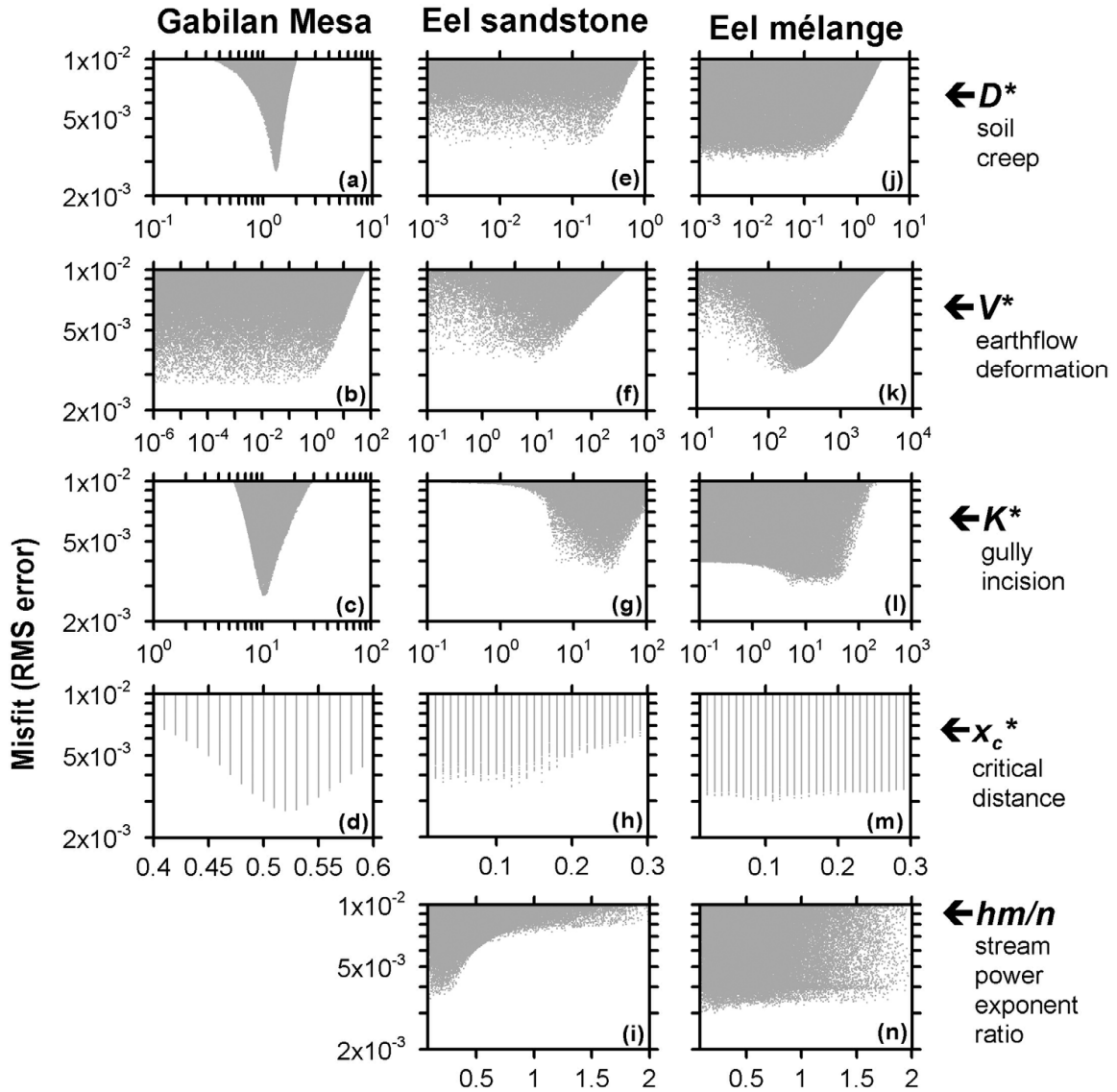


Figure 7. Misfit versus the landscape evolution model’s free parameters at each of the study sites. Each point represents a steady state solution to equation (11) generated with a random combination of parameters from the ranges given in Table 1. The minimum of each point cloud defines the best model-generated profile.

Finally, we apply our model to the Eel River site underlain by Franciscan *mélange* where several large (up to $\sim 0.5 \text{ km}^2$) earthflows are active and nearly 10% of the surrounding landscape area contains historically active earthflows [Mackey and Roering, 2011]. Here, the gully network consists of many small, often disconnected segments, and the average profile is slightly convex (Figure 6e,f), both of which suggest the importance

of earthflow processes. Our best-fit modeled profile also matches the observed profile well at this site. The misfit is most sensitive to V^* , and a narrow range of values for K^* fit the data approximately equally well (Figure 7k,l). Similar to the Eel River sandstone profiles, the misfit is not sensitive to D^* as long as it is less than ~ 0.1 (Figure 7j). Small values of hm/n also tend to result in a better fit (Figure 7n), but the minimum is not as well defined as at the sandstone site, perhaps because the earthflow term exerts a much stronger control on profile form at this site.

4.2. Spatial erosion patterns

To highlight spatial variations in the modeled geomorphic processes, we substitute these best-fit parameter values (Table 1) back into equation (13) and calculate the contribution of each transport process to the dimensionless rate of change of the land surface elevation, $\partial z^*/\partial t^*$, at each point along the profile (Figure 8). A negative contribution to $\partial z^*/\partial t^*$ at a given point indicates that the particular process lowers the land surface elevation (erosion), while a positive contribution indicates that the process raises the land surface elevation (deposition). Because we solve for steady-state topographic profiles, the contributions of the soil creep, earthflow, and gully terms must sum to equal the long-term erosion rate, $-\rho^*$, at every point along the profile. The values of D^* , V^* , and K^* set the profile-averaged magnitude of each geomorphic process, but local topographic gradient, curvature, and distance from the drainage divide modulate the intensity and sign of each process along the profile.

For the Gabilan Mesa profile (Figure 8a), only soil creep and fluvial incision contribute to the steady state topographic form. When $x^* < x_c^*$, only soil creep transports sediment, so the steady-state profile attains a convex form allowing soil creep alone to

lower the land surface elevation at the long-term uplift rate. When $x^* \geq x_c^*$, fluvial incision also plays a role in balancing uplift, and contributes to lowering the land surface elevation. Because this segment of the profile is concave, the soil creep term is positive and contributes to raising the land surface elevation, so the stream power term must lower the land surface elevation more rapidly than the long-term uplift rate to keep pace. This effect is especially apparent when x^* is just greater than x_c^* , where the profile has the highest concavity as well as a high topographic gradient. The sharp step in process rates at x_c^* results from the model's assumption that the drainage area threshold for channel incision is fixed at x_c^* over time. In the field, the position of the channel head likely fluctuates over time [Dietrich and Dunne, 1993], which would smooth this process transition when temporally averaged. Earthflows are not present at this site and do not significantly affect the modeled steady-state profile form.

At the sandstone site in the Eel River study area (Figure 8b), earthflow deformation and gully incision exert the strongest controls on topographic form. Soil creep plays a minor role in smoothing the drainage divide and nearly keeps pace with the uplift rate there, but contributes negligibly to changing the land surface elevation on the remainder of the quasi-planar hillslope. Instead, when $x^* < x_c^*$, the earthflow term becomes increasingly important in lowering the land surface elevation with increasing x^* , and approximately keeps pace with uplift near x_c^* . However, at x_c^* the profile abruptly becomes concave and has a high topographic gradient until $x^* \sim 0.3$. Over this range of x^* , the gully term lowers the land surface elevation more quickly than the long-term uplift rate due to the high, but decreasing, topographic gradient, and the earthflow term contributes to raising the land surface elevation due to the high profile concavity. The

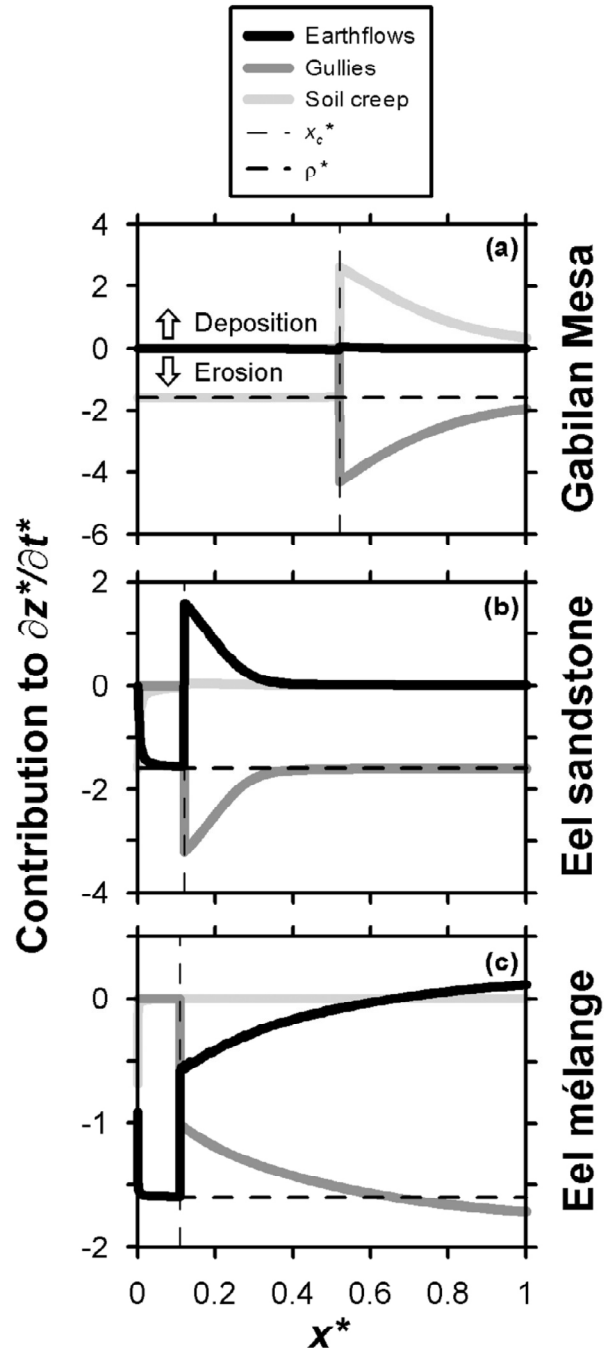


Figure 8. Contributions of each modeled geomorphic process to $\partial z^*/\partial t^*$ at each point along the best fit profiles from the three study sites. The light grey line shows the contribution from the soil creep term, the medium grey shows the gully incision term, and the black shows the earthflow term. At every point along the profile these three terms sum to the long-term nondimensional erosion rate, $-\rho^*$, shown as the horizontal dashed line.

remaining section of the profile becomes approximately planar, and the gully term alone nearly keeps pace with uplift, reflecting the low hm (drainage area exponent) to n (slope exponent) ratio of the best-fit model result. Despite its sensitivity to topographic gradient, the earthflow term does not contribute to changing the land surface elevation over this section of the profile because the gradient is remarkably uniform, resulting in a steady flux of earthflow material downslope.

At the *mélange* site in the Eel River study area (Figure 8c), earthflows and gullies again strongly control the topographic form, with soil creep playing only a minor role in lowering the drainage divide. As at the sandstone site, the earthflow term is effective at lowering the land surface elevation when $x^* < x_c^*$ and keeps pace with uplift near x_c^* . However, when $x^* > x_c^*$, the modeled profile is still convex at this site, so the earthflow term continues to contribute to lowering the land surface elevation, although at a much slower rate. The gully incision term contributes to lowering the land surface elevation over this section of the profile as well, but its magnitude does not exceed the long-term uplift rate as it did at the other two sites. As $x^* \rightarrow 1$, the profile becomes nearly planar, and the gully term alone is able to keep pace with uplift while the earthflow term transports a steady flux of sediment.

Although along-profile variations in the sign and magnitude of the modeled geomorphic processes are different between the two Eel River sites, they both fit well with observed characteristics of earthflows. Earthflows typically have an upper source area that feeds sediment into a long, narrow transport zone, which ends in a bulbous toe at the foot of a hillslope [Kelsey, 1978; Keefer and Johnson, 1983; Cruden and Varnes, 1996; Baum *et al.*, 2003]. Earthflow source areas in the study area often occur just below

drainage divides, and our model predicts that earthflows at both the sandstone and mélangé sites substantially lower the land surface elevation near the drainage divide over the long term. Transport zones in the study area extend most of the length of hillslopes and tend to transport a roughly steady flux of sediment by plug flow [Mackey *et al.*, 2009]. Our model captures this behavior well at the middle and lower sections of the profiles where the earthflow term contributes negligibly to changing the land surface elevation, relative to the gully term. However, at the sandstone site, the model predicts a small region where earthflows substantially contribute to raising the land surface elevation just after x_c^* instead of transitioning smoothly into the transport zone regime. As modeled, this indicates a small zone at the lower edge of the earthflow source area where earthflows are inefficient at transporting sediment due to the rapidly decreasing topographic gradient. This effect is not present in the modeled mélangé profile because it is convex near x_c^* , suggesting that the more vigorous earthflow activity at this site can efficiently transport material from source to transport zones. Some bulbous earthflow toes are present in the study area where an earthflow transports sediment onto a flat part of terrain, but rivers flowing along the base of hillslopes often truncate earthflows before they form distinct depositional toes. Our model simulates hillslope processes and does not include river bank processes, so the profiles end just before reaching a hillslope-bounding river, and the model results are therefore relevant to the truncated earthflow transport zones common in the study area.

4.3. Long-term process rates

Our LEM results also provide estimates of the long-term average sediment flux along each study site's representative profile due to the modeled geomorphic processes.

To determine average fluxes, we numerically integrate the curves in Figure 8, multiply by an estimated uplift rate, U , and the mean profile length, ℓ , divide by the density ratio, ρ^* , and then average over the length of the profile. At the Gabilan Mesa site, we estimate a modest uplift rate of 0.3 mm yr^{-1} and at the Eel River site assume a faster rate of 1 mm yr^{-1} (section 2). Since the magnitude of the sediment flux due to each modeled process scales linearly with U , different estimates of U give different total fluxes, but each process contributes the same proportion to the total flux. The uncertainty in the magnitude of the estimated fluxes is also directly proportional to the uncertainty in U . Mean profile lengths are 171 m, 1287 m, and 1329 m at the Gabilan Mesa, Eel River sandstone, and Eel River mélange sites, respectively.

Table 2 lists the average sediment fluxes per unit contour width due to each process at each site predicted by the landscape evolution model. The magnitude of any one of these fluxes is only as precise as the uplift rate, but we report all the fluxes as though uplift rate is known precisely in order to highlight the proportional contributions of each process to the sediment flux at each site. In the Gabilan Mesa, sediment flux along the representative profile is approximately balanced between soil creep and fluvial incision, with soil creep on average transporting 54% of the sediment and fluvial processes transporting 46%. We emphasize that this result is particular to our chosen first-order valley profiles, and that the balance of sediment fluxes would tip much more in favor of soil creep on hillslope-only profiles, or toward fluvial processes on profiles including more of the fluvial network. In the Eel River sandstone lithology, gully processes become very important in transporting sediment along the profile and, on average, account for ~94% of the sediment flux. In terms of volume of sediment

transported, earthflows are of minor importance at this site, transporting just 4% of the sediment, while soil creep transports the remaining 2%. However, smaller values of D^* also allow the model to match the observed profile well at this site, so this 2% soil creep contribution is a maximum value. Although earthflow motion does not deliver much sediment to the channel network at this site, it is important on the upper hillslope in allowing the model to match the observed profile. In the Eel River mélange lithology, gullies also transport the majority of the sediment (69%), but earthflows contribute a substantial 31% to the average sediment flux. This finding is similar to that of *Kelsey* [1978] in the nearby Van Duzen River basin, where earthflow motion and gully erosion from earthflows each supply about 50% of the sediment to rivers truncating earthflow toes, although on average the earthflows in that study move more rapidly and are deeper than those in our Eel River site.

Table 2. Long-term average sediment fluxes per unit contour width due to each geomorphic process at each site predicted by the best-fit modeled profiles.^a

Mean sediment flux	Site			
	Gab.	San.	Mel.	
Soil creep, q_s	1.4×10^{-2} (54%)	9.8×10^{-3} (2%)	1.4×10^{-3} (0%)	$\text{m}^2 \text{ yr}^{-1}$
Earthflow, q_e	2.1×10^{-5} (0%)	2.8×10^{-2} (4%)	2.1×10^{-1} (31%)	$\text{m}^2 \text{ yr}^{-1}$
Gully, q_g	1.2×10^{-2} (46%)	6.1×10^{-1} (94%)	4.6×10^{-1} (69%)	$\text{m}^2 \text{ yr}^{-1}$

^aGab. = Gabilan Mesa (Figure 5a), San. = Eel River sandstone lithology (Figure 5b), and Mel. = Eel River mélange lithology (Figure 5c).

The absolute magnitude of our modeled earthflow flux, $q_e = 2.1 \times 10^{-1} \text{ m}^2 \text{ yr}^{-1}$, is consistent with observations that earthflows in the Eel River mélangé lithology are typically several meters deep, move $\sim 1 \text{ m yr}^{-1}$, and historically occur in $\sim 10\%$ of the terrain at a given time [Mackey and Roering, 2011]. However, because this estimate depends on the uplift rate, which we do not know precisely at this site, we consider it an order of magnitude estimation. That this flux is of the same order as the modern flux suggests that earthflows have been active at similar rates over the $>10^3$ yr timescales encapsulated by the averaged topographic profiles used in this study.

4.4. Model-predicted steady-state hillslope relief

To place the predictions of our model in a wider spatial and temporal context, we calculate curves of steady-state, dimensionless hillslope relief – maximum hillslope elevation divided by length, or the average topographic gradient – over a range of rock uplift rates while varying two key parameters that describe earthflow behavior, V^* and p (Figure 9). Although the value of p does not exert a strong control on our best-fit profiles, it does dramatically influence the model's theoretical predictions of how steady-state relief scales with uplift rate. Changing V^* relative to D^* and K^* affects the overall magnitude of earthflow processes and, according to equation (12c), accommodates changes in earthflow characteristic depth, H , bulk density, ρ_e , or the constant in the non-Newtonian flow law, a . Changes in the magnitude of V^* may therefore reflect changes in climate since the presence of more or less water within an earthflow likely affects all three of these parameters. The highly nonlinear influence of H on V^* implies that changes in earthflow thickness most strongly affect the magnitude of V^* , so deeper weathering, perhaps due to variable precipitation or lowering of the water table, may be

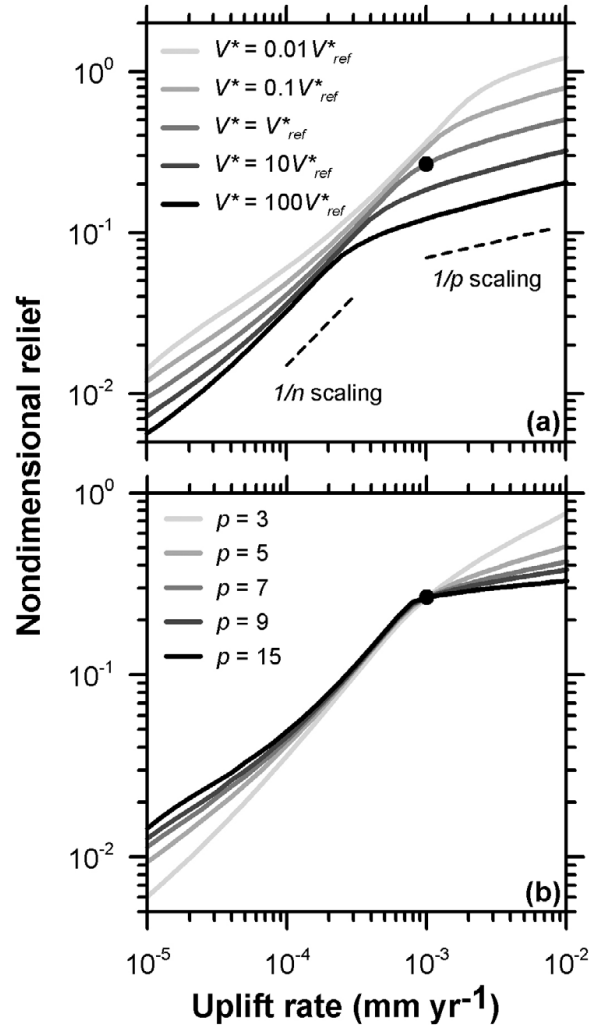


Figure 9. Model-predicted hillslope relief (normalized by hillslope length) as a function of uplift rate for varying magnitudes of (a) V^* with $p = 5$ and (b) p . The reference profile, indicated by the black dot, is the best fit modeled profile at the Eel mélangé site with $U = 1 \text{ mm yr}^{-1}$.

the most effective way to increase the overall magnitude of earthflow activity. Changing p affects the nonlinearity of the flow law (equation (6)) and therefore whether earthflows behave more viscously or plastically in the long term.

To generate earthflow-driven, steady-state relief vs. erosion rate curves (Figure 9), we first take the best-fit profile from the Eel River mélangé site as a reference state with an uplift rate of 1 mm yr^{-1} and a dimensionless hillslope relief of 0.27. We then

simulate changes in uplift rate by proportionately changing the magnitudes of D^* , V^* , and K^* , which results in a relief-uplift rate curve for the Eel River mélange reference state. Next, we vary V^* by 4 orders of magnitude above and below the reference state, and similarly simulate changes in uplift rate using these increased or decreased values of V^* . This results in a suite of relief-uplift rate curves for different values of V^* (Figure 9a). We also calculate how varying the landslide rheology parameter, p , influences the relationship between relief and uplift rate. Again using the Eel River mélange profile, we first vary p above and below the reference value and determine the best-fit V^* while leaving all other parameters constant. This produces several nearly indistinguishable best-fit modeled profiles with an average gradient and relief similar to the observed profile (Figure 6e,f). We then generate an additional suite of relief-uplift rate curves by proportionally varying D^* , V^* , and K^* .

Figures 9a and b illustrate two distinct regimes over which dimensionless relief increases with uplift rate. At low uplift rates, relief increases relatively rapidly with uplift rate, and modeled profiles in this regime are highly concave, indicating that the stream power term most influences topographic form. This concavity is possible because the stream power term depends on x^* in addition to the local topographic derivative and is therefore able to incise even as topographic gradients become low. Relief increases approximately as $1/n$ in this regime, as predicted by equation (13) with D^* , $V^* = 0$. However, at extremely low uplift rates the relief scaling deviates slightly from this trend because the stream power term reduces the topographic gradient to near zero over most of the lower profile, where $x^* \geq x_c^*$. For uplift rates similar to that of the reference state, relief begins to increase less rapidly as the modeled profiles transition into a more

earthflow-dominated regime. The magnitudes of V^* and p affect the details of this high uplift rate regime by altering modeled earthflow behavior. Increases in V^* alone (Figure 9a), with $p = 5$ as in the Eel River mélangé reference state, cause a decrease in hillslope relief across the full range of simulated uplift rates, and also shift the transition to the earthflow-dominated regime to lower uplift rates. In other words, as earthflows become more effective at transporting sediment, they require smaller topographic gradients to keep pace with uplift and exert a dominant control on topographic form at relatively modest uplift rates. Increases in p cause hillslope relief to increase less rapidly with uplift rate in the earthflow-dominated regime, and relief approaches a threshold value as $p \rightarrow \infty$ and the rheology becomes completely plastic. Relief increases approximately as $1/p$ in this regime as predicted by equation (13) when $D^*, K^* = 0$. The tendency for relief to become insensitive to uplift rate as p increases is consistent with the idea of threshold hillslopes resulting from finite rock mass strength [Carson and Petley, 1970; Schmidt and Montgomery, 1995; Burbank et al., 1996]. However, our landscape evolution model predicts that if landslides have a viscous component to their deformation and behave more as a plug-type flow, hillslope relief, or average topographic gradient, may continue to be an indicator of uplift rate even with strong tectonic forcing.

5. Discussion

In this contribution, we propose a mechanistic geomorphic transport law for deep-seated earthflows that is consistent with observed topographic profiles and geomorphic process rates in the study areas. By focusing on average hillslope profiles, with lengths of hundreds of meters to kilometers, and geomorphically significant timescales of $>10^3$

years, our results offer several advantages over both long-term, range-scale studies and short-term, site-specific earthflow studies. For example, our slope-area analysis (Figure 2) demonstrates that topographic gradient in earthflow-prone terrain tends to slowly decrease over a wide range of drainage areas up to $\sim 10^6 \text{ m}^2$, suggesting that a threshold slope approximation, as is commonly employed in range-scale landscape evolution models [Howard, 1994; Tucker and Slingerland, 1994; Tucker and Bras, 1998; van der Beek *et al.*, 1999], would not adequately capture the topographic trends in the study area. Furthermore, applying a threshold slope model to the study area would not capture the subtle differences in profile curvature (Figure 6) that strongly control both spatial patterns (Figure 8) and average rates (Table 2) of earthflow sediment transport in our model. On the other hand, at shorter spatial and temporal scales over which earthflow motion is typically monitored, sediment transport is highly variable and measured rates from an individual earthflow may not be representative of longer-term average rates. By using topographic form to infer relative process rates, our model averages over this short-term variability and yields relative rates specifically relevant to the observed topography. We emphasize that our estimate of V^* also represents a landscape-scale, long-term average, although site-specific studies and laboratory experiments may constrain reasonable values for the dimensional parameters contained in V^* , such as a and p in the non-Newtonian flow law.

Our Monte Carlo simulations show that the magnitudes of D^* , V^* , and K^* dictate the morphology of hillslopes at the study sites, but the behavior of the model with respect to hm/n and p reveals details about the mechanisms of each modeled geomorphic process. At both Eel River study sites, lower values of hm/n result in better matches between

modeled and observed profiles, indicating that gully incision depends only weakly on distance from the drainage divide. This could result from low values of h or m , or a high value of n . We determined that $h = 1.25 \pm 0.01$ (95% confidence) by plotting drainage area vs. downstream distance for 8 major gullies spanning the Eel River mélange hillslope. This value is significantly less than both $h = 2$, which would indicate self-similar scaling, and *Hack's* [1957] value of $h = 1.67$, indicating that drainage area increases less rapidly with downstream distance than in many other settings. In the stream power model, m depends on the exponents describing the dependence of incision rate on shear stress, the dependence of channel width on discharge, and the dependence of discharge on drainage area [Whipple and Tucker, 1999]. Our small best-fit values of hm/n could therefore also result from a weak dependence of incision rate on shear stress, a strong dependence of channel width on discharge, or a weak dependence of discharge on drainage area. Of these options, we expect the first to be unlikely since our model predicts high values of n at the Eel River sandstone site, and n reflects only the dependence of incision rate on shear stress [Whipple and Tucker, 1999]. Instead, we find it more likely that channel width depends strongly on discharge, perhaps due to a more rapid increase in channel width with downstream distance compared to alluvial channels, as found by *Snyder et al.* [2000] for small catchments near the study area. Also, it may be that discharge increases slowly with drainage area at the study sites, possibly due to ecological factors such as spatial variations in evapotranspiration.

Interestingly, the insensitivity of our model results to p , so long as it yields a plug-like flow, implies that the specific style of earthflow deformation or sliding is less important than the overall magnitude of the depth-averaged earthflow flux in generating

the observed profiles in the study area. Within the model, this insensitivity may arise from the dependence of V^* on p (equation (12c)), which allows many combinations of these two parameters to match the observed profiles equally well. Also, as p increases, the rheology of the modeled earthflows rapidly becomes more plastic so that further increases in p do not substantially change the shape of the resulting steady-state profile. Our method for choosing representative profiles may also contribute to this insensitivity by averaging over much of the spatial and temporal variability in earthflow behavior present at each site. For example, the Eel River mélange site (Figure 5c) contains several active earthflows with different sizes, possibly different failure mechanisms, and different movement rates, but our model seeks only to capture the first-order, long-term form of the landscape by matching an averaged, representative profile. Although this technique does not reveal much information about p at the study sites, it does imply that earthflows transport material in a plug-flow fashion, and it may provide information about other earthflow properties relevant to long-term landscape evolution such as the characteristic depth, H , flow law constant, a , or earthflow bulk density, ρ_e , according to equation (12c) and given independent estimates of some of these parameters.

Despite this insensitivity to p , and therefore to the specifics of earthflow failure mechanisms, we emphasize the importance of explicitly connecting geomorphic transport laws to relevant geomorphic processes. Other mathematical expressions can produce low-gradient, near-planar hillslopes with convex ridgetops similar to those produced by our equation (7) for earthflow flux, but do not lead to insights into earthflow behavior. For example, an equation in which sediment flux increases nonlinearly with topographic gradient and approaches infinity at some critical slope value produces a similar hillslope

form [Howard, 1994; Roering *et al.*, 1999], but is rooted in force and energy considerations of surface particles being disturbed by various biological and physical processes [Roering *et al.*, 1999]. More recently, models of Tucker and Bradley [2010] and Fofoula-Georgiou *et al.* [2010] produce relatively planar hillslopes by emphasizing non-local transport, in which a surface disturbance can move individual sediment grains distances comparable to the hillslope length scale. We could potentially compare our earthflow profiles with any of these models, but such an endeavor would not reveal much about the behavior of slow-moving earthflows with a depth-dependent sediment flux.

Our model formulation allows some speculation about the effects of changes in climatic forcing on long-term landscape evolution in earthflow-prone terrain. Changes in precipitation affect the parameters describing soil creep (equation (1)) [Fernandes and Dietrich, 1997; Tucker and Bras, 1998; Perron *et al.*, 2009] and stream power (equation (2)) [Tucker and Slingerland, 1997; Whipple, 2001] through changes in vegetation, for example. However, within the framework of our model, changes in precipitation probably most strongly affect the magnitude of the earthflow flux (equation (7)) due to its highly nonlinear dependence on earthflow thickness, H . As described in section 3.3, the position of the weathering front sets the depth of mobile earthflow material. In fine-grained, argillaceous mudstones, such as the Franciscan *mélange* underlying much of the study area, cycles of wetting and drying often drive weathering [Ollier, 1969; Franklin and Chandra, 1972; Matsukura and Mizuno, 1986; Stephenson and Kirk, 2000] so that the position of the weathering front should approximately track the position of the groundwater table, as observed by Rempe *et al.* [2010] in a similar lithology to that of the study area. In this way, we suggest that the long-term depth of earthflow activity should

be inversely related to the amount of precipitation. Sustained wetter climatic periods would ultimately result in thinner earthflows, so the terrain in our model would steepen, causing the depth-averaged velocity of earthflows to increase in order to accommodate a given sediment flux. Conversely, drier climatic periods would lead to thicker earthflows, so gentler slopes in the model would allow slower earthflow failures to accommodate a given flux of sediment. Changes in the frequency and magnitude of earthflow occurrence could also result from changes in average earthflow depth, but our model does not make any quantitative predictions about these changes because it does not explicitly include stochastic earthflow behavior. This relationship between earthflow depth and climate may in part explain observations of more earthflows on dry, south-facing slopes in and near the study area [*Kelsey, 1978; Mackey and Roering, 2011*]. In other words, the limited depth of weathering may inhibit earthflow activity on the wetter north-facing slopes.

Finally, we suggest that our method for including deep-seated earthflows in a model using an expression for a depth-dependent sediment flux may be adaptable to other types of slope failures. In landscapes with more competent bedrock than in the study site, the typical spacing of weak sedimentary layers or joints, for example, could set the failure depth, which would vary spatially and temporally as other geomorphic and tectonic processes modify the landscape. Incorporating this depth information into an expression for landslide velocity would then determine the flux due to the modeled landslide process. We choose a non-Newtonian flow law to determine the landslide flux in the study area because it captures the general behavior of earthflows, but different rheologies or frictional properties of a failure surface, for example, could determine rates of

landslide motion in other landscapes. We emphasize that including such simplified treatments of landslide behavior in landscape evolution models can lead to new insights into spatial and temporal patterns of erosion and feedbacks between geomorphic processes.

6. Conclusions

This study presented a mathematical model that captured the general characteristics of a deep-seated earthflow-prone landscape along the Eel River, northern California. By combining expressions for sediment fluxes or incision rates due to soil creep, earthflow, and fluvial processes, we first derived an equation to describe the change in the land surface elevation with time along a hillslope profile. Steady-state profiles modeled using this equation matched representative profiles from sites with varying levels of historic earthflow activity. The magnitude of a nondimensional number describing the intensity of earthflow processes based on a non-Newtonian flow rheology tracked the level of historic earthflow activity well. Using best-fit modeled profiles, we then determined the contribution of each modeled geomorphic process to changing the land surface elevation at each point along the profile. Modeled earthflows contributed substantially to lowering the land surface elevation on the upper hillslopes and transported an approximately steady flux of sediment on mid to lower hillslopes, consistent with observations of earthflow collection zones and transport zones, respectively, in the Eel River study area. The best-fit profiles also provided estimates for the long-term average sediment flux due to each modeled geomorphic process, with modeled earthflows contributing the highest flux at the site with the most historic

earthflow activity. The magnitude of this flux, on the order of $10^{-1} \text{ m}^2 \text{ yr}^{-1}$, is consistent with modern earthflow movement rates at that site, but modeled gullies incising the earthflow surface transported the majority of sediment along the profile. We also generated theoretical curves of steady-state hillslope relief vs. uplift rate, which indicated that relief increases nonlinearly with uplift rate in earthflow-prone landscapes. These results indicated that topographic metrics such as mean hillslope angle, if known precisely, may record uplift rate in earthflow-prone landscapes even at high uplift rates where threshold slope processes normally limit further topographic development.

We demonstrated that incorporating a geomorphic transport law for deep-seated earthflow processes into a landscape evolution model can yield valuable information about spatial and temporal patterns of sediment transport. In doing so, we addressed a gap in landscape evolution modeling between long-term ($>10^6$ yr), range-scale studies and short-term ($<10^2$ yr), hillslope-scale studies. Future landscape evolution modeling studies potentially have much to gain by focusing on interactions among simple expressions for various geomorphic processes, especially deep-seated landsliding.

CHAPTER IV
TOPOGRAPHIC SIGNATURES OF SLOW-MOVING, DEEP-SEATED
LANDSLIDES AND A GENERAL LANDSCAPE
EVOLUTION MODEL

I carried out the work described in this chapter with the guidance of Dr. Josh Roering and Dr. Alan Rempel. Both these coauthors contributed substantially by offering regular input and feedback on early results, as well as comments on drafts of the manuscript. I did all the writing.

1. Introduction

The topographic characteristics of a drainage basin are governed by complex interactions among various hillslope and channel processes, which in turn are sensitive to changes in baselevel, climate, and rock properties. A fundamental goal of studying earth surface processes is to disentangle this complex web of interactions in order to quantitatively relate observed topographic forms to the underlying geomorphic processes [National Research Council, 2010]. Such quantitative relationships are required in order to infer previous drivers of landscape evolution based on current landscape characteristics, as well as to predict how landscapes will respond to changes in these drivers.

A common approach for making such interpretations or predictions is to utilize geomorphic transport laws, which give sediment fluxes or incision rates based on topographic attributes, such as slope or drainage area, as well as material properties, such as bulk density or material strength [Dietrich *et al.*, 2003]. Ideally, these laws derive from simple mechanistic principles, and field, experimental, and mathematical modeling studies support their utility. Several geomorphic transport laws have been proposed and

proven useful for studies of landscape evolution, including soil transport on hillslopes [Culling, 1960; Roering *et al.*, 1999], soil production from bedrock [Heimsath *et al.*, 1997], and detachment-limited river incision [Howard and Kerby, 1983]. However, many other geomorphic processes lack established transport laws, especially those processes with rates and basic properties that vary dramatically over wide ranges of time and spatial scales. This paper focuses on one of these processes: deep-seated landslides, which we define here as extending to the depth of the lowermost weathering front, or arbitrarily deeper than about a meter.

Landslides with sizes and rates of movement spanning many orders of magnitude are the dominant erosion process in many catchments where erosion rates are high (greater than $\sim 1 \text{ mm yr}^{-1}$). The topography often manifests this process dominance through uniformly high relief and steep topographic gradients, or threshold hillslopes, which are insensitive to changes in uplift rate [Schmidt and Montgomery, 1995; Burbank *et al.*, 1996; Montgomery and Brandon, 2002], but can differ among bedrock types [Korup, 2008] and with climate [Gabet *et al.*, 2004]. Erosion rates derived from landslide frequency-size distributions confirm the importance of landsliding, which can keep pace with or even exceed the tectonic uplift rate [Hovius *et al.*, 1997; Blodgett and Isacks, 2007; Larsen and Montgomery, 2012]. These studies focused on some of the world's highest mountain ranges, with thousands of meters of relief, but many other regions have high erosion rates and only modest topographic relief of hundreds of meters [Griffiths, 1982; Milliman and Syvitski, 1992]. These landslide-driven settings are commonly underlain by mechanically weak bedrock that is especially prone to weathering and deep-seated landsliding. Deep-seated landslides keep pace with rapid

uplift rates by providing a large flux of sediment from a small area [Kelsey, 1978; Mackey and Roering, 2010], but little is known about how this process plays out at longer than historic timescales over which drainage basins evolve. Figure 1 provides one snapshot of such a landscape from the Waipaoa catchment, North Island, New Zealand, where Holocene erosion rates are 3–4 mm yr⁻¹ [Berryman *et al.*, 2000], and deep-seated landslides abound.

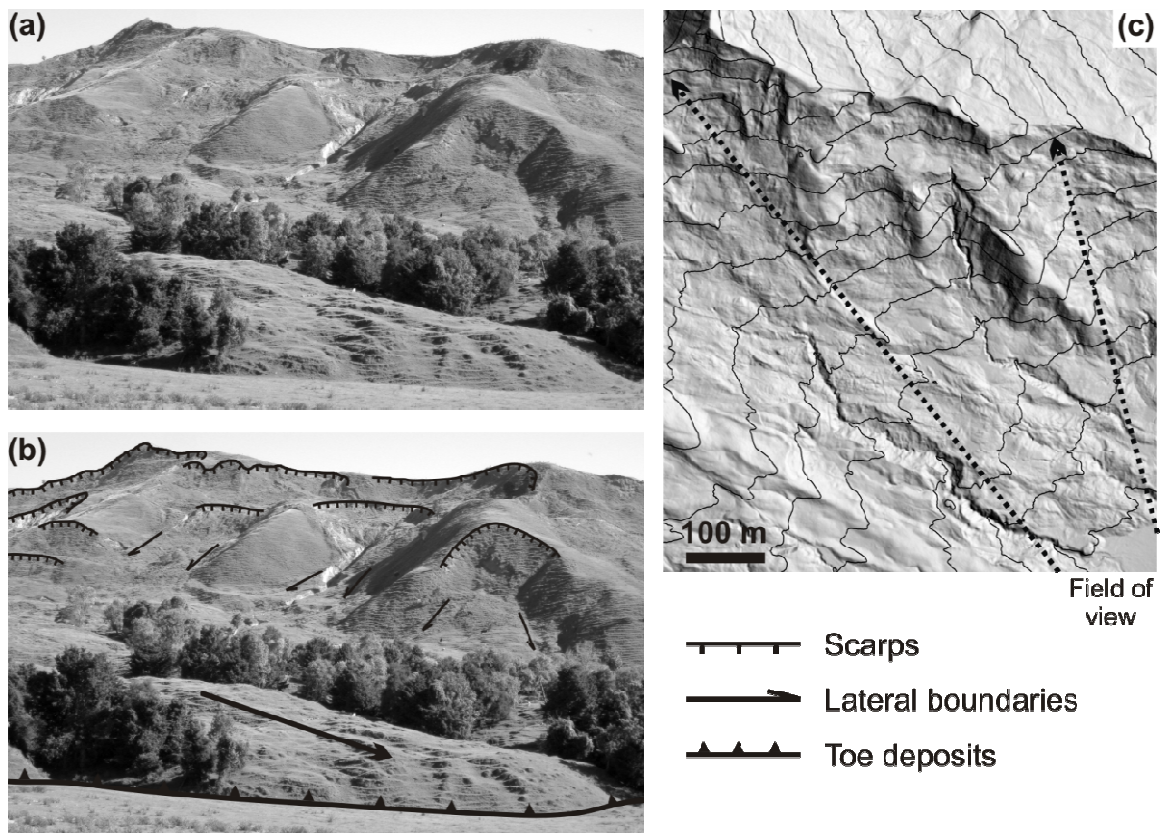


Figure 1. (a) Example of a catchment dominated by slow-moving, deep-seated landslides near the Waipaoa River, North Island, New Zealand ($\sim 38.34^\circ$ S and 177.93° E, indicated in Fig. 2). (b) The authors' interpretation of recent deep-seated landslide activity. Numerous scarps and landslide deposits exist amidst remnants of stable ridges. In the foreground, the individual landslides coalesce into a large, low gradient toe deposit. (c) LiDAR-derived hillshade map of the area. Contour interval is 20m and the dashed arrows approximately indicate the field of view in (a) and (b).

Despite the known importance of landslides to landscape evolution in a variety of settings, a geomorphic transport law for deep-seated landslides that can be straightforwardly implemented in a two-dimensional landscape evolution model remains elusive. *Ahnert* [1976, 1977] made a significant early attempt by including a plastic flow term, which was a function of weathering depth and the land surface slope, in a landscape evolution model, but explored only a limited range of model parameters. Later, *Kirkby* [1987] also developed a general model for mass movements, but explored only topographic profiles. *Hergarten and Neugebauer* [1998, 1999] demonstrated that a landslide flux depending on both depth and slope could produce stochastic landslide behavior consistent with the theory of self-organized criticality [*Bak et al.*, 1988]. Numerous models have invoked a threshold topographic gradient to simulate bedrock landsliding, but ignored the transport and deposition of sediment removed from slopes exceeding the threshold [*Tucker and Bras*, 1998; *van der Beek and Braun.*, 1999; *Dadson and Church*, 2005]. To date, *Densmore et al.* [1998] have included the most realistic treatment of deep-seated landsliding in a landscape evolution model by assigning a probability of failure to each grid cell in a model landscape based on a mechanistically determined critical hillslope height. Failed material was deposited in the valley network, where it could experience feedbacks with channel processes. Despite this rather detailed treatment of landsliding, however, the choices of failure probability and deposit geometry were arbitrary and not relevant to moderate relief catchments dominated by deep-seated landslides.

Here, we propose a general transport law for a range of deep-seated landslide processes motivated by observations of sites on the north island of New Zealand and the

northern California coast ranges of the United States. At these sites, we first utilize high-resolution topographic data to document a topographic signature of slow, deep-seated landslides. Motivated by empirical observations of vertical velocity profiles from deep-seated landslides throughout the world, we model landslides as non-Newtonian fluids so that landslide sediment flux depends nonlinearly on the landslide depth and topographic gradient. Flow law parameters for a given site can be estimated from borehole inclinometer data. When combined with existing geomorphic transport laws for soil creep, channel incision, and bedrock weathering, modeled landslides systematically inhibit channel formation and reduce catchment-averaged topographic gradients to produce the same topographic signatures observed in the study areas. We document a rich variety of landscapes produced over a wide range of model parameters, and show that a non-dimensional landslide number predicts the transition from stable, ridge-valley topography to landslide-dominated topography. The nature of this transition depends strongly on the steady state depth of bedrock weathering, which provides the mechanically weak material capable of generating landslides.

2. Topographic signatures of slow-moving, deep-seated landslides

To motivate and inform our landscape evolution model, we first describe the geology and tectonic settings of two study sites with extensive deep-seated landsliding, one in the Waipaoa catchment, North Island, New Zealand and the other along the Eel River, northern California, United States. We then use LiDAR-derived topographic data and slope-area statistics to document the topographic signatures of these deep-seated landslides.

2.1. Study areas

Our first study area is 160 km² to the east of the Waipaoa River near Whatatutu, North Island, New Zealand (Figure 2). Bedrock there is mainly mudstone of Miocene to Pleistocene age [Mazengarb and Speeden, 2000]. The Miocene Tolaga Group rocks are most abundant and consist of undifferentiated, massive, thinly bedded, and slightly calcareous mudstones with rare sandstone, tuff, and conglomerate beds. Small regions underlain by either Pliocene mudstones and sandstones of the Mangaheia Group or Pleistocene sediments of the Mangatuna Formation exist in the southern part of the study area. In Figure 2 and throughout the text we refer to these units collectively as mudstone. A melange of severely crushed Cretaceous to early Miocene lithologies in a sheared mudstone matrix underlies the northern part of the study area (Figure 2). The mudstone and melange portions of the study area both exhibit signs of widespread deep-seated landsliding, an example of which is shown in Figure 1. In the mudstone, deep-seated earthflows as well as shallow soil slips are common, while in the melange, earthflows are rampant and accompanied by minor gullying [Jessen *et al.*, 1999]. The New Zealand Land Resource Inventory Erosion Classification system [Eyles, 1985] defines each of these failure styles as follows: soil slips are rapid, shallow failures confined to less than one meter below the surface, gullying removes soil or soft rock by the overland flow of water in narrow, ephemeral channels, and earthflows involve the flow of soil and underlying regolith while retaining a deforming surface cover. In our study area, earthflows commonly occur as deep-seated landslide complexes with soil slips and gully erosion occurring on the surface of the complex. Field reconnaissance indicates that the

active deep-seated earthflows typically consist of well mixed, clay rich, weathered material with occasional logs and blocks of harder rock.

The study site resides in a tectonically active region and has been experiencing rock uplift of $\sim 0.7 \text{ mm yr}^{-1}$ since the late Pleistocene, based on the deformation of aggradational terraces along the Waipaoa River [Berryman *et al.*, 2000]. The elevation of the most recent terrace relative to the modern river indicates that the Waipaoa has incised at an average rate of 3–4 mm yr^{-1} over the past 18,000 yrs just to the west of our study area [Berryman *et al.*, 2000]. Throughout the Waipaoa catchment, terraces and numerous knickpoints in tributary headwaters have decoupled areas of relict topography from this incision [Crosby and Whipple, 2006; Gomez and Livingston, 2012], but in our study area this relict topography is relatively rare. Most of the mechanically weak slopes there have adjusted to the rapid decrease in baselevel through mass wasting processes [Marden *et al.*, 2008].

Our second study area is 180 km^2 along the main stem of the Eel River south of Alderpoint, California, United States (Figure 3). Bedrock there is the central belt of the Franciscan Complex, part of a metamorphosed and tectonically sheared Jurassic to Cretaceous accretionary prism [McLaughlin *et al.*, 2000]. A highly sheared melange of meta-argillite with isolated blocks of chert, greenstone, and serpentinite underlies most of the northeastern part of the study area. In Figure 3, we delineate the widespread melange unit and exclude the largest of the chert, greenstone, and serpentinite blocks, such as in the northern portion of the study area. Metasandstone and meta-argillite of the Broken Formation underlie most of the southwestern part of the study area, and we refer to this unit simply as sandstone throughout the text. Deep-seated earthflows with irregular gully

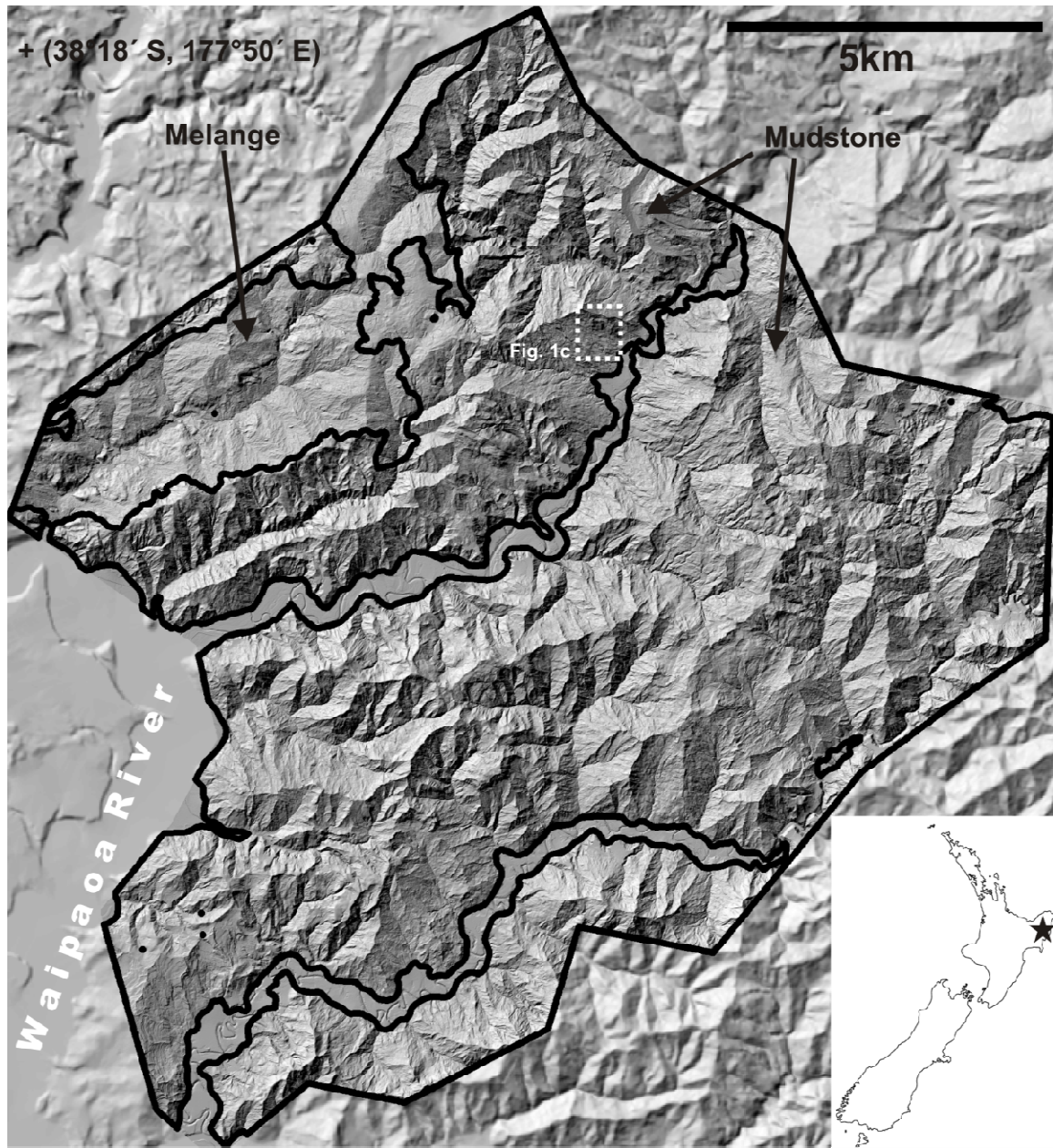


Figure 2. LiDAR-derived hillshade map of the Waipaoa study area, with outlined geologic units used in the slope-area plot (Figure 4). Dashed white rectangle outlines the location of Figure 1.

networks incised on their surfaces are common throughout the study area, but especially abundant in the melange unit [Mackey and Roering, 2011]. As in the Waipaoa study area, these earthflows transport weathered, clay-rich material with the occasional block of

harder rock or other debris. This study area is actively uplifting due to its position relative to the northward migrating Mendocino Triple Junction [*Furlong and Govers, 1999; Furlong and Schwartz, 2004*]. Using a geodynamic model, *Lock et al. [2006]* estimated a current uplift rate of $0.5\text{--}1\text{ mm yr}^{-1}$ in our study area, which is similar to the modern, catchment averaged erosion rate of $\sim 0.9\text{ mm yr}^{-1}$ estimated from suspended sediment data near the mouth of the Eel River [*Wheatcroft and Sommerfield, 2005*]. Earthflow movement alone is historically responsible for at least 0.45 mm yr^{-1} of erosion in the study area [*Mackey and Roering, 2011*].

In both study areas, we used 1 m resolution bare earth digital elevation models (DEMs) derived from Light Detection and Ranging (LiDAR) for our topographic analysis. NZ Aerial Mapping collected the LiDAR data for the Waipaoa site in 2010, and the National Center for Airborne Laser Mapping (NCALM) collected the Eel River LiDAR data in 2006.

2.2. Topographic signatures

Perhaps the most visually striking features of both study areas are the long, kilometer scale, quasi-planar hillslopes. Clear examples of this topography are the ridges and valleys in the Waipaoa study area surrounding and immediately southeast of the dashed white box in Figure 2, and the northeast trending ridges and valleys to the southwest of the Eel River in Figure 3. The gradient of these hillslopes is not controlled by rock structure in either study area, and instead, deep-seated landslides frequently span entire hillslopes from the ridge to the channel. This correspondence suggests that deep-seated landsliding might set this long hillslope length scale, a connection that we quantify



Figure 3. LiDAR-derived hillshade map of the Eel River study area, with outlined geologic units used in the slope-area plot (Figure 4). Dashed white rectangle outlines the location of Figure 5.

below using slope-area statistics and slope distributions, and then demonstrate with a mechanistic model in section 4.

Slope-area plots, which document topographic gradient as a function of drainage area, are a standard tool for identifying the boundaries between geomorphic process

regimes, such as the hillslope-valley transition [Tarboton *et al.*, 1991; Montgomery and Foufoula-Georgiou, 1993]. Figure 4a shows four slope-area plots, one for each main bedrock type in each of our study areas. We computed drainage area in each 1 m² grid cell using a steepest descent (D8) algorithm [O’Callaghan and Mark, 1984], and the topographic gradient using a centered finite difference approximation.

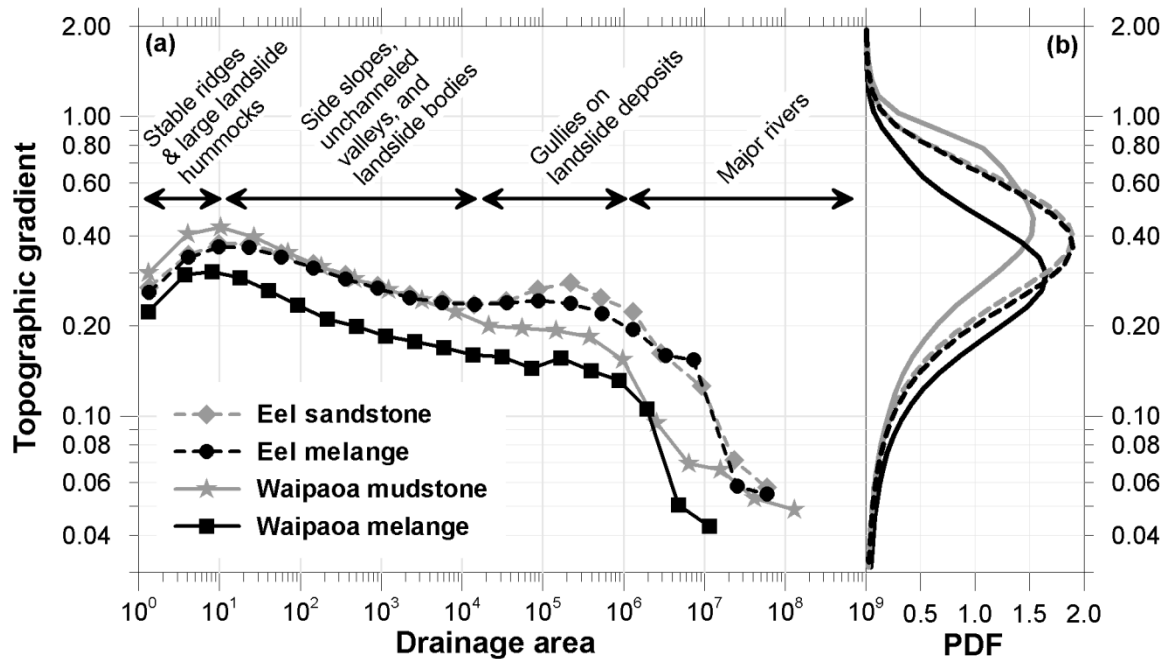


Figure 4. (a) LiDAR-derived slope-area plots for the Waipaoa and Eel River study areas, subdivided by geologic unit (Figures 3 and 4). The topographic gradient is the mean of 20 logarithmically spaced bins in drainage area, and standard errors are smaller than the symbols. Figure 5 illustrates the spatial arrangement of the four geomorphic process regimes indicated by the double headed arrows across the top of the plot. (b) Probability density functions of LiDAR-derived topographic gradients.

Despite differences in bedrock type, all the slope-area plots exhibit similar trends in the mean topographic gradient with increasing drainage area. In Figures 4 and 5, we identify four geomorphic process regimes between the breaks in slope of the slope-area plot, and illustrate the spatial pattern of these regimes. At small drainage areas, slope

increases rapidly until a drainage area of $\sim 10 \text{ m}^2$. These grid cells correspond to stable ridge tops as well as hummocks and scarps on the surfaces of active and relict deep-seated landslides (Figure 5, red terrain). From drainage areas of $\sim 10 \text{ m}^2$ to 10^4 m^2 , slope monotonically decreases to approximately the same magnitude as at a drainage area of $\sim 1 \text{ m}^2$, the smallest drainage area recorded by the DEM. In stable terrain, these grid cells delineate short side slopes adjacent to ridges and some unchanneled valleys, while in deep-seated landslide terrain, they are located just below scarps and in between hummocks throughout the landslide body (Figure 5, green terrain). At drainage areas of $\sim 10^4 \text{ m}^2$, topographic gradient tends to vary little or to slightly increase with increasing area up to $\sim 10^6 \text{ m}^2$. These data points correspond to small (meter-scale width and depth) channels, most of which are incised into the surfaces of active and relict deep-seated landslides (Figure 5, light blue lines). We suggest that this pattern records the interplay between deep-seated landslides and channel processes such that landslide deformation inhibits the channels from attaining convex longitudinal profiles. Finally, at drainage areas greater than $\sim 10^6 \text{ m}^2$, slope decreases rapidly with increasing area, and these grid cells delineate the major, valley-forming channels that define the kilometer-scale ridge-valley topography described earlier (Figure 5, dark blue line). The breadth of the distributions of topographic gradients (Figure 4b) reflects this diversity of processes regimes. Instead of a narrow distribution centered on a steep threshold slope, each of our study sites exhibits a wide range of slopes that result from interactions among deep-seated landslides and other geomorphic processes.

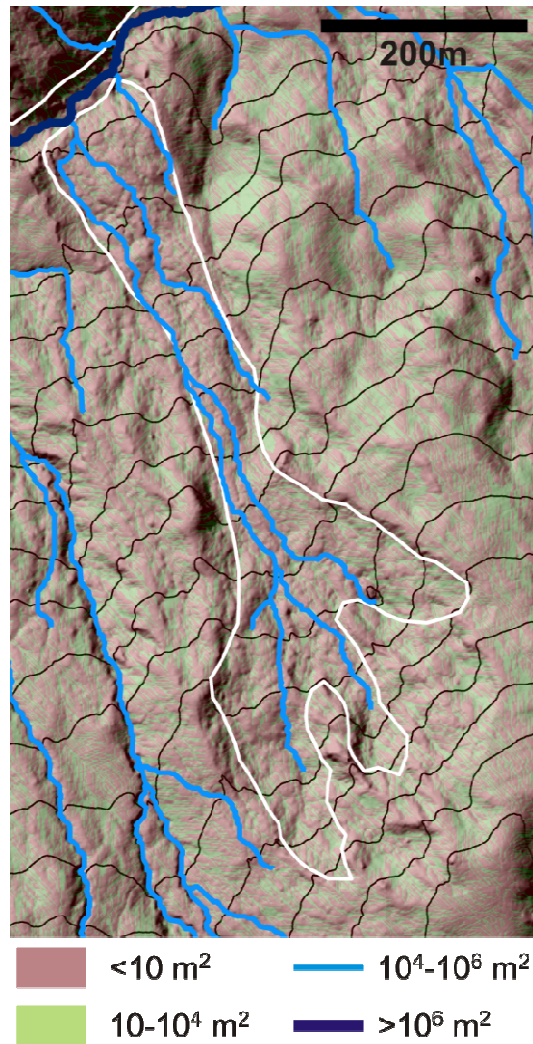


Figure 5. LiDAR-derived hillshade map (Figure 3, dashed white box), illustrating the spatial arrangement of the geomorphic process regimes identified in Figure 4. White outline delineates a historically active earthflow.

3. Landscape evolution model

3.1. Modeling goals

A landscape evolution model including deep-seated landsliding should be able to produce the most salient characteristics of deep-seated landslides in the context of landscape evolution. First, the model should produce the same topographic signatures identified in the preceding section, namely the long, quasi-planar hillslopes and the

process regimes in slope-area space (Figure 4). Additionally, landsliding is a stochastic process, where the rate and location of landsliding varies with time. Although this behavior results from mechanistic simulations with prescribed probabilities of slope failure [Densmore *et al.*, 1998, Stark and Guzzetti, 2009], we argue that it should also emerge from a purely mechanistic model. Detailed mapping of slow-moving, deep-seated landslides reveals that most deep-seated landslides are actually landslide complexes, with many generations of landslides superimposed on one another [Keefner and Johnson, 1983; Bovis, 1985; Mackey *et al.*, 2009; Mackey and Roering, 2011] reflecting this stochastic nature. Our goal then is to develop a simple mathematical landscape evolution model that produces these general landslide characteristics and behaviors and is applicable to a wide range of deep-seated landslides in different geologic settings. We do so below based on observations of our study areas and by using mechanistic equations for deep-seated landsliding and other geomorphic processes.

3.2. Geomorphic process model

Our landscape evolution model is based on conservation of mass, such that the change in the elevation of the land surface at any location in a landscape is the balance of fluxes into and out of that location [Kirkby, 1971; Smith and Bretherton, 1972; Ahnert, 1976; Willgoose *et al.*, 1991; Howard, 1994; Tucker and Bras, 1998]. In our study areas we identify four key fluxes, each related to a specific geomorphic process: (1) uplift of fresh bedrock relative to baselevel and its conversion to weathered material, (2) incision in channels, (3) near surface soil creep, and (4) deep-seated landslide deformation of weathered material. For these four processes, continuity requires that

$$\frac{\partial z}{\partial t} = \frac{\rho_r}{\rho_{ls}} U - \varepsilon - \nabla \cdot (\mathbf{q}_s + \mathbf{q}_{ls}), \quad (1)$$

where z (with units of length, L) is the land surface elevation, t (T) is time, ρ_r ($M L^{-3}$) is the bulk density of bedrock, ρ_{ls} ($M L^{-3}$) is the bulk density of weathered material, U ($L T^{-1}$) is the vertical uplift rate relative to baselevel, ε ($L T^{-1}$) is the vertical rate of channel incision, \mathbf{q}_s ($L^2 T^{-1}$) is the horizontal soil creep flux per unit contour width, \mathbf{q}_{ls} ($L^2 T^{-1}$) is the horizontal deep-seated landslide flux per unit contour width, and boldface type indicates vectors. In this framework, each geomorphic process represented on the right-hand side of equation (1) acts everywhere in the landscape at all times, and the landscape's particular form results from a competition among these processes over time [Smith and Bretherton, 1972; Howard, 1994; Tucker and Bras, 1998]. We propose a new geomorphic transport law to determine the deep-seated landslide flux, but rely on established geomorphic transport laws for the remaining geomorphic processes.

The first term on the right-hand side of equation (1) is a tectonic source term, where U is the vertical bedrock uplift rate relative to baselevel, and the density ratio, ρ_r/ρ_{ls} , allows for a volumetric expansion as that rock is weathered and converted to mobile sediment. In our model, we assume uplift is spatially and temporally uniform relative to a fixed baselevel in order to isolate the effects of the surface processes in shaping the modeled drainage basin.

The second term on the right-hand side of equation (1) describes the rate of incision due to overland flow of water. We use the stream power model [Howard and Kerby, 1983] to describe this process, which assumes that the incision rate is a power law function of drainage area and topographic gradient, such that

$$\varepsilon = KA^m |\nabla z|^n, \quad (2)$$

where K ($L^{1-2m} T^{-1}$) is a coefficient of erosion, A (L^2) is drainage area, $|\nabla z|$ is the magnitude of the topographic gradient, and m and n are dimensionless constants.

Equation (2) derives from the assumption that incision is detachment-limited and depends on the shear stress exerted on the ground surface beneath the flowing water. The drainage area, A , serves as a proxy for a characteristic water discharge, so that the exponent m reflects hydraulic geometry, drainage basin hydrology, and the dependence of incision on shear stress [Whipple and Tucker, 1999]. The topographic gradient is directly proportional to bed shear stress, so the exponent n reflects just the dependence of incision on shear stress.

The first flux term on the right-hand side of equation (1) describes the transport of near surface sediment by soil creep, which results from the dilation and subsequent settling of soil particles due to a variety of biologic and physical processes [Selby, 1993]. This flux increases with the magnitude of the topographic gradient, resulting in convex hillslopes [Gilbert, 1877, 1909; Davis, 1892]. We assume a linear relationship for this dependence [Culling, 1960; McKean *et al.*, 1993; Small *et al.*, 1999], which is applicable to gently-sloping, soil-mantled landscapes:

$$\mathbf{q}_s = -D\nabla z, \tag{3}$$

where D is a constant with the same units as a diffusivity ($L^2 T^{-1}$). If hillslopes steepen beyond a gradient of ~ 0.6 , a nonlinear dependence of flux on gradient is more appropriate [Roering *et al.*, 1999], but most parts of our study areas have gentler slopes (Figure 2b), and we focus on modeling landscapes with similarly gentle slopes.

The final flux term in equation (1) describes the transport of material by deep-seated landslides, the expression for which we propose based on observations of landslides in our study areas and similar landslides elsewhere. In general, to predict landslide flux at any location in a landscape, one needs to determine the landslide's thickness and velocity at that location, which suggests an equation of the form

$$q_{ts} = \overline{u}_{ts}H, \quad (4)$$

where \overline{u}_{ts} ($L T^{-1}$) is the vertically averaged velocity and H (L) is the thickness [Tucker and Hancock, 2010]. Most slope failures in both our study areas are composite earth slide-earth flows [Cruden and Varnes, 1996], which transport sediment down slope through a combination of fluid-like internal deformation and frictional slip on a shear surface [Brunsdon, 1980; Keefer and Johnson, 1983; Zhang et al., 1991; Swanston et al., 1995; Baum et al., 2004]. Vertical velocity profiles from borehole inclinometer data from these types of landslides therefore commonly have a plug flow shape in which a millimeter- to meter-scale shear zone at the base of the landslide accommodates most of the shear strain while material near the surface translates essentially as a rigid block [Keefer and Johnson, 1983; Iverson, 1986a; Pyles et al., 1987; Malet and Maquaire, 2003]. Properties of this shear zone, modulated by fluid pressure in the pore spaces as the material deforms, control landslide motion over daily to seasonal timescales [Iverson and Major, 1987; Hilley et al., 2004; Iverson, 2005; Schulz, 2009a]. However, it remains unclear how landslide deformation evolves over longer timescales when multiple generations of landslide activity distributed throughout a catchment interact with other geomorphic processes to set the long-term topographic characteristics of that catchment. We therefore adopt a general, continuum mechanics approach that reproduces the general form of landslide velocity profiles in order to simulate landslide behavior. In doing so, we deliberately sacrifice some of the details of short time scale landslide motion in exchange for a landslide model that easily couples with other geomorphic transport laws in a grid based numerical landscape evolution model. Specifically, we assume a non-Newtonian rheology [Barnes et al., 1989] for modeled landslides with the form

$$\dot{\epsilon}_{ij} = a\sigma_{II}^{p-1}\sigma_{ij}, \quad (5)$$

where $\dot{\epsilon}_{ij}$ (T^{-1}) is a component of the strain rate tensor, a ($L^p M^p T^{2p-1}$) is a flow law constant, σ_{II} ($M L^{-1} T^{-2}$) is the second invariant of the deviatoric stress tensor, p is a dimensionless flow law exponent, and σ_{ij} ($M L^{-1} T^{-2}$) is the corresponding component of the deviatoric stress tensor ($M L^{-1} T^{-2}$). *Iverson* [1986a, 1986b, 1986c] used a similar rheology-based approach to investigate the response of an earthflow to perturbations to its stress field, while *Vulliet and Hutter* [1988a, 1988b, 1988c] and *Vulliet* [2000] have accurately predicted the deformation of slow-moving landslides over yearly time scales using this and similar rheologies in finite element models. To implement equation (5) in a longer term landscape evolution model, we make a simplifying assumption that shear in the down slope direction is the dominant component of the deviatoric stress tensor, such that

$$\boldsymbol{\sigma} \approx \begin{pmatrix} 0 & 0 & \sigma_{xz} \\ 0 & 0 & \sigma_{yz} \\ \sigma_{zx} & \sigma_{zy} & 0 \end{pmatrix}, \quad (6)$$

where the subscripts refer to a slope-normal coordinate system. The second stress invariant then reduces to

$$\sigma_{II} = \sqrt{\sigma_{xz}^2 + \sigma_{yz}^2}. \quad (7)$$

Note that ice also deforms according to equation (5) with $p \sim 3$ [*Glen*, 1955], and glacier and ice sheet models commonly refer to this assumption as the shallow ice approximation [*Hutter*, 1983]. Using this shallow flow approximation, the shear stress, $\boldsymbol{\tau}$ ($M L^{-1} T^{-2}$) at depth, d (L), in a landslide is

$$\boldsymbol{\tau} = \rho_{ls} g d \nabla \mathbf{z}, \quad (8)$$

where g ($L T^{-2}$) is gravitational acceleration, and the shear strain rate is

$$\frac{\partial \mathbf{u}}{\partial z} = a(\rho g d)^p |\nabla \mathbf{z}|^{p-1} \nabla \mathbf{z}, \quad (9)$$

where \mathbf{u} ($L T^{-1}$) is the horizontal velocity vector. Integrating equation (9) once with respect to z gives the vertical velocity profile within the landslide,

$$\mathbf{u} = \frac{a(\rho_{ls}g)^p |\nabla \mathbf{z}|^{p-1}}{p+1} (H^{p+1} - (H-h)^{p+1}) \nabla \mathbf{z}, \quad (10)$$

where h (L) is height above the base of the landslide [*Turcotte and Schubert, 2002, p. 311*]. The shape of this velocity profile depends nonlinearly on h , with different values of p controlling shear localization. For $p = 1$, the velocity profile is parabolic as for a Newtonian viscous fluid, while the profile becomes more plug-like with increasing p and approaches that of a rigid block with an infinitesimally small shear zone as $p \rightarrow \infty$.

Integrating equation (10) with respect to z gives the depth-integrated landslide flux per unit contour width,

$$\mathbf{q}_{ls} = \frac{a(\rho_{ls}g)^p |\nabla \mathbf{z}|^{p-1}}{p+2} H^{p+2} \nabla \mathbf{z}, \quad (11)$$

which has the form of a geomorphic transport law and incorporates readily into the mass balance framework of equation (1).

Importantly, equation (11) depends strongly on landslide depth, which can vary substantially with time and location in a landslide-prone catchment. In order to predict landslide depth in our model, we note that the deepest shear zones determined from borehole measurements in deep-seated earthflows are typically at or just above the interface between intact bedrock and weathered material [*Swanson and Swanston, 1977; Brunnsden, 1984; Trotter, 1993*]. In our study areas, at several locations where deep channel incision has exposed shear zones, these zones also occur at or within a few centimeters of the interface between weathered material and fresh bedrock. This indicates that for earthflows to persist in a catchment, their shear zones must migrate

downward through time, relative to the uplifting terrain, in approximate concordance with the weathering front [Crozier, 1968; Gage and Black, 1979]. In this interpretation, deep-seated earthflows are not often deeper than the depth to the weathering front because the strength of the intact bedrock is much greater below this interface. Conversely, earthflows are not often much shallower than the depth of the weathering front because the driving shear stress is less near the surface. We incorporate this behavior into our model by tracking the weathering front and allowing all material above this interface to deform and contribute to the deep-seated landslide flux according to equation (11). Mobile landslide material at any location in the landscape can therefore come directly from bedrock weathering or from the transport of pre-existing weathered material. In a simpler one-dimensional model, *Booth and Roering* [2011] assumed a constant weathered zone depth as a first order approximation. Here, we instead follow previous landscape evolution models [*Ahnert*, 1976; *Densmore et al.*, 1998; *Hergarten and Neugebauer*, 1998, 1999] and let the production of weathered material from bedrock evolve with time according to

$$P = P_0 \exp\left(\frac{H}{H_0}\right), \quad (12)$$

where P ($L T^{-1}$) is the weathering rate, P_0 ($L T^{-1}$) is the maximum weathering rate when the weathered depth is zero, and H_0 (L) is a characteristic depth.

Substituting equations (2), (3), and (11) into equation (1) gives the governing equation for our landscape evolution model,

$$\frac{\partial z}{\partial t} = \frac{\rho_r}{\rho_{ls}} U - KA^m |\nabla \mathbf{z}|^n + D \nabla^2 z - \frac{\alpha(\rho_{ls}g)^p}{p+2} \nabla \cdot (|\nabla \mathbf{z}|^{p-1} H^{p+2} \nabla \mathbf{z}), \quad (13)$$

which describes the time evolution of the land surface elevation at every location in a drainage basin, and is coupled to equation (12) to determine H . We refer to the first term

on the right-hand side of equation (13) as the source term since it describes the steady addition of mass to the modeled catchment by tectonic uplift. We refer to the second term as the stream power term, which describes a nonlinear advective process with an effective velocity of $KA^m |\nabla z|^{n-1}$. The third term is the soil creep term, which has a diffusive form and an effective diffusivity of D . We refer to the last term as the landslide term, which has the form of nonlinear diffusion with an effective diffusivity of $a(\rho_{ts}g)^p |\nabla z|^{p-1} H^{p+2}/(p+2)$.

3.3. Numerical model

To test whether our landscape evolution model captures the fundamental landslide behaviors outlined in section 3.1, we implement equations (12) and (13) in a numerical model that simulates the evolution of a $\sim 1 \text{ km}^2$ catchment, which is similar in size to those in our study areas. We integrate equation (13) forward in time using finite differences (Appendix A) until the time-averaged sediment flux leaving the model catchment balances the tectonic flux into the catchment, and focus on these steady state model landscapes. The initial condition for the land surface elevation is a plane with meter-scale random roughness and a mean elevation of 2 m, while the initial condition for the elevation of the weathering front is also a plane with meter-scale roughness, but a mean elevation of 0 m. One corner of the modeled drainage basin is fixed at an elevation of 0 m while the rest of the model domain uplifts relative to this base level. No flux boundary conditions on the remaining boundary nodes ensure that material uplifted into the model domain leaves the catchment through this fixed elevation outlet. To focus our modeling efforts, we use the same constant values for some of the free parameters in equation (13), such that $\rho_r = 2700 \text{ kg m}^{-3}$, $\rho_{ts} = 1700 \text{ kg m}^{-3}$, $m = 0.5$, $n = 1$, and $p = 3$ in

all our model runs. Using a fixed value of p is not ideal because previous studies have found best-fit values of p ranging from 1 to 15 [Vulliet and Hutter, 1988a, 1988b, 1988c; Vulliet, 2000], but our choice of $p = 3$ allows the model to run in a reasonable amount of time since it strongly influences the maximum stable time step (Appendix A).

4. Results

Using the numerical model described above, we fully explore the parameter space and characterize the tectonic and geomorphic conditions at which landslides occur in the modeled catchment. We first estimate the flow law constant, a (equations (5)-(11)), for a variety of deep-seated landslides throughout the world (Table 1). We then show that a non-dimensional number comparing the magnitude of the landslide term to the stream power and soil creep terms predicts when a landscape transitions from being dominated by soil creep and stream power to being dominated by deep-seated landslides. For thick steady state weathered zones, a temporally steady landslide flux reduces catchment averaged slope and widens the valley spacing when this number exceeds a constant critical value. For thin steady state weathered zone thicknesses, landslide dominated landscapes occur over a relatively narrow range of the non-dimensional landslide number that depends on depth, and landslide flux varies dramatically in both space and time. Last, we demonstrate that the model produces the same topographic signatures, recorded by slope-area statistics, as are found in our study areas.

Table 1. Estimation of the Flow Law Constant, a .

Reference	Reference figure	Density, ρ_{ls} (kg m ⁻³)	Depth, H (m)	Slope, $ \nabla z $	Flow law constant, a (m ³ kg ⁻³ yr ⁵) ^a
<i>Borgatti et al.</i> [2006]	Fig. 8	2000	16	0.25 ^c	10 ⁻⁶¹
<i>Cristescu et al.</i> [2002]	Fig. 12	1700 ^b	20	0.29 ^d	10 ⁻⁶²
	Fig. 13	1700 ^b	8	0.36 ^d	10 ⁻⁶¹
<i>Keefer and Johnson</i> [1983]	Fig. 29	1730	0.5	0.27 ^e	10 ⁻⁵⁵
<i>Malet and Maquaire</i> [2003]	Fig. 3	1700 ^b	9	0.46 ^e	10 ⁻⁶¹
<i>Savage and Wasowski</i> [2006]	Fig. 8	1700 ^b	17	0.12 ^d	10 ⁻⁶⁰
<i>Vulliet and Hutter</i> [1988a]	Fig. 1a, Table 2	2041	26.5	0.23	10 ⁻⁶³
		2041	20	0.16	10 ⁻⁶²
		2041	14.85	0.19	10 ⁻⁶²
		2041	22	0.07	10 ⁻⁶²
		2041	15.35	0.29	10 ⁻⁶²
<i>Vulliet and Hutter</i> [1988b]	Fig. 8	1700 ^b	7	0.27 ^e	10 ⁻⁵⁹
<i>Zhang et al.</i> [1991]	Fig. 4, G	1800	5	0.47	10 ⁻⁵⁸
	Fig. 4, H	1800	5	0.09	10 ⁻⁵⁶
	Fig. 4, M	1800	6	0.14	10 ⁻⁵⁸
	Fig. 4, N	1800	3	0.32	10 ⁻⁵⁷

^aFrom best-fit velocity profile when $p = 3$.

^bApproximate density because not provided in reference.

^cApproximate slope based on reported mobilized friction angle.

^dApproximate slope based on reported topographic maps.

^eApproximate slope based on reported average slope.

4.1. Estimating the landslide parameter, a

To determine what values of a to use in our numerical simulations, with the flow law exponent fixed at $p = 3$, we applied equation (10) to previously studied deep-seated landslides with observations of velocity, depth, and topographic gradient from borehole data (Table 1) [*Keefer and Johnson*, 1983; *Vulliet and Hutter*, 1988a, 1988b; *Zhang et al.*, 1991; *Cristescu et al.*, 2002; *Malet and Maquaire*, 2003; *Borgatti et al.*, 2006; *Savage and Wasowski*, 2006]. For studies that reported a complete vertical velocity profile, we iteratively determined the value of a that minimized the root mean square error between

the predicted and observed velocity profiles. If the study provided only a surface velocity, we set $h = H$ in equation (10) and solved for a directly. The best fit values of a range from $\sim 10^{-63} m^3 kg^{-3} yr^5$ for the slower and deeper landslides to $\sim 10^{-55} m^3 kg^{-3} yr^5$ for the faster and thinner landslides. At a given study site, a often varies by an order of magnitude or more when determined from borehole data at different locations or at different times on the same landslide. This could be due to the material properties of the landslide actually changing from one location or time to another, or might be an artifact of using a shallow flow approximation, which ignores longitudinal stresses. Nonetheless, these order of magnitude estimates suggest the approximate range of a to explore in our numerical simulations described below.

4.2. The non-dimensional landslide number

One measure of the importance of landslides in shaping a model catchment is the size of the landslide term (the last term on the right-hand side of equation (13)) relative to the stream power and soil creep terms (the second and third terms on the right-hand side of equation (13), respectively). To compare the sizes of these terms, we non-dimensionalize equation (13) taking ζ as a characteristic vertical length scale associated with uplift, ξ as a characteristic vertical length scale associated with weathering, λ as a characteristic horizontal length scale, and $\theta = \zeta/U$ as a characteristic time scale. Substituting $z^* = z/\zeta$, $H^* = H/\xi$, $x^* = x/\lambda$, $y^* = y/\lambda$, and $t^* = t/\theta$ gives the non-dimensional governing equation as

$$\frac{\partial z^*}{\partial t^*} = \rho^* - K^* A^{*m} |\nabla \mathbf{z}^*|^n + D^* \nabla^2 z^* - V^* \nabla \cdot (|\nabla \mathbf{z}^*|^{p-1} H^{*p+2} \nabla \mathbf{z}^*), \quad (14)$$

where

$$\rho^* = \frac{\rho_r}{\rho_{ts}}, \quad (15a)$$

$$K^* = \frac{K\lambda^{2m-n}\zeta^n}{U}, \quad (15b)$$

$$D^* = \frac{D\zeta}{U\lambda^2}, \quad (15c)$$

$$\text{and } V^* = \frac{a(\rho_{ts}g)^p \zeta^p \xi^{p+2}}{U(p+2)\lambda^{p+1}}, \quad (15d)$$

and the asterisks denote dimensionless quantities. To capture the full dynamics of the landscape evolution model with the non-dimensional numbers given by equations (15a-d), it is important to select characteristic length scales appropriate to the size and shape of the model catchment. The steady state hillslope relief is a natural choice for ζ , which is generally not known a priori for a given model run, but is easily determined from the resulting steady state modeled landscape. The steady state weathered zone depth is a natural choice for ξ , which can be predicted for any model run by

$$\xi = -H_0 \ln\left(\frac{U}{\rho_0}\right). \quad (16)$$

For the characteristic horizontal length scale, λ , we use the hillslope length scale, defined as one half of the first-order valley spacing. For modeled landscapes where landsliding is unimportant ($V^* = 0$), this can be estimated using

$$\lambda = \left(\frac{D}{K}\zeta^{1-n}\right)^{\frac{1}{2(m+1)-n}}, \quad (17)$$

assuming that the stream power and soil creep terms are the only significant contributors to sediment transport in the catchment [Perron *et al.*, 2008a]. Substituting equation (17) into equation (15d) and assuming that the catchment's mean topographic gradient, $|\overline{\nabla z}|$, is equivalent to ζ/λ yields a single non-dimensional number that captures the importance of the landslide term relative to the stream power and soil creep terms:

$$V^* = \frac{a(\rho_{ts}g|\overline{\nabla z}|)^p \xi^{p+2}}{U(p+2)} \left(\frac{K}{D\zeta^{1-n}}\right)^{\frac{1}{2(m+1)-n}}. \quad (18)$$

For $m = 0.5$ and $n = 1$, as we use in this study, equation (18) simplifies to

$$V^* = \frac{a(\rho_{ls}g|\nabla z|)^p \xi^{p+2}}{U^{(p+2)}} \left(\frac{K}{D}\right)^{\frac{1}{2}}, \quad (19)$$

which highlights the relative importance of each parameter on the right-hand side in determining V^* for a model catchment. All else being equal, V^* increases relatively weakly with a and relatively strongly with ρ_{ls} , g , $|\nabla z|$, or ξ because each of these variables directly influences the magnitude of the deep-seated landslide flux (equation (11)). An increase in K or a decrease in D causes a weak increase in V^* by decreasing the hillslope length scale, which increases the mean topographic gradient and therefore indirectly increases the landslide flux. An increase in U causes a decrease in V^* because it increases the tectonic flux relative to the landslide flux.

To test the validity of V^* for predicting landscape form, we ran a series of models as described in section 3.3 with six different combinations of variables on the right-hand side of equation (19) and tracked the mean topographic gradient and mean valley spacing of the resulting steady state topography (Table 2, Figure 6). We first determined unique combinations of U , D , and K that produced landscapes with mean topographic gradients ranging from ~ 0.1 to 0.5 with the landslide term set to zero. We then ran the model 100 times, each time with a different value of a , suggested by our estimates in section 4.1, in order to span a wide range of V^* that included the transition from soil creep and stream power dominated landscapes to deep-seated landslide dominated landscapes. All these model runs had steady state weathered zone thicknesses (equation (16)) that were large compared to the initial weathered zone depth of ~ 2 m. We determined mean valley spacing by estimating the power spectrum of the steady state topography using the two-dimensional discrete Fourier transform and then identifying the peak of the spectrum after being normalized by a red noise spectrum [Perron *et al.*, 2008b].

Table 2. Parameters Used to Generate Figure 6.

Run #	U (m yr ⁻¹)	D (m ² yr ⁻¹)	K (yr ⁻¹)	P_0 (m yr ⁻¹)	H_0 (m)	a range (m ³ kg ⁻³ yr ⁵)	Symbol
1	1.0×10^{-5}	4.0×10^{-3}	3.0×10^{-4}	2.0×10^{-5}	8	10^{-65} – 10^{-59}	◆
2	1.0×10^{-5}	4.0×10^{-3}	2.0×10^{-4}	2.0×10^{-5}	16	10^{-67} – 10^{-61}	+
3	1.0×10^{-4}	1.0×10^{-2}	3.0×10^{-3}	2.0×10^{-4}	4	10^{-64} – 10^{-58}	●
4	1.0×10^{-4}	1.0×10^{-2}	1.3×10^{-3}	2.0×10^{-4}	8	10^{-66} – 10^{-60}	▲
5	1.0×10^{-4}	1.0×10^{-2}	7.0×10^{-4}	2.0×10^{-4}	16	10^{-67} – 10^{-61}	▼
6	1.0×10^{-3}	1.0×10^{-2}	7.0×10^{-3}	4.0×10^{-4}	16	10^{-68} – 10^{-62}	★

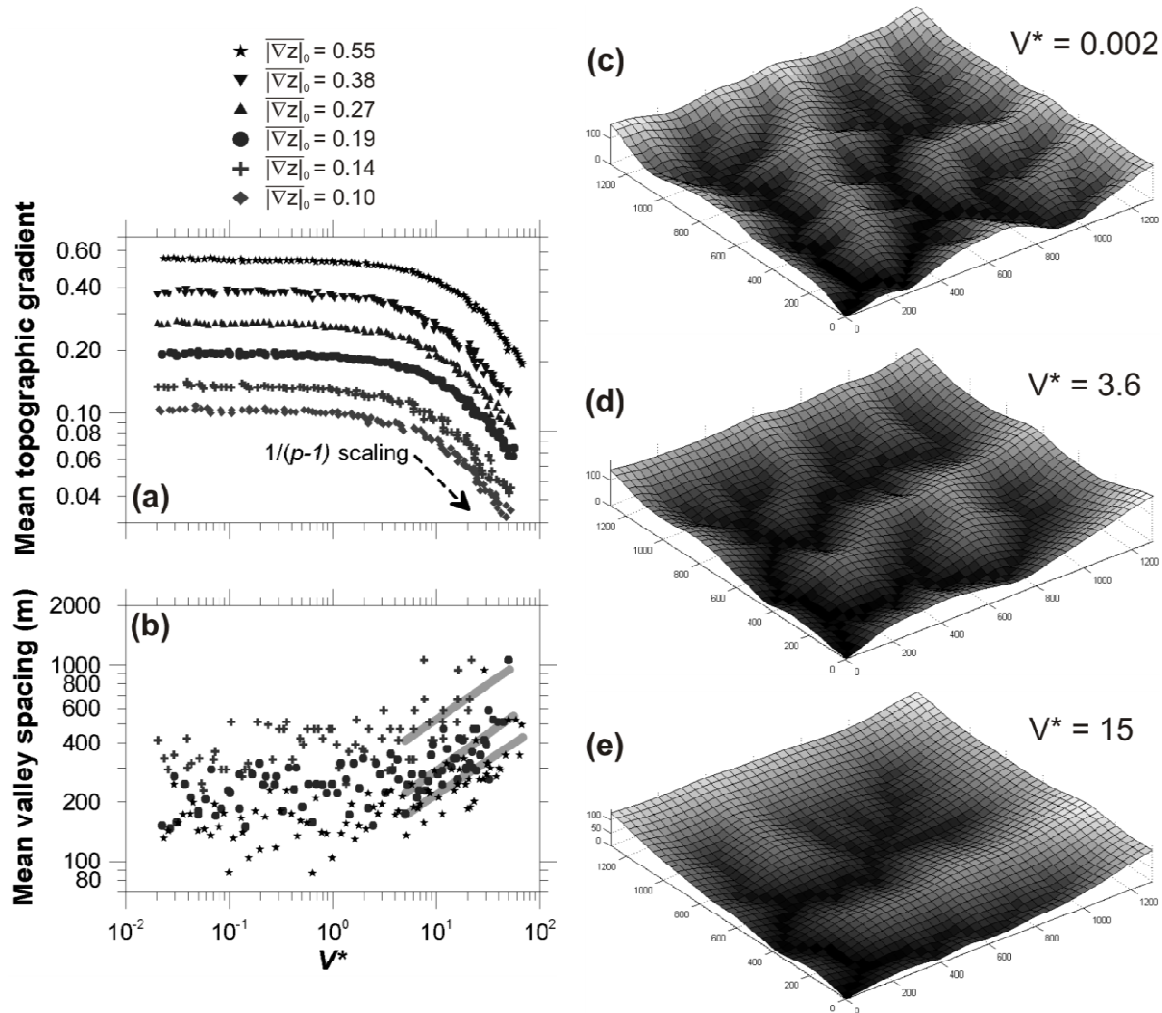


Figure 6. Dependence of (a) mean topographic gradient and (b) mean valley spacing of modeled catchments on V^* for thick steady state weathered zones. Table 2 gives the parameters used for each of the 6 model runs. For clarity only 3 of the runs are shown in (b), and the grey lines are statistically significant fits for the data with $V^* > 5$, which highlight the increase in valley spacing with V^* in the landslide flux dominated regime. (c)-(e) are examples of steady state landscapes resulting from small, moderate, and large values of V^* , respectively, from run #5 (▼ symbols). Shading is elevation, and axes are in meters.

For each of these model landscapes, the landslide term affects neither the mean topographic gradient (Figure 6a) nor the mean valley spacing (Figure 6b) when V^* is less than ~ 1 , and these landscapes (Figure 6c) are statistically indistinguishable from landscapes where $V^* = 0$. At $V^* \sim 1$, the mean topographic gradient begins to decrease with V^* , the mean valley spacing begins to increase, and hillslopes become more planar in both profile and plan form (Figure 6d). Topographic gradient and valley spacing continue their trajectories with additional increases in V^* , and when V^* is greater than ~ 5 , the low gradient, quasi-planar hillslopes begin to approach the scale of the modeled catchment (Figure 6c). We refer to this critical value of V^* as V^*_{crit} since it marks the transition from soil creep and stream power dominated landscapes to deep-seated landslide dominated landscapes. In this regime, the mean topographic gradient tends to decrease as $V^{*-1/(p-1)}$ (Figure 6a), as predicted by equation (14) with $K^* = 0$ and $D^* = 0$. Mean valley spacing increases as $V^{*0.36 \pm 0.32}$, $V^{*0.38 \pm 0.13}$, and $V^{*0.35 \pm 0.13}$ ($V^*_{mean} \pm 95\%$ confidence interval) for model runs 2, 3, and 6, respectively (Figure 6b).

None of these six model runs generate stochastic landslide behavior at steady state, so the flux of material out of each location in the model catchment exactly balances the sum of the vertical tectonic flux and the horizontal flux of material from upslope into that location at all times. The landslide term contributes a temporally constant proportion of the total flux at each location, but its relative contribution varies spatially. Because the weathered zone depth, which sets landslide thickness, attains its constant steady state value under these model conditions, the topographic gradient alone controls the landslide flux throughout the catchment. Landslide fluxes are therefore highest and much larger than the soil creep and stream power fluxes in valley heads and midway up valley side

slopes where topographic gradients are highest and the topography transitions from being convex to concave.

4.3. Controls on stochastic landslide behavior

To determine how the steady state weathered zone thickness affects the nature of the transition from soil creep and stream power dominated landscapes to deep-seated landslide dominated landscapes, we ran another series of models with different maximum weathering rates (equation (12)), which gave shallower steady state weathered zone depths (equation (16), Table 3). For this series of model runs, we kept $U = 1 \text{ mm yr}^{-1}$, $D = 0.01 \text{ m}^2 \text{ yr}^{-1}$, and $K = 0.01 \text{ yr}^{-1}$ constant, then ran the model 100 times over a range of a values and determined the mean topographic gradient and valley spacing as described at the end of section 4.2.

Table 3. Parameters Used to Generate Figure 7.^a

Run #	P_0 (m yr ⁻¹)	ζ (m)	a range (m ³ kg ⁻³ yr ⁵)	Symbol
1	2.0×10^{-3}	2.8	$10^{-65} - 10^{-59}$	◆
2	1.7×10^{-3}	2.1	$10^{-67} - 10^{-61}$	+
3	1.3×10^{-3}	0.9	$10^{-64} - 10^{-58}$	●
4	1.1×10^{-3}	0.4	$10^{-66} - 10^{-60}$	★

^a $U = 1 \text{ mm yr}^{-1}$, $D = 0.01 \text{ m}^2 \text{ yr}^{-1}$, and $K = 0.01 \text{ yr}^{-1}$ held constant.

For each of these modeled landscapes, the mean topographic gradient is unaffected when $V^* < V^*_{crit}$ (Figures 7a and c). However, unlike the gradual transition to the steady flux landslide dominated regime reported in section 4.2, the onset of landsliding in these model runs is abrupt and marked by a dramatic decrease in mean topographic gradient when $V^* > V^*_{crit}$ (Figures 7a, d, and e). At this transition, stochastic landslide activity is triggered, and the landslide flux varies dramatically in both time and space, even when the landscape is at a temporally averaged steady state. Individual

landslide events tend to initiate in valley heads where topographic gradients are highest, then run out and deposit weathered material in the low order channel network. This episodic flux erodes weathered material locally at rates far exceeding the steady tectonic uplift rate and prevents the weathered zone from attaining its predicted steady state value throughout the model catchment. All else being equal, a decrease in the steady state weathered zone thickness causes a reduction in mean topographic gradient at a lower V^*_{crit} than predicted for the thick weathered zone depths of section 4.2. For example, for the combination of parameters explored here (Table 3), a reduction of thickness from 2.8 m to 0.4 m causes a decrease in V^*_{crit} of ~ 4 orders of magnitude, which reflects the sensitivity of the landslide flux to weathered zone depth.

In model runs 1 and 2, mean valley spacing increases with V^* when $V^* > V^*_{crit}$, but mean valley spacing is insensitive to V^* over the range investigated for model runs 3 and 4 (Figure 7b, Table 3). Qualitatively, this difference relates to the size of landslides and their deposits in the low order channel network. For the relatively thin weathered zones of runs 3 and 4, most landslides are small, and their thin deposits are easily incised in low order valleys. For the relatively thick weathered zones of runs 1 and 2, landslides tend to be larger and their thicker deposits more effectively inhibit incision in the low order channel network, widening valley spacing.

4.4. Landslide regime phase space

The dependence of V^*_{crit} on the steady state weathered zone thickness, ζ , described above suggests a phase space for classifying the three main types of landscapes produced by the model: landscapes with no landsliding, steady landsliding, or stochastic landsliding (Figure 8). We generated this sample phase space for the same values of U ,

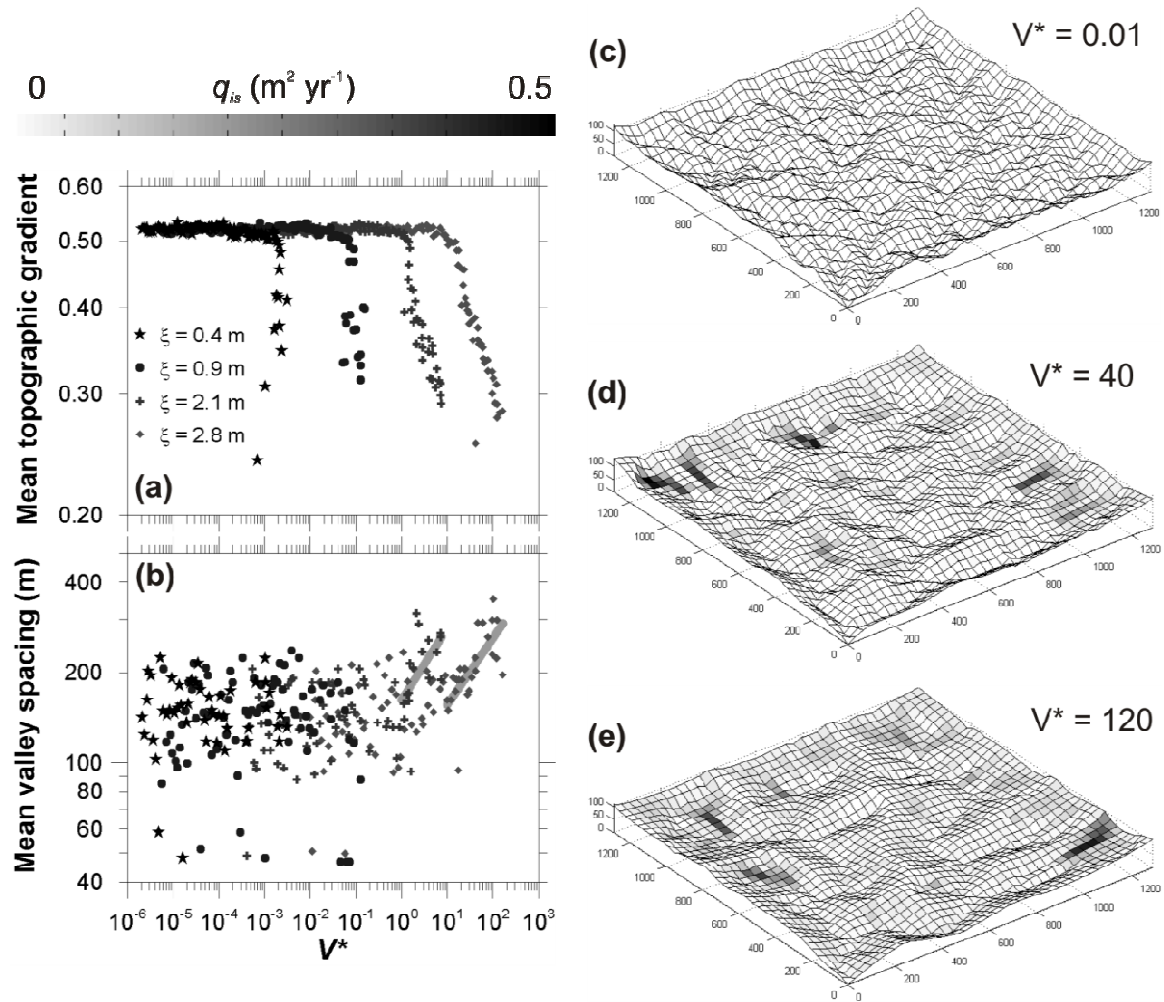


Figure 7. Dependence of (a) mean topographic gradient and (b) mean valley spacing of modeled catchments on V^* for thin steady state weathered zones and stochastic landslide activity. Table 3 gives the parameters used for each of the 4 model runs. Grey lines in (b) are statistically significant fits for the data with $V^* > 10$ and $V^* > 1$ for runs 1 and 2, respectively. (c)-(e) are examples steady state landscapes resulting from small, moderate, and large values of V^* , respectively, from run #1 (\blacklozenge symbols). Shading is landslide flux per unit contour width, and axes are in meters.

D , and K as in section 4.3 by running the model over values of ζ ranging from ~ 0.8 to 8 m and values of a ranging from 10^{-64} to 10^{-58} $\text{m}^3 \text{kg}^{-3} \text{yr}^5$.

On the left-hand side of this phase space, V^* is small and no landslides occur, indicating that the landslide term is unimportant relative to the soil creep and stream power terms in shaping the topography. Landscapes in this regime consist of ridges and

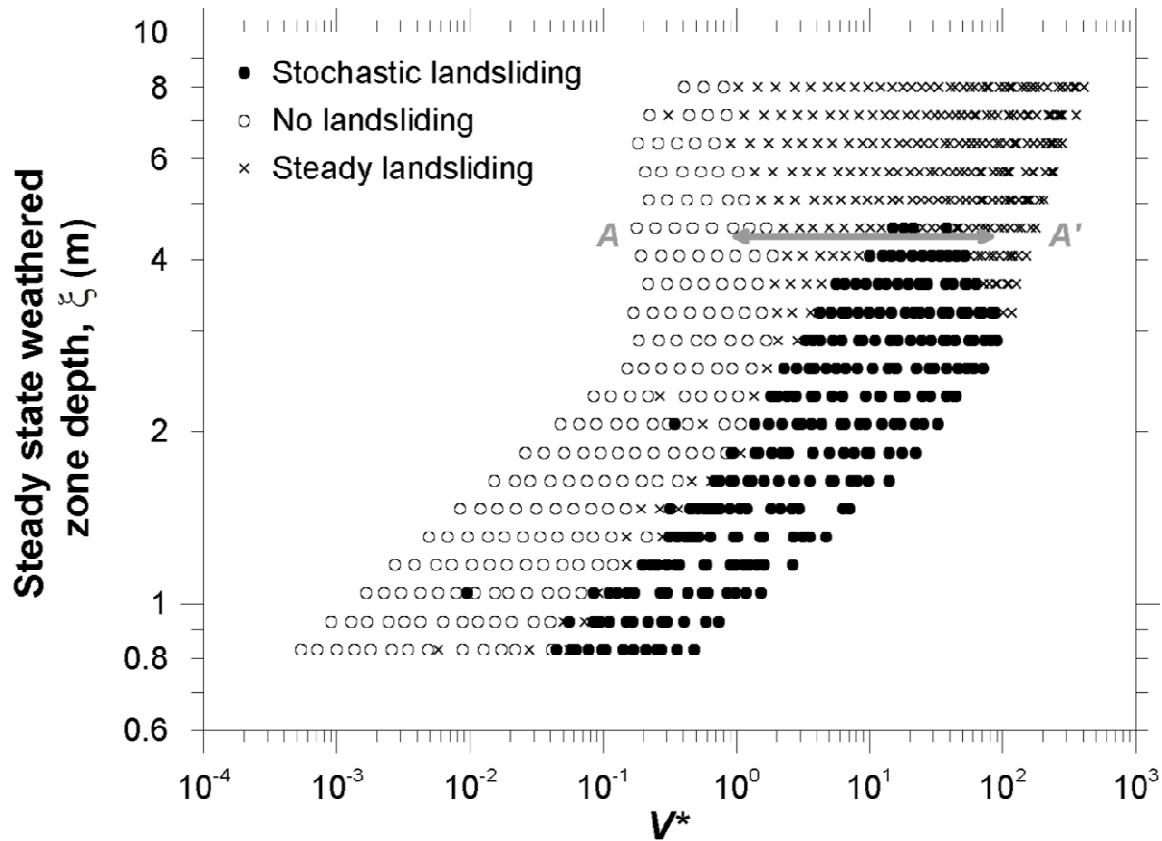


Figure 8. Phase space illustrating the 3 model landscape regimes (no landsliding, steady landsliding, and stochastic landsliding) for combinations of V^* and ζ . In the no landsliding regime, defined by $|\overline{\nabla z}| \geq 0.95 |\overline{\nabla z}|_0$ and $\text{std}(H) < 1.05 \text{std}(H)_0$, where the subscripted 0 indicates the background mean value when $V^* = 0$, the magnitude of the landslide term is too small relative to the soil creep and stream power terms to produce a landslide flux large enough to affect the topography. In the steady landsliding regime, defined by $|\overline{\nabla z}| < 0.95 |\overline{\nabla z}|_0$ and $\text{std}(H) < 1.05 \text{std}(H)_0$, the magnitude of the landslide relative to soil creep and stream power terms is large enough that a steady landslide flux reduces the mean topographic gradient and increases mean valley spacing. In the stochastic landsliding regime, defined by $\text{std}(H) \geq 1.05 \text{std}(H)_0$, thinner steady state weathered zone depths allow landsliding that varies in space and time to occur. Transect A-A' indicates the range of landscapes investigated in section 4.4 and shown in Figure 9.

valleys, such as those in Figures 6c and 7c, and the combination of soil creep on hillslopes and fluvial incision in channels alone keeps pace with tectonic uplift. These landscapes have mean topographic gradients and standard deviations of weathered zone

depths that vary by less than 5% from their reference values from landscapes where $V^* = 0$.

In the upper portion of the phase space, when V^* is greater than ~ 1 , most landscapes have a large, temporally steady, but spatially variable landslide flux. Landscapes in this regime have gentle, long, and quasi-planar hillslopes, such as in Figures 6d and e. Each of these landscapes has a mean topographic gradient that is less than the reference value by at least 5% and a standard deviation of weathered zone thicknesses that differs from the reference value by less than 5%. For this combination of model parameters and initial conditions, if ζ is greater than ~ 5 m, all landscapes with $V^* > 1$ have this characteristic steady landslide flux, but when ζ is less than ~ 5 m, this regime begins to encounter the stochastic landsliding regime. This transition thickness is similar in size to the deepest pockets of weathering present during the initial stages of landscape evolution (section 3.3), suggesting that the initial weathered zone thickness exerts a strong control on whether steady or stochastic landsliding develops as the model landscape attains a steady state.

In the lower right portion of the phase space, stochastic landsliding occurs when V^* exceeds a critical value that depends on the steady state weathered zone thickness. Figures 7d and e give examples of these landscapes, which are defined by a standard deviation of weathered zone thicknesses that exceeds the reference value by at least 5%. For shallow weathered zone depths of less than ~ 3 m, the transition from the no landsliding regime to this stochastic landsliding regime is abrupt and occurs at lower values of V^* for lower values of ζ . For moderate weathered zone depths of ~ 3 to 5 m, landscapes first transition from no landsliding to steady landsliding at $V^* \sim 1$ before

transitioning again to this stochastic landsliding regime at a higher V^* . Further increases in V^* then push the landscape back into the steady landsliding regime. This last transition does not occur for shallower weathered zone depths less than ~ 3 m because the stochastic landsliding reduces the mean topographic gradient to near zero before steady landsliding turns on.

The upper boundary of the stochastic landsliding regime in this phase space increases with the model's initial weathered zone thickness, reflecting how the landscape evolves to steady state. When the weathered zone is initially very deep, a thick mantle of weathered material already covers much of the landscape as it steepens from the nearly flat initial surface. Upstream propagation of knickpoints as the fluvial network becomes established then rapidly steepens areas underlain by this thick weathered zone, triggering discrete landslide events. These landslides' deposits are also thick compared to the steady state weathered zone depth and have low topographic gradients, so they persist as the landscape uplifts, and can be rapidly incised again at a later time, repeating the cycle.

4.5. Topographic signatures

Each of these three regimes – no landsliding, steady landsliding, and stochastic landsliding – produces visually distinctive landscapes, the characteristics of which we quantify using the spatial variability of weathered zone depths and slope-area plots of the resulting topography. To illustrate each of these regimes, we characterized landscapes along transect $A-A'$ in Figure 8 (Figure 9). For these model runs, we maintained a predicted steady state weathered zone depth (equation (16)) of $\xi = 4.4$ m ($P_0 = 0.003$ and $H_0 = 4$), and varied a from 10^{-62} to 10^{-58} $\text{m}^3 \text{kg}^{-3} \text{yr}^5$. Other parameters were $U = 1$ mm yr^{-1} , $K = 0.01$ yr^{-1} , and $D = 0.01$ $\text{m}^2 \text{yr}^{-1}$.

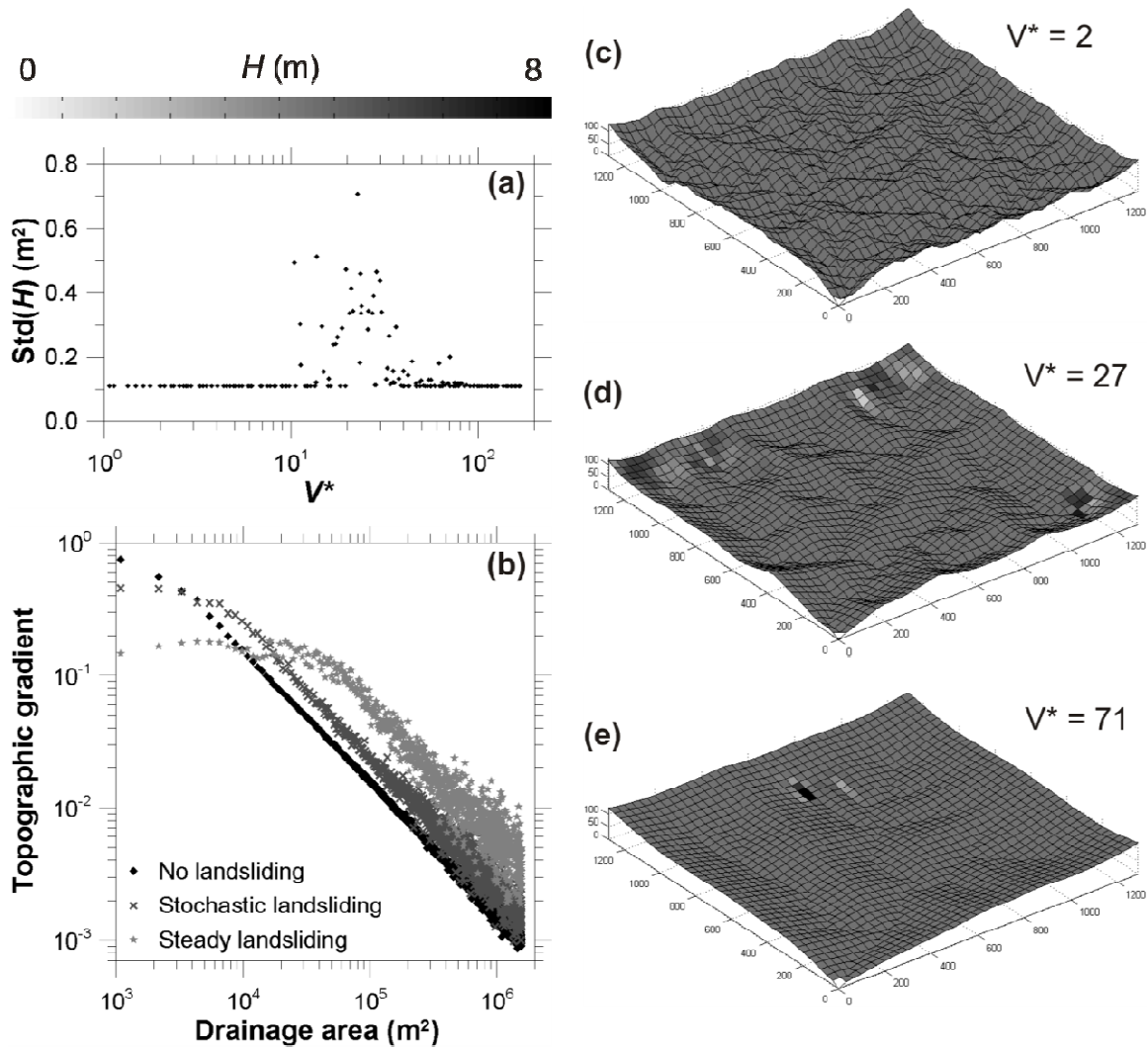


Figure 9. (a) Dependence of the standard deviation of weathered zone depths on V^* along transect A-A' in Figure 8. (b) Average slope-area plots for model landscapes in the no landsliding regime, the stochastic landsliding regime, and the steady landsliding regime. (c)-(e) are examples of landscapes in each of these three regimes, shaded by weathered zone thickness, H . The axes are in meters.

In the no landsliding regime, where V^* is small, the weathered zone depth attains a spatially and temporally constant steady state value, recorded by a low standard deviation of weathered zone depths that is consistent among model runs (Figure 9a and c). At $V^*_{crit} \sim 10$ for these parameters, the landscape abruptly transitions into the stochastic landsliding regime, marked by the ~ 5 -fold increase in the standard deviation

of weathered zone thicknesses. Stochastic landsliding directly causes this increase in variability by perturbing the weathered zone to shallower depths at landslide initiation sites and thickening the weathered zone in depositional areas (Figure 9d). This effect is strongest when V^* is just greater than V^*_{crit} , and the variability of weathered zone thickness tends to decrease with further increases of V^* . By $V^* \sim 40$ an increased proportion of model runs do not produce any stochastic landsliding, and those that do have only modestly elevated standard deviations of weathered zone thickness, marking a gradual transition to the steady landsliding regime once V^* exceeds ~ 70 (Figure 9e).

The topography manifests these different regimes through the dependence of topographic gradient on drainage area (Figure 9b). In the no landsliding regime, the landscape consists of stable ridges and valleys and is dissected by the channel network down to the model's grid resolution in this example (Figure 9c). Because of this, slopes are steepest at the smallest drainage areas and then decrease as a power law function of drainage area for areas greater than $\sim 4 \times 10^3 \text{ m}^2$, consistent with the stream power model (equation (2)). In the stochastic landsliding regime, the topographic gradient slightly decreases up to a drainage area of $\sim 10^4 \text{ m}^2$. At the smallest drainage areas, the slope is less than that of the no landsliding regime, while at drainage areas from $\sim 4 \times 10^3$ to $1 \times 10^4 \text{ m}^2$, the slope is greater. This documents how stochastic landsliding in the model removes weathered material from the parts of the catchment with the lowest drainage areas and the steepest slopes and then deposits this material in the valley network, locally steepening low order channels (Figure 9d). In the steady landsliding regime, the topographic gradient at the smallest drainage areas is lower than in either of the other regimes, increases gradually up to a drainage area of $\sim 4 \times 10^3 \text{ m}^2$, then remains fairly

constant from drainage areas of $\sim 4 \times 10^3$ to $5 \times 10^4 \text{ m}^2$. This reflects the large landslide flux, relative to soil creep and stream power, which predicts that for a constant depth, the magnitude of the topographic gradient should slightly increase non-linearly with distance from a divide (equation (11)). For areas greater than $\sim 5 \times 10^4 \text{ m}^2$, slope again decreases rapidly in agreement with the stream power model. In both landsliding regimes, the topographic gradient in channels with drainage areas of $\sim 10^4 \text{ m}^2$ up to at least 10^6 m^2 is greater on average than in the no landsliding regime because the landslide term contributes to net deposition in these concave areas of the landscape, forcing them to be steeper in order for stream power incision to keep up with the uplift rate.

The slope-area plots from the stochastic and steady landsliding regimes exhibit trends similar to those of our study areas (Figure 4). The model's coarser spatial resolution does not resolve the initial peak in topographic gradient evident in the 1 m resolution LiDAR-derived slope-area plots, but does capture the transition from the landslide dominated lower drainage areas to the stream power dominated higher drainage areas. Landslides in both the stochastic and steady landsliding regimes tend to reduce topographic gradients near drainage divides, where they erode material, and steepen topographic gradients in the low order channel network, where they deposit material. This pushes the transition to the stream power dominated part of the landscape to higher drainage areas, and landslides with a higher V^* are more effective at moving this transition point.

4.6. Uplift rate and catchment relief

To put our landscape evolution model in a broader spatial and temporal context, we determined how topographic relief varies with uplift rate in each of the three

landscape types produced by the model. To construct each relief-uplift rate curve we let $D = 0.01 \text{ m}^2 \text{ yr}^{-1}$, $K = 0.01 \text{ yr}^{-1}$, $L = 4 \text{ m}$, $a = 1 \times 10^{-60} \text{ m}^3 \text{ kg}^{-3} \text{ yr}^5$, and $U = 0.05$ to 5 mm yr^{-1} and recorded the maximum elevation of each steady state modeled catchment. For the steady landsliding regime, we let $P_0 \approx 7U$ in order to have a thick steady state weathered zone of $\zeta = 8 \text{ m}$, for the stochastic landsliding regime, we let $P_0 \approx 2U$ to give $\zeta = 3 \text{ m}$, and for the no landsliding regime we let $a = 0$.

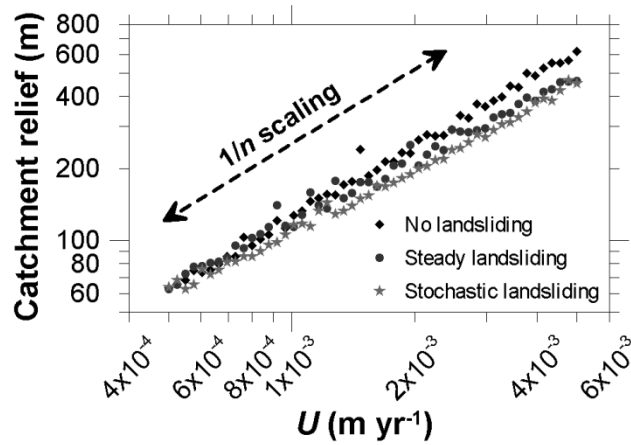


Figure 10. Relief v. uplift rate curves for modeled landscapes in each of the three landsliding regimes. In the no landsliding regime relief scales as $U^{0.99 \pm 0.03}$ which is consistent with the stream power model with $n = 1$, in the steady landsliding regime relief scales as $U^{0.91 \pm 0.02}$, and in the stochastic landsliding regime relief scales as $U^{0.85 \pm 0.03}$. Landsliding therefore weakly but significantly weakens the dependence of total catchment relief on uplift rate.

In the no landsliding regime and for this combination of parameters, relief increases with uplift rate as $U^{0.99 \pm 0.03}$, which is consistent with the stream power model when $n = 1$ [Whipple and Tucker, 1999] and predicted by equation (14) with $D^* = 0$ and $V^* = 0$. The extent and steepness of the fluvial network therefore generates the majority of the total catchment relief with hillslopes above first order valleys contributing only a small fraction of total relief. Catchments in the steady landsliding regime generally have

less total relief for a given uplift rate, and relief scales as $U^{0.91\pm 0.02}$, while catchments in the stochastic landsliding regime have even less relief for a given U , and relief scales as $U^{0.85\pm 0.03}$. Both these relief-uplift scaling exponents are significantly lower than that of the no landsliding regime, indicating that the presence of landsliding, especially stochastic landsliding, in the model slightly weakens the dependence of catchment relief on uplift rate. If landsliding were the only important process in the model ($D^* = 0$ and $K^* = 0$ in equation (14)), catchment relief would be the same as the local hillslope relief and would scale as $U^{1/p}$ [Booth and Roering, 2011]. However, the fact that the scaling exponents in both landsliding regimes are still fairly close to 1 indicates that the fluvial network still plays an important role in setting overall catchment relief, so long as the stream power term is large enough to dissect the model catchment into ridges and valleys.

5. Discussion and Conclusions

Our landscape evolution model captured the most salient characteristics of our study areas, and should be adaptable to a wide variety of other landscapes. To apply the model to a given study area, one needs to independently estimate as many of the parameters in equations (11) and (13) as possible, some of which are more challenging to infer than others. For the landslide term, borehole deformation data, as we exploited here, is one way to estimate the key landslide parameters a and p . Since the model is meant to simulate long term (longer than $\sim 10^3$ yr) landscape evolution, such measurements should record deformation over at least a season of movement in order for a and p to be representative of their average, long term values. Also, for the shallow flow approximation to be most valid, deformation data should come from parts of a landslide

with a constant topographic gradient and thickness, where longitudinal stresses are minimal. A combination of remote sensing and geophysical data could also potentially constrain the flow law parameters. For example, high resolution topographic data (LiDAR) and repeat aerial photographs or satellite interferometry could provide spatially extensive information about topographic gradient and surface deformation [Hilley *et al.*, 2004; Strozzi *et al.*, 2005; Schwab *et al.*, 2008; Roering *et al.*, 2009; Mackey and Roering, 2011; DeLong *et al.*, 2012], while shallow geophysics such as shallow seismic, ground penetrating radar, or electrical resistivity could provide spatially extensive depth information [Jongmans and Garambois, 2007; Travelletti and Malet, 2012].

The model also provides a framework to predict how deep-seated landslide prone landscapes might respond to changes in climatic forcing. Many slow-moving landslides move seasonally once the groundwater table has risen sufficiently to raise pore water pressures and decrease the effective normal stresses [Iverson and Major, 1987]. After the onset of motion during the wet season, velocity often correlates with precipitation [Keefner and Johnson, 1983], but these wet season velocities are typically large and relatively constant compared to the much slower dry season velocities [Iverson and Major, 1987; Zhang *et al.*, 1993; Coe *et al.*, 2003; Schulz *et al.*, 2009b]. This suggests that slow-moving landslides respond to longer wet seasons by moving for a longer period of time, rather than by moving much faster than in shorter wet seasons. The parameter a , which is based empirically on a landslide's deformation over a given time scale, is sensitive to this behavior if the time scale is longer than seasonal, with a proportionately larger value of a resulting from a longer period of landslide movement in a given season. However, changes in the amount and duration of precipitation might also affect other model

parameters, especially the weathered zone depth. In clay-rich lithologies such as those in our study areas, cyclic wetting and drying often drives weathering so that the weathering front tends to track the position of the lowest groundwater table [Ollier, 1969; Franklin and Chandra, 1972; Matsukura and Mizuno, 1986; Stephenson and Kirk, 2000; Rempe et al., 2010]. Since this sets landslide depth in our model, deeper weathering, perhaps due to a temporary period of decreased precipitation, would increase landslide flux once precipitation increased again. In the context of our Waipaoa study area, the rapid incision beginning ~ 18 k. a. [Berryman et al., 2000], lowered river channel elevations and groundwater levels, resulting in deeper weathering and perhaps a dramatic increase in deep-seated landsliding [Gage and Black, 1979].

If a landscape is near a border between the regimes of Figure 8, such climatic changes might cause dramatic shifts in landslide behavior. We first consider a change in the duration of the wet season, which affects the parameter a as described above. For a landscape in the no landsliding regime, an increase in a would shift the landscape to the right on Figure 8, possibly causing an abrupt transition to stochastic landsliding if the weathering depth is relatively shallow, or a gradual transition to steady landsliding if the weathering depth is relatively deep. For a landscape already in the stochastic landsliding regime, an increase in a could push the landscape into the steady landsliding regime. A change in the position of the water table, due to a change in the magnitude of precipitation seasonality, would affect landslide thickness as described in the preceding paragraph. An increase in thickness would shift a landscape up and strongly to the right on Figure 8, more dramatically than an increase in a since V^* increases non-linearly as ξ^{p+2} . This implies that a slight increase in weathered zone thickness could push a

landscape from the no landsliding to the stochastic landsliding regime for thin weathered zones, from the no landsliding to the steady landsliding regime for thick weathered zones, or from the stochastic landsliding to steady landsliding regime for thin weathered zones. Although we only investigated $p = 3$ in this study, higher values of p relevant to landslides with very thin shear zones would increase the sensitivity of V^* to ζ , causing such transitions to be even more abrupt.

In conclusion, we proposed a general, mechanistic geomorphic transport law for slow-moving, deep-seated landslides and implemented this law in a landscape evolution model to determine the geomorphic conditions at which landsliding is important in shaping topography. For a relatively thick weathered zone, which sets landslide depth, a non-dimensional number defined as the ratio of the uplift timescale to the landslide timescale predicted a gradual transition from stream power- and soil creep-dominated landscapes to landslide-dominated landscapes with increases in the landslide flow law parameter or the weathered zone depth. These landslide-dominated landscapes experienced a large, spatially variable, but temporally steady landslide flux that systematically reduced catchment relief, measured as the mean topographic gradient, and increased valley spacing. For relatively thin weathered zone depths, landscapes transitioned abruptly from stream power- and soil creep-dominated to landslide-dominated at a lower value of the non-dimensional landslide number than predicted for thicker weathered zones. Landslides in this regime were stochastic such that the flux varied dramatically in both time and space, causing highly variable weathered zone depths in addition to a reduced mean topographic gradient and increased valley spacing. For very large values of the non-dimensional landslide number, these landscapes

underwent an additional transition from stochastic landsliding to steady landsliding as for the thick weathered zones. Both the stochastic and steady landsliding regimes produced slope-area plots similar to those generated by our study areas. Landsliding reduced topographic gradients at low drainage areas where landslides initiated in the model, increased topographic gradients in the low order channel network where landslides deposited material, and thereby pushed the transition to the stream power-dominated parts of the landscape to higher drainage areas. We suggest that this is the first landscape evolution model to accurately capture the most salient features of slow-moving, deep-seated landslides in the context of landscape evolution, and that our proposed geomorphic transport law for these landslides is adaptable to a wide range of geologic settings.

APPENDIX

NUMERICAL SOLUTION OF EQUATIONS (12) AND (13)

We solved the coupled equations (12) and (13) by tracking the time evolution of the bedrock elevation, b , and the land surface elevation, z , on a finite difference grid. For each time step of duration Δt we first determined b using the explicit scheme

$$b_{i,j}^{k+1} = b_{i,j}^k + \Delta t \left[U - P_0 \exp\left(\frac{-(z_{i,j}^k - b_{i,j}^k)}{H_0}\right) \right], \quad (\text{A1})$$

where the subscripted i and j refer to indices of locations within the model domain, and the superscripted k indexes the time step. We then determined z using the explicit scheme

$$z_{i,j}^{k+1} = z_{i,j}^k + \Delta t \left(\frac{\partial z}{\partial t} \right)^k. \quad (\text{A2})$$

To approximate $\partial z / \partial t$ at time step k , we used finite difference approximations of the derivatives in each of the terms on the right-hand side of equation (13). For the stream power term we used an upwind scheme, which defines the topographic gradient as the forward difference in the direction of steepest descent [Pelletier, 2008, p. 93], such that

$$|\nabla z|_{i,j} = \left| \frac{\Delta z}{\delta x} \right|_{D8}, \quad (\text{A3})$$

where Δz is the change in elevation over a horizontal distance of δx , and the subscripted $D8$ indicates the direction of steepest descent between a node and its eight nearest neighbors [O'Callaghan and Mark, 1984]. If the steepest descent is in the x - or y -direction, $\delta x = \Delta x$ and $\Delta z = z_{i\pm 1,j} - z_{i,j}$ or $z_{i,j\pm 1} - z_{i,j}$, while on the diagonal, $\delta x = \sqrt{2}\Delta x$ and $\Delta z = z_{i\pm 1,j\pm 1} - z_{i,j}$, assuming a grid spacing of Δx in both the x - and y -directions. We also calculated the drainage area using the $D8$ algorithm. To eliminate grid size effects on the incision rate given by the stream power model, we distributed the incision in each node

over a channel width, w [Howard, 1994; Perron et al., 2008a], determined by the empirical relationship

$$w_{i,j} = 0.005\sqrt{A_{i,j}}. \quad (\text{A4})$$

The upwind scheme introduces numerical diffusion [Smolarkiewicz, 1983] with an effective diffusivity, D_{num} , that varies spatially in the case of the stream power model and depends on the size of the time step:

$$D_{num_{i,j}} = \frac{Kw_{i,j}A_{i,j}^m|\nabla z|_{i,j}^{n-1}}{2} \left(1 - \frac{\Delta t K w_{i,j} A_{i,j}^m |\nabla z|_{i,j}^{n-1}}{\Delta x^2}\right). \quad (\text{A5})$$

We eliminated this effect by applying the Smolarkiewicz [1983] correction

$$\widetilde{\Delta z}_{i,j} = -\Delta t \left| \frac{\Delta(D_{num}|\nabla z|)}{\delta x} \right|_{DB}, \quad (\text{A6})$$

where $\widetilde{\Delta z}_{i,j}$ indicates a small correction to be made to $z_{i,j}^{k+1}$ each time step. For the soil creep term we discretized the Laplacian operator using a 5-point stencil:

$$\nabla^2 z = \frac{z_{i+1,j} + z_{i-1,j} + z_{i,j+1} + z_{i,j-1} - 4z_{i,j}}{\Delta x^2}. \quad (\text{A7})$$

The landslide term has the form of a nonlinear diffusion equation, which generally requires the use of staggered grids for conditional stability in a finite difference model.

We implemented this technique following Oerlemans and van der Veen [1984] by first calculating the effective nonlinear diffusivity as

$$D_{eff_{i,j}} = \frac{\alpha(\rho_{ts}g)^p \left(\left(\frac{z_{i+1,j} - z_{i-1,j}}{2\Delta x} \right)^2 + \left(\frac{z_{i,j+1} - z_{i,j-1}}{2\Delta x} \right)^2 \right)^{\frac{p-1}{2}} H_{i,j}^{p+2}}{p+2}, \quad (\text{A8})$$

at each node in the regular finite difference grid. We then calculated the flux on a staggered grid consisting of points halfway between each of the nodes in the regular finite difference grid in the x - and y -directions. For example, the flux at the point on the staggered grid halfway between the node at (i,j) and $(i+1,j)$ is

$$q_{ts_{i+1/2,j}} = \frac{D_{eff_{i+1,j}} + D_{eff_{i,j}}}{2} \frac{z_{i+1,j} - z_{i,j}}{\Delta x}, \quad (\text{A9})$$

which is in the x -direction. Using equivalent expressions for the flux at the three remaining neighboring nodes in the staggered grid, the divergence of the landslide flux at node (i,j) is

$$(\nabla \cdot q_{ls})_{i,j} = \frac{q_{ls_{i+1/2,j}} - q_{ls_{i-1/2,j}} + q_{ls_{i,j+1/2}} - q_{ls_{i,j-1/2}}}{\Delta x}. \quad (\text{A10})$$

The above finite difference scheme implies different maximum stable time steps for the stream power, soil creep, and landslide terms, given by

$$\Delta t \leq \frac{\Delta x}{(KwA^m |\nabla z|^{n-1})_{max}}, \quad (\text{A11})$$

$$\Delta t \leq \frac{\Delta x^2}{2D}, \quad (\text{A12})$$

$$\text{and } \Delta t \leq \frac{\Delta x^2}{4(D_{eff})_{max}}, \quad (\text{A13})$$

respectively, where the subscripted *max* indicates the maximum value of the quantity in parentheses within the model domain. We used an adaptable time step equal to the minimum of equations (A11-13), which for most simulated landscapes was set either by the stream power term at the node with the greatest drainage area or by the landslide term where the quantity $|\nabla z|^{p-1} H^{p+2}$ was greatest.

REFERENCES CITED

Chapter II

- Addison, P.S., 2002. *The Illustrated Wavelet Handbook: Introductory Theory and Applications in Science, Engineering, Medicine and Finance*. Institute of Physics Publishing, Bristol, UK.
- Armstrong, J.E., Crandell, D.R., Easterbrook, D.J., Noble, J.B., 1965. Late Pleistocene stratigraphy and chronology in southwestern British Columbia and northwestern Washington. *GSA Bulletin* 76, 321–330.
- Beeson, M.H., Tolan, T.L., Madin, I.P., 1989. *Geologic Map of the Lake Oswego Quadrangle, Clackamas, Multnomah and Washington Counties, Oregon*. Geologic Map Series 59, Oregon Department of Geology and Mineral Industries, Portland, OR.
- Beeson, M.H., Tolan, T.L., Madin, I.P., 1991. *Geologic Map of the Portland Quadrangle, Multnomah and Washington Counties, Oregon*. Geologic Map Series 75, Oregon Department of Geology and Mineral Industries, Portland, OR.
- Booth, D.B., 1987. Timing and processes of deglaciation along the southern margin of the Cordilleran ice sheet. In: Ruddiman, W.F., Wright Jr., H.E. (Eds.), *North America and Adjacent Oceans During the Last Deglaciation; The Geology of North America*, K-3. Geological Society of America, Boulder, CO, pp. 71–90.
- Carrara, A., Cardinali, M., Guzzetti, F., 1992. Uncertainty in assessing landslide hazard and risk. *ITC Journal* 2, 172–183.
- Chadwick, J., Glenn, N., Thackray, G., Dorsch, S., 2005. Landslide surveillance: new tools for an old problem. *Eos* 86 (11), 109–114.
- Cruden, D.M., Varnes, D.J., 1996. Landslide types and processes. In: Turner, A.K., Schuster, R.L. (Eds.), *Landslides Investigation and Mitigation*. National Academy Press, Washington, DC, pp. 36–75.
- Galli, M., Ardizzone, F., Cardinali, M., Guzzetti, F., Reichenbach, P., 2008. Comparing landslide inventory maps. *Geomorphology* 94, 268–89.
doi:10.1016/j.geomorph.2006.09.023.
- Galster, R.W., Laprade, W.T., 1991. Geology of Seattle, Washington, United States of America. *Bulletin of the Association of Engineering Geologists* 28 (3), 235–302.

- Glenn, N.F., Streutker, D.R., Chadwick, D.J., Thackray, G.D., Dorsch, S.J., 2006. Analysis of LiDAR-derived topographic information for characterizing and differentiating landslide morphology and activity. *Geomorphology* 73, 131–148.
- Guzzetti, F., Carrara, A., Cardinali, M., Reichenbach, P., 1999. Landslide hazard evaluation: a review of current techniques and their application in a multi-scale study, Central Italy. *Geomorphology* 31, 181–216.
- Guzzetti, F., Cardinali, M., Reichenbach, P., Carrara, A., 2000. Comparing landslide maps: a case study in the upper Tiber River basin, central Italy. *Environmental Management* 25 (3), 247–263. doi:10.1007/s002679910020.
- Hanley, J.T., 1977. Fourier analysis of the Catawba Mountain knolls, Roanoke County, Virginia. *Mathematical Geology* 9 (2), 159–163.
- Harrison, J.M., Lo, C.P., 1996. PC-based two-dimensional discrete Fourier transform programs for terrain analysis. *Computers and Geosciences* 22 (4), 419–424.
- Haugerud, R.A., Harding, D.J., Johnson, S.Y., Harless, J.L., Weaver, C.S., Sherrod, B.L., 2003. High resolution Lidar topography of the Puget Lowland, Washington—a bonanza for earth science. *GSA Today* 13 (6), 9.
- Hovius, N., Stark, C.P., Allen, P.A., 1997. Sediment flux from a mountain belt derived by landslide mapping. *Geology* 25 (3), 231–234.
- Hovius, N., Stark, C.P., Hao-Tsu, C., Jiun-Chuan, L., 2000. Supply and removal of sediment in a landslide-dominated mountain belt: Central Range, Taiwan. *Journal of Geology* 108, 73–89.
- Jordan, G., Schott, B., 2005. Application of wavelet analysis to the study of spatial pattern of morphotectonic lineaments in digital terrain models. A case study. *Remote Sensing of the Environment* 94, 31–38.
- Kumar, P., Foufoula-Georgiou, E., 1994. Wavelet analysis in geophysics: an introduction. In: Foufoula-Georgiou, E., Kumar, P. (Eds.), *Wavelets in Geophysics*. Academic Press, San Diego, CA, pp. 1–44.
- Kumar, P., Foufoula-Georgiou, E., 1997. Wavelet analysis for geophysical applications. *Reviews of Geophysics* 35 (4), 385–412.
- Lashermes, B., Foufoula-Georgiou, E., Dietrich, W.E., 2007. Channel network extraction from high resolution topography using wavelets. *Geophysical Research Letters* 34, L23S04. doi:10.1029/2007GL031140.

- Madin, I.P., Niewendorp, C.A., 2008. Preliminary Geologic Map of the Dixie Mountain Quadrangle, Washington, Multnomah and Columbia Counties, Oregon. Open-File Report O-08-07, Oregon Department of Geology and Mineral Industries, Portland, OR.
- Malamud, B.D., Turcotte, D.L., 2001. Wavelet analyses of Mars polar topography. *Journal of Geophysical Research* 106 (8), 17497–17504.
- Malamud, B.D., Turcotte, D.L., Guzzetti, F., Reichenbach, P., 2004a. Landslide inventories and their statistical properties. *Earth Surface Processes and Landforms* 29, 687–711. doi:10.1002/esp.1064.
- Malamud, B.D., Turcotte, D.L., Guzzetti, F., Reichenbach, P., 2004b. Landslides, earthquakes, and erosion. *Earth and Planetary Science Letters* 229, 45–59.
- McKean, J., Roering, J., 2004. Objective landslide detection and surface morphology mapping using high-resolution airborne laser altimetry. *Geomorphology* 57, 331–351.
- McKean, J.A., Isaak, D.J., Wright, C.W., 2008. Geomorphic controls on salmon nesting patterns described by a new, narrow-beam terrestrial-aquatic lidar. *Frontiers in Ecology and the Environment* 6. doi:10.1890/070109.
- Nilsen, T.H., Brabb, E.E., 1977. Slope stability studies in the San Francisco Bay region, California. *Geological Society of America, Reviews in Engineering Geology* 3, 235–243.
- Nilsen, T.H., Wright, F.H., Vlastic, C., Spangle, W.E., 1979. Relative slope stability and land-use planning in the San Francisco Bay region, California. U.S. Geological Survey Professional Paper 944. 104 pp.
- Percival, D.P., 1995. On estimation of the wavelet variance. *Biometrika* 82, 619–631.
- Perron, J.T., Kirchner, J.W., Dietrich, W.E., 2008. Spectral signatures of characteristic spatial scales and nonfractal structure in landscapes. *Journal of Geophysical Research* 113, F04003. doi:10.1029/2007JF000866.
- Priestley, M.B., 1981. *Spectral Analysis and Time Series*. Academic Press, New York.
- Rayner, J.N., 1972. The application of harmonic and spectral analysis to the study of terrain. In: Chorley, R.J. (Ed.), *Spatial Analysis in Geomorphology*. Methuen, London, pp. 283–302.

- Roering, J.J., Kirchner, J.W., Dietrich, W.E., 2005. Characterizing structural and lithologic controls on deep-seated landsliding: implications for topographic relief and landscape evolution in the Oregon Coast Range, USA. *GSA Bulletin* 117, 654–668. doi:10.1130/B25567.1.
- Schulz, W.H., 2004. Landslides Mapped Using LIDAR Imagery, Seattle, Washington. Open-File Report 2004-1396, U.S. Geological Survey, Reston, VA, 11 pp, 1 plate.
- Schulz, W.H., 2005. Landslide Susceptibility Estimated from Mapping Using Light Detection and Ranging (LIDAR) Imagery and Historical Landslide Records, Seattle, Washington. Open-File Report 2005-1405, U.S. Geological Survey, Reston, VA, 16 pp, 1 plate.
- Schulz, W.H., 2007. Landslide susceptibility revealed by LIDAR imagery and historical records, Seattle, Washington. *Engineering Geology* 89, 67–87.
- Slatton, K.C., Carter, W.E., Shrestha, R.L., Dietrich, W., 2007. Airborne laser swath mapping: achieving the resolution and accuracy required for geosurficial research. *Geophysical Research Letters* 34, L23S10. doi:10.1029/2007GL031939.
- Torrence, C., Compo, G.P., 1998. A practical guide to wavelet analysis. *Bulletin of the American Meteorological Society* 79 (1), 61–78.
- Trimble, D.E., 1963. Geology of Portland, Oregon and adjacent areas. *Bulletin* 1119, U.S. Geological Survey, Washington, DC, 119 pp.
- Tubbs, D.W., 1974. Landslides in Seattle. Washington Division of Geology and Earth Resources Information Circular 52, 15 pp., 1 plate.
- Tubbs, D.W., 1975. Causes, mechanisms and prediction of landsliding in Seattle. Seattle, University of Washington, Ph.D. dissertation, 89 pp., 1 plate.
- Van Den Eeckhaut, M., Poesen, J., Verstraeten, G., Vanacker, V., Moeyersons, J., Nyssen, J., van Beek, L.P.H., 2005. The effectiveness of hillshade maps and expert knowledge in mapping old deep-seated landslides. *Geomorphology* 67, 351–363.
- Van Den Eeckhaut, M., Poesen, J., Verstraeten, G., Vanacker, V., Nyssen, J., Moeyersons, J., van Beek, L.P.H., Vandekerckhove, L., 2007a. Use of LIDAR-derived images for mapping old landslides under forest. *Earth Surface Processes and Landforms* 32, 754–769.
- Van Den Eeckhaut, M., Verstraeten, G., Poesen, J., 2007b. Morphology and internal structure of a dormant landslide in a hilly area: the Collinabos landslide (Belgium). *Geomorphology* 89, 258–273.

Wieczorek, G.F., 1984. Preparing a detailed landslide-inventory map for hazard evaluation and reduction. *Bulletin of the Association of Engineering Geologists* 21 (3), 337–342.

Wills, C.J., McCrink, T.P., 2002. Comparing landslide inventories, the map depends on the method. *Environmental and Engineering Geoscience* 8, 279–293.

Chapter III

Ahnert, F. (1976), Brief description of a comprehensive three-dimensional process-response model of landform development, *Z. Geomorphol. Suppl.*, 25, 29-49.

Ahnert, F. (1977), Some comments on the quantitative formulation of geomorphological processes in a theoretical model, *Earth Surf. Processes*, 2, 191-202.

Ahnert, F. (1987), Process-response models of denudation at different spatial scales, *Catena*, 10, Suppl, 31-50.

Barnes, H.A., J.F. Hutton, and K. Walters (1989), *An Introduction to Rheology*, Elsevier, Amsterdam.

Baum, R.L., W. Savage, and J. Wasowski (2003), Mechanics of earthflows, Proceedings of the International Conference FLOWS, Sorrento, Italy.

Bovis, M.J., and P. Jones (1992), Holocene history of earthflow mass movements in south-central British Columbia—The influence of hydroclimatic changes, *Can. J. Earth Sci.*, 29, 1746-1755.

Brunetti, M.T., F. Guzzetti, and M. Rossi (2009), Probability distributions of landslide volumes, *Nonlin. Processes Geophys.*, 16, 179-188.

Brunsdon, D. (1984), Mudslides, in *Slope Instability*, edited by D. Brunsdon and D.B. Prior, pp. 363-418, John Wiley & Sons Ltd., Chichester, UK.

Burbank, D.W., J. Leland, E. Fielding, R.S. Anderson, N. Brozovic, M.R. Reid, and C. Duncan (1996), Bedrock incision, rock uplift and threshold hillslopes in the northwestern Himalayas, *Nature*, 379, 505–510.

Carson, M.A., and D.J. Petley (1970), The existence of threshold hillslopes in the denudation of landscapes, *T. I. Brit. Geogr.*, 49, 71-95.

Christensen, M.N. (1965), Late Cenozoic deformation in the Central Coast Ranges of California, *Geol. Soc. Am. Bull.*, 76, 1105-1124.

- Coe, J.A., W.L. Ellis, J.W. Godt, W.Z. Savage, J.E. Savage, J.A. Michael, J.D. Kibler, P.S. Powers, D.J. Lidke, and S. Debray (2003), Seasonal movement of the Slumgullion landslide determined from Global Positioning System surveys and field instrumentation, July 1998-March 2002, *Eng. Geol.*, 68, 67-101.
- Crozier, M.J. (1968), Earthflows and related environmental factors of Eastern Otago, *J. Hydrol. N. Z.*, 7, 4-12.
- Cruden, D.M., and J. Krahn (1973), A reexamination of the geology of the Frank Slide, *Can. Geotech. J.*, 10, 581-591, doi:10.1139/t73-054.
- Cruden, D.M., and D.J. Varnes (1996), Landslide types and processes, in *Landslides Investigation and Mitigation*, edited by A.K. Turner and R.L. Schuster, pp. 36-75, National Academy Press, Washington, D.C.
- Culling, W.E.H. (1960), Analytical theory of erosion, *Geology*, 68, 336-344.
- Davis, W.M. (1892), The convex profile of bad-land divides, *Science*, 20, 245.
- Dietrich, W.E., and T. Dunne (1993), The channel head, in *Channel Network Hydrology*, edited by K. Beven and M.J. Kirkby, pp. 175-219, John Wiley & Sons Ltd., New York.
- Dietrich, W.E., and J.T. Perron (2006), The search for a topographic signature of life, *Nature*, 439, 411-418.
- Dietrich, W.E., D.G. Bellugi, L.S. Sklar, J.D. Stock, A.M. Heimsath, and J.J. Roering (2003), Geomorphic transport laws for predicting landscape form and dynamics, in *Prediction in Geomorphology, Geophys. Monogr. Ser.*, vol. 135, edited by P.R. Wilcock and R.M. Iverson, pp. 103-132, AGU, Washington, D.C.
- Densmore, A.L., M.A. Ellis, and R.S. Anderson (1998), Landsliding and the evolution of normal-fault-bounded mountains, *J. Geophys. Res.*, 103, B7, 15203-15219.
- Dumitru, T.A. (1991), Major Quaternary uplift along the northernmost San Andreas fault, King Range, northwestern California, *Geology*, 19, 526-529, doi:10.1130/009-7613(1991)019<0526:MQUATN>2.3.CO;2.
- Fernandes, N.F., and W.E. Dietrich (1997), Hillslope evolution by diffusive processes: The timescale for equilibrium adjustments, *Water Resour. Res.*, 33, 1307-1318.
- Foufoula-Georgiou, E., V. Ganti, and W.E. Dietrich (2010), A nonlocal theory of sediment transport on hillslopes, *J. Geophys. Res.*, 115, F00A16, doi:10.1029/2009JF001280.

- Franklin, J.A., and R. Chandra (1972), The slake-durability test, *Intl. J. Rock Mech. Min. Sci.*, 9, 325-341.
- Fuller, T.K., L.A. Perg, J.K. Willenbring, and K. Lepper (2009), Field evidence for climate-driven changes in sediment supply leading to strath terrace formation, *Geology*, 37, 467-470, doi:10.1130/G25487A.1.
- Furlong, K.P., and R. Govers (1999), Ephemeral crustal thickening at a triple junction: The Mendocino crustal conveyor, *Geology*, 27, 127-130, doi:10.1130/0091-7613(1999)027<0127:ECTAAT>2.3.CO;2.
- Furlong, K.P., and S.Y. Schwartz (2004), Influence of the Mendocino triple junction on the tectonics of coastal California, *Annu. Rev. Earth Planet. Sci.*, 32, 403-433, doi:10.1146/annurev.earth.32.101802.120252.
- Gabet, E.J., B.A. Pratt-Sitaula, and D.W. Burbank (2004), Climatic controls on hillslope angle and relief in the Himalayas, *Geology*, 32, 629-632, doi:10.1130/G20641.1.
- Gage, M., and R.D. Black (1979), Slope-stability and geological investigations at Mangatu State Forest, *N.Z. For. Serv. Tech. Pap.* 66, 37 pp., N.Z. For. Serv., Wellington.
- Galehouse, J.S. (1967), Provenance and paleocurrents of the Paso Robles Formation, California, *Geol. Soc. Am. Bull.*, 78, 951-978.
- Gilbert, G.K. (1877), *Geology of the Henry Mountains*, U.S. Geographical and Geological Survey of the Rocky Mountains Region, Washington D.C.
- Gilbert, G.K. (1909), The convexity of hilltops, *J. Geol.*, 17, 344-350. Guzzetti, F., A. Carrarra, M. Cardinali, and P. Reichenbach (2000), Landslide hazard evaluation: a review of current techniques and their application in a multi-scale study, Central Italy, *Geomorphology*, 31, 181-216.
- Guzzetti, F., F. Ardizzone, M. Cardinali, M. Rossi, and D. Valigi (2009), Landslide volumes and landslide mobilization rates in Umbria, central Italy, *Earth Planet. Sci. Lett.*, 279, 222-229, doi:10.1016/j.epsl.2009.01.005.
- Hack, J.T. (1957), Studies of longitudinal stream profiles in Virginia and Maryland, U.S. Geol. Surv. Prof. Pap., 294-B, 97 pp.
- Hergarten, S., and H.J. Neugebauer (1998), Self-organized criticality in a landslide model, *Geophys. Res. Lett.*, 25, 801-804.

- Hergarten, S., and H.J. Neugebauer (1999), Self-organized criticality in landsliding processes, in *Process Modelling and Landform Evolution, Lecture Notes in Earth Sciences*, vol. 78, edited by S. Hergarten and H.J. Neugebauer, pp. 231-249, Springer, Berlin/Heidelberg/New York.
- Hilley, G.E., Bürgmann, R., Ferretti, A., Novali, F., and Rocca, F. (2004). Dynamics of slow-moving landslides from permanent scatterer analysis, *Science*, *304*, 1952-1955.
- Hovius, N., C.P. Stark, and P.A. Allen (1997), Sediment flux from a mountain belt derived by landslide mapping, *Geology*, *25*, 231-234, doi: 10.1130/0091-7613(1997)025<0231:SFFAMB>2.3.CO;2.
- Howard, A. D. (1994), A detachment-limited model of drainage basin evolution, *Water Resour. Res.*, *30*, 2261–2285.
- Howard, A. D. (1997), Badland morphology and evolution: Interpretation using a simulation model, *Earth Surf. Processes*, *22*, 211–227.
- Howard, A.D., and G. Kerby (1983), Channel changes in badlands, *Geol. Soc. Am. Bull.*, *94*, 739-752.
- Istanbulluoglu, E., and R.L. Bras (2005), Vegetation-modulated landscape evolution: Effects of vegetation on landscape processes, drainage density, and topography, *J. Geophys. Res.*, *110*, F02012, doi: 10.1029/2004JF000249.
- Iverson, R.M. (1986a), Dynamics of slow landslides: a theory for time-dependent behavior, in *Hillslope Processes*, edited by A.D. Abrahams, pp. 297-317, Allen and Unwin, Winchester, MA.
- Iverson, R.M. (1986b), Unsteady, nonuniform landslide motion: 1. Theoretical dynamics and the steady datum state, *J. Geol.*, *94*, 1-15.
- Iverson, R.M. (1986c), Unsteady, nonuniform landslide motion: 2. Linearized theory and the kinematics of transient response, *J. Geol.*, *94*, 349-364.
- Iverson, R.M. (2005), Regulation of landslide motion by dilatancy and pore pressure feedback, *J. Geophys. Res.*, *110*, F02015, doi:10.1029/2004JF000268.
- Iverson, R.M., and J.J. Major (1987), Rainfall, groundwater flow, and seasonal movement at Minor Creek landslide, northwestern California: Physical interpretation of empirical relations, *Geol. Soc. Am. Bull.*, *99*, 579-594.

- Jayko, A.S., M.C. Blake, R.J. McLaughlin, H.N. Ohlin, S.D. Ellen, and H.M. Kelsey (1989), Reconnaissance Geologic Map of the Covelo 30- by 60-Minute Quadrangle, Northern California, U.S. Geological Survey Miscellaneous Field Investigation Map MF-2001, scale 1:100 000.
- Keefer, D.K., and A.M. Johnson (1983), Earthflows: morphology, mobilization and movement, *U.S. Geologic Survey Professional Paper 1256*, United States Government Printing Office, Washington, D.C.
- Kelsey, H.M. (1978), Earthflows in Franciscan mélangé, Van Duzen river basin, California, *Geology*, *6*, 361-364, doi:10.1130/0091-7613(1978)6<361:EIFMVD>2.0.CO;2.
- Kelsey, H.M. (1980), A sediment budget and an analysis of geomorphic process in the Van Duzen River basin, north coastal California, 1941-1975: Summary, *Geol. Soc. Am. Bull.*, *91*, 190-195.
- Kilburn, C.R.J., and D.N. Petley (2003), Forecasting giant, catastrophic slope collapse: lessons from Vajont, Northern Italy, *Geomorphology*, *54*, 21-32.
- Kirkby, M.J. (1971), Hillslope process-response models based on the continuity equation, *Inst. Brit. Geogr., Spec. Publ.* *3*, 15-30.
- Kirkby, M.J. (1987), General models of long-term slope evolution through mass movement, in *Slope Stability: Geotechnical Engineering and Geomorphology*, edited by M.G. Anderson and K.S. Richards, pp. 359-379, Wiley and Sons, Chichester, U.K.
- Kooi, H., and C. Beaumont (1996), Large-scale geomorphology; classical concepts reconciled and integrated with contemporary ideas via a surface processes model, *J. Geophys. Res.*, *101*, 3361-3386.
- Korup, O. (2008), Rock type leaves topographic signature in landslide-dominated mountain ranges, *Geophys. Res. Lett.*, *35*, L11402, doi:10.1029/2008GL034157.
- Korup, O., J.J. Clague, R.L. Hermanns, K. Hewitt, A.L. Strom, and J.T. Weidinger (2007), Giant landslides, topography, and erosion, *Earth Planet. Sci. Lett.*, *261*, 578-589.
- Lock, J., H. Kelsey, K. Furlong, and A. Woolace (2006), Late Neogene and Quaternary landscape evolution of the northern California Coast Ranges: Evidence for Mendocino triple junction tectonics, *Geol. Soc. Am. Bull.*, *118*, 1232-1246, doi:10.1130/B25885.1.

- Mackey, B.H., and J.J. Roering (2011), Sediment yield, spatial characteristics, and the long-term evolution of active earthflows determined from airborne LiDAR and historical aerial photographs, Eel River, California, *Geol. Soc. Am. Bull.*, doi:10.1130/B30306.1.1.
- Mackey, B.H., J.J. Roering, and J.A. McKean (2009). Long-term kinematics and sediment flux of an active earthflow, Eel River, California, *Geology*, 37, 803-806, doi:10.1130/G30136A.1.
- Malamude, B.D., D.L. Turcotte, F. Guzzetti, and P. Reichenbach (2004), Landslide inventories and their statistical properties, *Earth Surf. Process. Landforms*, 29, 687-711. doi:10.1002/exp.1064.
- Malet, J.P., O. Maquaire, and E. Calais (2002), The use of global positioning system techniques for the continuous monitoring of landslides: Application to the Super-Sauze earthflow (Alpes-de-Haute-Provence, France), *Geomorphology*, 43, 33-54, doi:10.1016/S0169-555X(01)00098-8.
- Maquaire, O., J.P. Malet, A. Remaitre, J. Locat, S. Klotz, and J. Guillon (2003), Instability conditions of marly hillslopes: Towards landsliding or gullyng? The case of the Barcelonnette Basin, south east France, *Eng. Geol.*, 70, 33-54, doi:10.1016/S0013-7952(03)00086-3.
- Matsukura, Y., and K. Mizuno (1986), The influence of weathering on the geotechnical properties and slope angles of mudstone in the Mineoka earth-slide area, Japan, *Earth Surf. Process. Landforms*, 11, 263-273.
- McKean, J.A. (1993), Soil creep and earthflows: Geomorphic analysis using cosmogenic isotopes and remote sensing, Ph.D. thesis, Department of Earth and Planetary Science, University of California at Berkeley, Berkeley, California.
- McKean, J.A., W.E. Dietrich, R.C. Finkel, J.R. Southon, and M.W. Caffee (1993), Quantification of soil production and downslope creep rates from cosmogenic ¹⁰Be accumulations on a hillslope profile, *Geology*, 21, 343-346.
- McLaughlin, R.J., S.D. Ellen, M.C.J. Blake, A.S. Jayko, W.P. Irwin, K.R. Aalto, G.A. Carver, and S.H.J. Clark (2000), Geology of the Cape Mendocino, Eureka, Garberville, and Southwestern Part of the Hayfork 30 × 60 Minute Quadrangles and Adjacent Offshore Area, Northern California, U.S. Geological Survey Miscellaneous Field Studies Map MF-2336, 1:100 000 scale.
- McSaveny, M.J., and G.A. Griffiths (1987), Drought, rain, and movement of a recurrent earthflow complex in New Zealand, *Geology*, 15, 643-646.

- Merritts, D., and K.R. Vincent (1989), Geomorphic response of coastal streams to low, intermediate, and high rates of uplift, Mendocino triple junction region, northern California, *Geol. Soc. Am. Bull.*, *111*, 1373-1388.
- Miller, D.J. (1995), Coupling GIS with physical models to assess deep-seated landslide hazards, *Environ. Eng. Geosci.*, *1*, 263-276.
- Montgomery, D.R., and M.T. Brandon (2002), Topographic controls on erosion rates in tectonically active mountain ranges, *Earth Planet Sc. Lett.*, *201*, 481-489.
- Montgomery, D. R., and W. E. Dietrich (1992), Channel initiation and the problem of landscape scale, *Science*, *255*, 826–830.
- Oguchi, T. (1997), Drainage density and relative relief in humid steep mountains with frequent slope failure, *Earth Surf. Processes*, *22*, 107-120.
- Ollier, C. (1969), *Weathering*, Oliver & Boyd, Edinburgh.
- Perron, J.T., J.W. Kirchner, W.E. Dietrich, and R.C. Finkel (2005), Testing model predictions of the evolution of valley spacing, Abstract H33F-02 presented at the 2005 Fall Meeting, AGU, San Francisco, Calif.
- Perron, J.T., W.E. Dietrich, and J.W. Kirchner (2008), Controls on the spacing of first-order valleys, *J. Geophys. Res.*, *113*, F04016, doi:10.1029/2007JF000977.
- Perron, J.T., J.W. Kirchner, and W.E. Dietrich (2009), Formation of evenly spaced ridges and valleys, *Nature*, *460*, 502-505, doi:10.1038/nature08174.
- Pyles, M.R., K. Mills, and G. Saunders (1987), Mechanics and stability of the Lookout Creek earth flow, *Bull. Assoc. Eng. Geol.*, *XXIV*, 267-280.
- Rempe, D.M., J. Oshun, W.E. Dietrich, R. Salve, and I. Fung (2010), Controls on the weathering front depth on hillslopes underlain by mudstones and sandstones, Abstract EP34A-05 presented at the 2010 Fall Meeting, AGU, San Francisco, Calif.
- Roering, J.J., J.W. Kirchner, and W.E. Dietrich (1999), Evidence for nonlinear, diffusive sediment transport on hillslopes and implications for landscape morphology, *Water Resour. Res.*, *35*, 853-870.
- Roering, J.J., J.W. Kirchner, and W.E. Dietrich (2005), Characterizing structural and lithologic controls on deep-seated landsliding: Implications for topographic relief and landscape evolution in the Oregon Coast Range, USA, *Geol. Soc. Am. Bull.*, *117*, 654-668, doi:10.1130/B25567.1.

- Roering, J.J., J.T. Perron, and J.W. Kirchner (2007), Functional relationships between denudation and hillslope form and relief, *Earth Planet. Sci. Lett.*, 264, 245-258.
- Roering, J.J., L.L. Stimely, B.H. Mackey, and D.A. Schmidt (2009), Using DInSAR, airborne LiDAR, and archival air photos to quantify landsliding and sediment transport, *Geophys. Res. Lett.*, 36, L19402, doi:10.1029/2009GL040374.
- Schulz, W.H., J.W. Kean, and G. Wang (2009), Landslide movement in southwest Colorado triggered by atmospheric tides, *Nat. Geosci.*, 2, 863-866, doi:10.1038/NGEO659.
- Schmidt, K.M., and D.R. Montgomery (1995), Limits to relief, *Science*, 270, 617-620.
- Selby, M.J. (1993), *Hillslope Materials and Processes*, Oxford University Press, Oxford.
- Shampine, L.F., and M.W. Reichelt (1997), The MATLAB ODE suite, *SIAM J. Sci. Comput.*, 18, 1-22.
- Small, E.E., R.S. Anderson, and G.S. Hancock (1999), Estimates of the rate of regolith production using ^{10}Be and ^{26}Al from an alpine hillslope, *Geomorphology*, 27, 131-150.
- Snyder, N.P., K.X. Whipple, G.E. Tucker, and D.J. Merritts (2000), Landscape response to tectonic forcing: Digital elevation model analysis of stream profiles in the Mendocino triple junction region, northern California, *Geol. Soc. Am. Bull.*, 112, 1250-1263.
- Stark, C.P., and N. Hovius (2001), The characterization of landslide size distributions, *Geophys. Res. Lett.*, 28, 1091-1094.
- Stephenson, W.J., and R.M. Kirk (2000), Development of shore platforms on Kaikoura Peninsula, South Island, New Zealand: II: The role of subaerial weathering, *Geomorphology*, 32, 43-56, doi:10.1016/S0169-555X(99)00062-8.
- Swanson, F. J., and D. N. Swanston (1977), Complex mass-movement terrains in the western Cascade Range, Oregon, *Rev. Eng. Geol.*, 3, 113-124.
- Swanston D.N., R.R. Ziemer, and R.J. Janda (1995), Rate and mechanisms of progressive hillslope failure in the Redwood Creek basin, northwestern California, in *Geomorphic Processes and Aquatic Habitat in the Redwood Creek Basin, Northwestern California*, edited by Nolan, K.M., Kelsey, H.M., and Marron, D.C., *U.S. Geological Survey Professional Paper 1454*, pp. E1-E16, United States Government Printing Office, Washington, D.C.
- Trotter, C.M. (1993), Weathering and regolith properties at an earthflow site, *Q. J. Eng. Geol.*, 26, 163-178.

- Tucker, G.E., and D.N. Bradley (2010), Trouble with diffusion: Reassessing hillslope erosion laws with a particle-based model, *J. Geophys. Res.*, *115*, F00A10, doi:10.1029/2009JF001264.
- Tucker, G.E., and R.L. Slingerland (1994), Erosional dynamics, flexural isostasy, and long-lived escarpments: A numerical modeling study, *J. Geophys. Res.*, *99*, 12229-12243.
- Tucker, G.E., and R.L. Slingerland (1997), Drainage basin responses to climate change, *Water Resour. Res.*, *33*, 2031-2047.
- Tucker, G.E., and R.L. Bras (1998), Hillslope processes, drainage density, and landscape morphology, *Water Resour. Res.*, *34*, 2751–2764.
- Turcotte, D.L., and G. Schubert (2002), *Geodynamics*, 2nd Ed., Cambridge University Press, New York.
- van der Beek, P., J. Braun, and K. Lambec (1999), Controls on post-mid-Cretaceous landscape evolution in the southeastern highlands of Australia: Insights from numerical surface process models, *J. Geophys. Res.*, *104*, 4945-4966.
- Vulliet, L. (2000), Natural slopes in slow movement, in *Modeling in Geomechanics*, edited by M. Zaman, J.R. Booker, and G. Gioda, pp. 654-676, John Wiley & Sons, Chichester, UK.
- Vulliet, L., and K. Hutter (1988a), Continuum model for natural slopes in slow movement, *Geotechnique*, *38*, 199-217.
- Vulliet, L., and K. Hutter (1988b), Set of constitutive models for soils under slow movement, *J. Geotech. Eng.-ASCE*, *114*, 1022-1041.
- Vulliet, L., and K. Hutter (1988c), Viscous-type sliding laws for landslides, *Can. Geotech. J.*, *25*, 467-477.
- Wheatcroft, R.A., and C.K. Sommerfield (2005), River sediment flux and shelf sediment accumulation rates on the Pacific Northwest margin, *Cont. Shelf Res.*, *25*, 311-332, doi:10.1016/j.csr.2004.10.001.
- Whipple, K.X. (2001), Fluvial landscape response time: How plausible is steady-state denudation?, *Am. J. Sci.*, *301*, 313-325.
- Whipple, K.X., and G.E. Tucker (1999), Dynamics of the stream-power incision model: Implications for height limits of mountain ranges, landscape response timescales, and research needs, *J. Geophys. Res.*, *104*, 17661-17674.

- Whipple, K.X., and G.E. Tucker (2002), Implications of sediment-flux-dependent river incision models for landscape evolution, *J. Geophys. Res.*, *107*, 2039, doi:10.1029/2000JB000044.
- Willgoose, G., R.L. Bras, and I. Rodriguez-Iturbe (1991a). A coupled channel network growth and hillslope evolution model, 1. Theory, *Water Resour. Res.*, *27*, 1671-1684.
- Willgoose, G., R.L. Bras, and I. Rodriguez-Iturbe (1991b). A coupled channel network growth and hillslope evolution model, 2. Nondimensionalization and application, *Water Resour. Res.*, *27*, 1685-1696.
- Wills, C.J., and T.P. McCrirk (2002), Comparing landslide inventories, the map depends on the method, *Environ. Eng. Geosci.*, *8*, 279-293.
- Zhang, X., C.J. Phillips, and M. Marden (1991), Internal deformation of a fast-moving earthflow, Raukumara Peninsula, New Zealand, *Geomorphology*, *4*, 145-154.

Chapter IV

- Ahnert, F. (1976), Brief description of a comprehensive three-dimensional process-response model of landform development, *Z. Geomorphol. Suppl.*, *25*, 29-49.
- Ahnert, F. (1977), Some comments on the quantitative formulation of geomorphological processes in a theoretical model, *Earth Surf. Processes*, *2*, 191-202.
- Bak, P., C. Tang, and K. Wiesenfeld (1988), Self-organized criticality, *Phys. Rev. A*, *38*, 364–374.
- Barnes, H. A., J. F. Hutton, and K. Walters (1989), *An Introduction to Rheology*, Elsevier, Amsterdam.
- Baum, R. L., W. Savage, and J. Wasowski (2004), Mechanics of earth-flows, *Proceedings of the International Workshop on Occurrence and Mechanisms of Flow-Like Landslides in Natural Slopes and Earthfills*, edited by L. Picarelli, pp.185–190, Patron Ed., Bologna, Italy.
- Berryman, K., M. Marden, D. Eden, C. Mazengarb, Y. Ota, and I. Moriya (2000), Tectonic and paleoclimatic significance of Quaternary river terraces of the Waipaoa River, East Coast, North Island, New Zealand, *N. Z. J. Geol. Geophys.*, *43*, 229–245.
- Booth, A. M., and J. J. Roering (2011), A 1-D mechanistic model for the evolution of earthflow-prone hillslopes, *J. Geophys. Res.*, *116*, F04021, doi:10.1029/2011JF002024.

- Borgatti, L., A. Corsini, M. Barbieri, G. Sartini, G. Truffelli, G. Caputo, and C. Puglisi (2006), Large reactivated landslides in weak rock masses: a case study from the Northern Apennines (Italy), *Landslides*, 3, 115–124.
- Bovis, M. J. (1985), Earthflows in the Interior Plateau, southwest British Columbia, *Can. Geotech. J.*, 22, 313–334.
- Brunsdon, D. (1984), Mudslides, in *Slope Instability*, edited by D. Brunsdon and D.B. Prior, pp. 363-418, John Wiley & Sons Ltd., Chichester, UK.
- Burbank, D. W., J. Leland, E. Fielding, R. S. Anderson, N. Brozovic, M. R. Reid, and C. Duncan (1996), Bedrock incision, rock uplift and threshold hillslopes in the northwestern Himalayas, *Nature*, 379, 505–510, doi:10.1038/379505a0.
- Blodgett, T. A., and B. L. Isacks (2007), Landslide erosion rate in the Eastern Cordillera of Northern Bolivia, *Earth Interactions*, 11, 1–30.
- Coe, J. A., W. L. Ellis, J. W. Godt, W. Z. Savage, J. E. Savage, J. A. Michael, J. D. Kibler, P. S. Powers, D. J. Lidke, and S. Debray (2003), Seasonal movement of the Slumgullion landslide determined from Global Positioning System surveys and field instrumentation, July 1998–March 2002, *Eng. Geol.*, 68, 67–101, doi:10.1016/S0013-7952(02)00199-0.
- Cristescu, N. D., O. Cazacu, and C. Cristescu (2002), A model for slow motion of natural slopes, *Can. Geotech. J.*, 39, 924–937, doi:10.1139/T02-040.
- Crosby, B. T., and K. X. Whipple (2006), Knickpoint initiation and distribution within fluvial networks: 236 waterfalls in the Waipaoa River, North Island, New Zealand, *Geomorphology*, 82, 16–38, doi:10.1016/j.geomorph.2005.08.023.
- Crozier, M. J. (1968), Earthflows and related environmental factors of Eastern Otago, *N. Z. J. Hydrol.*, 7, 4–12.
- Cruden, D. M., and D. J. Varnes (1996), Landslide types and processes, in *Landslides Investigation and Mitigation*, edited by A.K. Turner and R.L. Schuster, pp. 36–75, National Academy Press, Washington, D.C.
- Culling, W. E. H. (1960), Analytical theory of erosion, *Geology*, 68, 336–344, doi:10.1086/626663.
- Dadson, S. J., and M. Church (2005), Postglacial topographic evolution of glaciated valleys: a stochastic landscape evolution model, *Earth Surf. Processes*, 30, 1387–1403, doi:10.1002/esp.1199.
- Davis, W. M. (1892), The convex profile of bad-land divides, *Science*, 20, 245.

- DeLong, S. B., C. S. Prentice, G. E. Hilley, and Y. Ebert (2012), Multitemporal ALSM change detection, sediment delivery, and process mapping at an active earthflow, *Earth Surf. Processes*, 37, 262–272, doi:10.1002/esp.2234.
- Densmore, A. L., M. A. Ellis, and R. S. Anderson (1998), Landsliding and the evolution of normal-fault-bounded mountains, *J. Geophys. Res.*, 103, B7, 15203–15219.
- Dietrich, W. E., D. G. Bellugi, L. S. Sklar, J. D. Stock, A. M. Heimsath, and J. J. Roering (2003), Geomorphic transport laws for predicting landscape form and dynamics, in *Prediction in Geomorphology*, *Geophys. Monogr. Ser.*, vol. 135, edited by P.R. Wilcock and R.M. Iverson, pp. 103–132, AGU, Washington, D. C.
- Eyles G. O. (1985), *The New Zealand Land Resource Inventory Erosion Classification*, Water and Soil Miscellaneous Publication no. 85, Ministry of Works and Development, Soil Conservation Centre, Aokautere, Ministry of Works, Palmerston North, New Zealand.
- Furlong, K. P., and R. Govers (1999), Ephemeral crustal thickening at a triple junction: The Mendocino crustal conveyor, *Geology*, 27, 127-130, doi:10.1130/0091-7613(1999)027<0127:ECTAAT>2.3.CO;2.
- Furlong, K. P., and S. Y. Schwartz (2004), Influence of the Mendocino triple junction on the tectonics of coastal California, *Annu. Rev. Earth Planet. Sci.*, 32, 403-433, doi:10.1146/annurev.earth.32.101802.120252.
- Gabet, E. J., B. A. Pratt-Sitaula, and D. W. Burbank (2004), Climatic controls on hillslope angle and relief in the Himalayas, *Geology*, 32, 629–632, doi:10.1130/G20641.1.
- Gage, M., and R. D. Black (1979), Slope-stability and geological investigations at Mangatu State Forest, *N. Z. For. Serv., Tech. Pap. 66*, 37 pp., N.Z. For. Serv., Wellington, New Zealand.
- Gilbert, G. K. (1877), *Geology of the Henry Mountains*, U.S. Geographical and Geological Survey of the Rocky Mountains Region, Washington D.C.
- Gilbert, G. K. (1909), The convexity of hilltops, *J. Geol.*, 17, 344–350.
- Glen, J. W. (1955), The creep of polycrystalline ice, *P. Roy. Soc. Lond. A Mat.*, 228, 519–38.
- Gomez, B., and D. M. Livingston (2012), The river it goes right on: Post-glacial landscape evolution in the upper Waipaoa River basin, eastern North Island, New Zealand, *Geomorphology*, 159, 73–83, doi:10.1016/j.geomorph.2012.03.006.

- Griffiths, G. A. (1982), Spatial and temporal variability in suspended sediment yields of North Island basins, New Zealand, *J. Am. Water Resour. As.*, *18*, 575–584, doi:10.1111/j.1752-1688.1982.tb00038.x.
- Heimsath, A. M., W. E. Dietrich, K. Nishiizumi, and R. C. Finkel (1997), The soil production function and landscape equilibrium, *Nature*, *388*, 358–361.
- Hergarten, S., and H. J. Neugebauer (1998), Self-organized criticality in a landslide model, *Geophys. Res. Lett.*, *25*, 801–804.
- Hergarten, S., and H. J. Neugebauer (1999), Self-organized criticality in landsliding processes, in *Process Modelling and Landform Evolution, Lecture Notes in Earth Sciences*, vol. 78, edited by S. Hergarten and H.J. Neugebauer, pp. 231–249, Springer, Berlin/Heidelberg/New York.
- Hilley, G. E., R. Bürgmann, A. Ferretti, F. Novali, and F. Rocca (2004), Dynamics of slow-moving landslides from permanent scatterer analysis, *Science*, *304*, 1952–1955.
- Hovius, N., C. P. Stark, and P. A. Allen (1997), Sediment flux from a mountain belt derived by landslide mapping, *Geology*, *25*, 231–234, doi:10.1130/009-7613(1997)025<0231:SFFAMB>2.3.CO;2.
- Howard, A. D. (1994), A detachment-limited model of drainage basin evolution, *Water Resour. Res.*, *30*, 2261–2285.
- Howard, A. D., and G. Kerby (1983), Channel changes in badlands, *Geol. Soc. Am. Bulletin*, *94*, 739–752.
- Hutter, K. (1983), *Theoretical glaciology: material science of ice and the mechanics of glaciers and ice sheets*, D. Reidel Publishing Co., Dordrecht.
- Iverson, R. M. (1986a), Dynamics of slow landslides: a theory for time-dependent behavior, in *Hillslope Processes*, edited by A. D. Abrahams, pp. 297–317, Allen and Unwin, Winchester, MA.
- Iverson, R. M. (1986b), Unsteady, nonuniform landslide motion: 1. Theoretical dynamics and the steady datum state, *J. Geol.*, *94*, 1–15.
- Iverson, R. M. (1986c), Unsteady, nonuniform landslide motion: 2. Linearized theory and the kinematics of transient response, *J. Geol.*, *94*, 349–364.
- Iverson, R. M. (2005), Regulation of landslide motion by dilatancy and pore pressure feedback, *J. Geophys. Res.*, *110*, F02015, doi:10.1029/2004JF000268.

- Iverson, R. M., and J. J. Major (1987), Rainfall, groundwater flow, and seasonal movement at Minor Creek landslide, northwestern California: Physical interpretation of empirical relations, *Geol. Soc. Am. Bull.*, *99*, 579–594.
- Jessen, M. R., T. F. Crippen, M. J. Page, W. C. Rijkse, G. R. Harmsworth, and M. McLeod (1999), Land use capability classification of the Gisborne – East Coast region, *Landcare Research Science Series 21*, Manaaki Whenua Press, Lincoln, New Zealand.
- Jongmans, D., and S. Garambois (2007), Geophysical investigation of landslides: A review, *Bulletin Société Géologique de France*, *178*, 1–24.
- Keefer, D. K., and A. M. Johnson (1983), Earthflows: morphology, mobilization and movement, *U.S. Geologic Survey Professional Paper 1256*, United States Government Printing Office, Washington, D.C.
- Kirkby, M. J. (1971), Hillslope process-response models based on the continuity equation, *Spec. Publ. Inst. Br. Geogr.*, *3*, 15–30.
- Kirkby, M. J. (1987), General models of long-term slope evolution through mass movement, in *Slope Stability: Geotechnical Engineering and Geomorphology*, edited by M. G. Anderson and K. S. Richards, pp. 359–379, Wiley and Sons, Chichester, U.K.
- Korup, O. (2008), Rock type leaves topographic signature in landslide-dominated mountain ranges, *Geophys. Res. Lett.*, *35*, L11402, doi:10.1029/2008GL034157.
- Larsen, I. J., and D. R. Montgomery (2012), Landslide erosion coupled to tectonics and river incision, *Nat. Geosci.*, doi:10.1038/ngeo1479.
- Lock, J., H. Kelsey, K. Furlong, and A. Woolace (2006), Late Neogene and Quaternary landscape evolution of the northern California Coast Ranges: Evidence for Mendocino triple junction tectonics, *Geol. Soc. Am. Bull.*, *118*, 1232–1246, doi:10.1130/B25885.1.
- Mackey, B. H., and J. J. Roering (2011), Sediment yield, spatial characteristics, and the long-term evolution of active earthflows determined from airborne LiDAR and historical aerial photographs, Eel River, California, *Geol. Soc. Am. Bull.*, doi:10.1130/B30306.1.1.
- Mackey, B. H., J. J. Roering, and J. A. McKean (2009), Long-term kinematics and sediment flux of an active earthflow, Eel River, Calif., *Geol.*, *37*, 803–806, doi:10.1130/G30136A.1.

- Malet, J. P., and O. Maquaire (2003), Black marl earthflow mobility and long-term seasonal dynamic in southeastern France, In *Proceedings of the International Conference on Fast Slope Movements Prediction and Prevention for Risk Mitigation*, edited by L. Picarelli, pp. 333–340, Associazione Geotechnica Italiana, Pàtron Editore, Bologna.
- Marden, M., C. Mazengarb, A. Palmer, K. Berryman, and D. Rowan (2008), Last glacial aggradation and postglacial sediment production from the non-glacial Waipaoa and Waimata Catchments, Hikurangi Margin, North Island, New Zealand, *Geomorphology*, 99, 404–419, doi:10.1016/j.geomorph.2007.12.003.
- Mazengarb, C., and I. G. Speeden (2000), Geology of the Raukumara area, Institute of Geological and Nuclear Sciences 1:250,000 geological map 6, 1 sheet and 60 pp., Lower Hutt, New Zealand, Institute of Geological and Nuclear Sciences.
- McKean, J. A., W. E. Dietrich, R. C. Finkel, J. R. Southon, and M. W. Caffee (1993), Quantification of soil production and downslope creep rates from cosmogenic ¹⁰Be accumulations on a hillslope profile, *Geology*, 21, 343–346.
- McLaughlin, R. J., S. D. Ellen, M. C. J. Blake, A. S. Jayko, W. P. Irwin, K. R. Aalto, G. A. Carver, and S. H. J. Clark (2000), Geology of the Cape Mendocino, Eureka, Garberville, and Southwestern Part of the Hayfork 30 × 60 Minute Quadrangles and Adjacent Offshore Area, Northern California, U.S. Geological Survey Miscellaneous Field Studies Map MF-2336, 1:100 000 scale.
- Milliman, J. D., and J. P. M. Syvitski (1992), Geomorphic/tectonic control of sediment discharge to the ocean: The importance of small mountainous rivers, *J. Geol.*, 100, 525–544.
- Montgomery, D. R., and Fofoula-Georgiou, E. (1993), Channel network source representation using digital elevation models, *Water Resour. Res.*, 29, 3925–3934.
- Montgomery, D. R., and M. T. Brandon (2002), Topographic controls on erosion rates in tectonically active mountain ranges, *Earth Planet. Sci. Lett.*, 201, 481–489, doi:10.1016/S0012-821X(02)00725-2.
- National Research Council (2010), *Landscapes on the Edge: New Horizons for Research on Earth's Surface*, The National Academies Press, Washington, DC.
- O'Callaghan, J. F., and D. M. Mark (1984), The extraction of drainage networks from digital elevation data, *Comput. Vision Graph. Image Process.*, 28, 323–344.
- Oerlemans, J. and van der Veen, C. J. (1984), *Ice Sheets and Climate*, D. Reidel Publishing Company, Dordrecht, Holland.

- Pelletier, J. D. (2008), *Quantitative Modeling of Earth Surface Processes*, Cambridge University Press, Cambridge, UK.
- Perron, J. T., W. E. Dietrich, and J. W. Kirchner (2008a), Controls on the spacing of first-order valleys, *J. Geophys. Res.*, *113*, F04016, doi:10.1029/2007JF000977.
- Perron, J. T., J. W. Kirchner, and W. E. Dietrich (2008b), Spectral signatures of characteristic spatial scales and nonfractal structure in landscapes, *J. Geophys. Res.*, *113*, F04003, doi:10.1029/2007JF000866.
- Pyles, M. R., K. Mills, and G. Saunders (1987), Mechanics and stability of the Lookout Creek earth flow, *Bull. Assoc. Eng. Geol.*, *XXIV*, 267–280.
- Rempe, D. M. J. Oshun, W. E. Dietrich, R. Salve, and I. Fung (2010), Controls on the weathering front depth on hillslopes underlain by mud-stones and sandstones, Abstract EP34A-05 presented at the 2010 Fall Meeting, AGU, San Francisco, Calif., 13–17 Dec.
- Roering, J. J., J. W. Kirchner, and W. E. Dietrich (1999), Evidence for non-linear, diffusive sediment transport on hillslopes and implications for landscape morphology, *Water Resour. Res.*, *35*, 853–870, doi:10.1029/1998WR900090.
- Roering, J. J., L. L. Stimely, B. H. Mackey, and D. A. Schmidt (2009), Using DInSAR, airborne LiDAR, and archival air photos to quantify landsliding and sediment transport, *Geophys. Res. Lett.*, *36*, L19402, doi:10.1029/2009GL040374.
- Savage, W. and J. Wasowski (2006), A plastic flow model for the Acquara-Vadoncello landslide in Senerchia, Southern Italy, *Eng. Geol.*, *83*, 4–21.
- Schmidt, K. M., and D. R. Montgomery (1995), Limits to relief, *Science*, *270*, 617–620, doi:10.1126/science.270.5236.617.
- Schulz, W. H., J. W. Kean, and G. Wang (2009a), Landslide movement in southwest Colorado triggered by atmospheric tides, *Nat. Geosci.*, *2*, 863–866, doi:10.1038/NGEO659.
- Schulz, W. H., J. P. McKenna, J. D. Kibler, and G. Biavati (2009b), Relations between hydrology and velocity of a continuously moving landslide—evidence of pore-pressure feedback regulation landslide motion?, *Landslides*, *6*, 181–190, doi:10.1007/s10346-009-0157-4.
- Schwab, M., D. Rieke-Zapp, H. Schneider, M. Liniger, and F. Schlunegger (2008), Landsliding and sediment flux in the Central Swiss Alps: A photogrammetric study of the Schimbrig landslide, Entlebuch, *Geomorphology*, *97*, 392–406.
- Selby, M. J. (1993), *Hillslope Materials and Processes*, Oxford University Press, Oxford.

- Small, E. E., R. S. Anderson, and G. S. Hancock (1999), Estimates of the rate of regolith production using ^{10}Be and ^{26}Al from an alpine hillslope, *Geomorphology*, 27, 131–150.
- Smith, T. R., and F. P. Bretherton (1972), Stability and the conservation of mass in drainage basin evolution, *Water Resour. Res.*, 8, 1506–1529, doi:10.1029/WR008i006p01506.
- Smolarkiewicz, P. K. (1983), A simple positive definite advection scheme with small implicit diffusion, *Mon. Weather Rev.*, 111, 479–486.
- Stark, C. P., and F. Guzzetti (2009), Landslide rupture and the probability distribution of mobilized debris volumes, *J. Geophys. Res.*, 114, F00A02, doi:10.1029/2008JF001008.
- Strozzi T., P. Farina, A. Corsini, C. Ambrosi, M. Thüring, J. Zilger, A. Wiesmann, U. Wegmüller, and C. Werner (2005), Survey and monitoring of landslide displacements by means of L-band satellite SAR interferometry, *Landslides*, 2, 193–201, doi:10.1007/s10346-005-0003-2.
- Swanson, F. J., and D. N. Swanston (1977), Complex mass-movement terrains in the western Cascade Range, Oregon, *Rev. Eng. Geol.*, 3, 113–124.
- Swanston D. N., R. R. Ziemer, and R. J. Janda (1995), Rate and mechanisms of progressive hillslope failure in the Redwood Creek basin, northwestern California, in *Geomorphic Processes and Aquatic Habitat in the Redwood Creek Basin, Northwestern California*, edited by Nolan, K. M., Kelsey, H. M., and Marron, D. C., *U.S. Geological Survey Professional Paper 1454*, pp. E1–E16, United States Government Printing Office, Washington, D.C.
- Tarboton, D. G., R. L. Bras, and I. Rodriguez-Iturbe (1991), On the extraction of channel networks from digital elevation data, *Hydrol. Proc.*, 5, 81–100.
- Travelletti, J. and J. -P. Malet (2012), Characterization of the 3D geometry of flow-like landslides: A methodology based on the integration of heterogeneous multi-source data, *Eng. Geol.*, 128, 30–48.
- Trotter, C. M. (1993), Weathering and regolith properties at an earthflow site, *Q. J. Eng. Geol.*, 26, 163–178, doi:10.1144/GSL.QJEGH.1993.026.003.02.
- Tucker, G. E., and R. L. Bras (1998), Hillslope processes, drainage density, and landscape morphology, *Water Resour. Res.*, 34, 2751–2764.
- Tucker, G. E., and G. R. Hancock (2010), Modelling landscape evolution, *Earth Surf. Processes*, 35, 28–50, doi:10.1002/esp.1952.

- Turcotte, D. L., and G. Schubert (2002), *Geodynamics*, 2nd Ed., Cambridge University Press, New York.
- van der Beek, P., and J. Braun (1999), Controls on post-mid-Cretaceous landscape evolution in the southeastern highlands of Australia: Insights from numerical surface process models, *J. Geophys. Res.*, *104*, 4945–4966.
- Vulliet, L. (2000), Natural slopes in slow movement, in *Modeling in Geomechanics*, edited by M. Zaman, J.R. Booker, and G. Gioda, pp. 654–676, John Wiley & Sons, Chichester, UK.
- Vulliet, L., and K. Hutter (1988a), Continuum model for natural slopes in slow movement, *Geotechnique*, *38*, 199–217.
- Vulliet, L., and K. Hutter (1988b), Set of constitutive models for soils under slow movement, *J. Geotech. Eng.-ASCE*, *114*, 1022–1041.
- Vulliet, L., and K. Hutter (1988c), Viscous-type sliding laws for landslides, *Can. Geotech. J.*, *25*, 467–477.
- Wheatcroft, R. A., and C. K. Sommerfield (2005), River sediment flux and shelf sediment accumulation rates on the Pacific Northwest margin, *Cont. Shelf Res.*, *25*, 311–332, doi:10.1016/j.csr.2004.10.001.
- Whipple, K. X., and G. E. Tucker (1999), Dynamics of the stream-power incision model: Implications for height limits of mountain ranges, landscape response timescales, and research needs, *J. Geophys. Res.*, *104*, 17661–17674.
- Willgoose, G., R. L. Bras, and I. Rodriguez-Iturbe (1991), A coupled channel network growth and hillslope evolution model, 1. Theory, *Water Resour. Res.*, *27*, 1671–1684, doi:10.1029/91WR00935.
- Zhang, X., C.J. Phillips, and M. Marden (1991), Internal deformation of a fast-moving earthflow, Raukumara Peninsula, New Zealand, *Geomorphology*, *4*, 145–154.
- Zhang, X., C. Phillips, and M. Marden (1993), A comparison of earthflow movement mechanisms on forested and grassed slopes, Raukumara Peninsula, North Island, New Zealand, *Geomorphology*, *6*, 175–187.